Fall 2003

Effect of fullerene containing lubricants on wear resistance of machine components in boundary lubrication

Andriy Titov
New Jersey Institute of Technology

ABSTRACT

EFFECT OF FULLERENE CONTAINING LUBRICANTS ON WEAR RESISTANCE OF MACHINE COMPONENTS IN BOUNDARY LUBRICATION

by
Andriy Titov

Fullerenes, a new form of carbon nanomaterials, possess unique physical and mechanical properties that make their use as additives to liquid lubricants potentially beneficial. The goal of this study was to investigate the effect of fullerene containing lubricants on wear resistance of steel-bronze couples operating under boundary lubrication conditions. A mathematical model of deformed asperity contact was built to calculate real contact area and real contact pressure. Computer controlled wear friction testing methodology and equipment were designed, developed and implemented for obtaining reliable and objective experimental data. In addition, optical and scanning electron microscopy and standard surface texture analysis were employed. Heavy duty motor oil SAE 10 was modified by admixing fullerenes C_{60}, a fullerene mixture of C_{60} and C_{70}, fullerene containing soot, and graphite powder. The experiments showed that all of the selected fullerene additives dissolved in liquid lubricants reduce wear of the tested materials. In addition, it was found that despite improvements in wear resistance, the selected modified lubricants did not significantly change friction characteristics.

Improvement of wear resistance of contact surfaces operating with fullerene modified lubricants can be explained by the presence of fullerenes in real contact while the liquid lubricant is squeezed out. Fullerenes are considered to function as minute hard particles that do not break down under applied normal force, and tend to separate direct contact of functional surfaces of selected materials.

EFFECT OF FULLERENE CONTAINING LUBRICANTS ON WEAR RESISTANCE OF MACHINE COMPONENTS IN BOUNDARY LUBRICATION

by
Andriy Titov

A Dissertation
Submitted to the Faculty of
New Jersey Institute of Technology
in Partial Fulfillment of the Requirements for the Degree of
Doctor of Philosophy in Mechanical Engineering

Department of Mechanical Engineering

January 2004

APPROVAL PAGE

EFFECT OF FULLERENE CONTAINING LUBRICANTS ON WEAR RESISTANCE OF MACHINE COMPONENTS IN BOUNDARY LUBRICATION

Andriy Titov

Dr. Roman Dubrovsky, Dissertation Advisor — Date
Associate Professor of Mechanical Engineering, NJIT

Dr. Pasquale J. Florio, Committee Member — Date
Associate Professor of Mechanical Engineering, NJIT

Dr. Avraham Harnoy, Committee Member — Date
Professor of Mechanical Engineering, NJIT

Dr. Bernard Koplik, Committee Member — Date
Professor of Mechanical Engineering, NJIT

Dr. Melvin Zwillenberg, Committee Member — Date
Technology Development and Transfer Consultant,
Public Service Electric & Gas Company, Newark, NJ

BIOGRAPHICAL SKETCH

Author: Andriy Titov

Degree: Doctor of Philosophy

Date: January 2004

Undergraduate and Graduate Education:

- Doctor of Philosophy in Mechanical Engineering,
  New Jersey Institute of Technology, Newark, NJ, 2004

- Master of Science in Applied Physics and Mathematics,
  Moscow Institute of Physics and Technology, Moscow, Russia, 2000

- Bachelor of Science in Applied Physics and Mathematics,
  Moscow Institute of Physics and Technology, Moscow, Russia, 1998

Major: Mechanical Engineering

Presentations and Publications:

Titov, A., Dubrovsky, R., and Bezmelnitsyn, V., 2003, "Use of Arc Produced Carbon Soot as Additive to Liquid Lubricants," Journal of Tribology (to be submitted).

Titov, A., and Dubrovsky, R., 2003, "Effect of Profile Structure on Stability of Friction and Wear of Contact Surfaces", Journal of Tribology (to be submitted).

Dubrovsky, R., and Titov, A., 2003, "Computer Wear and Friction Testing Methodology for Heavy Duty Boundary Lubrication", 2003 ASME International Mechanical Engineering Congress and RD&D Expo, Washington, D.C.

Dubrovsky, R., and Titov, A., 2003, "Friction and Wear in the Presence of Fullerene Contained Lubricants at Boundary Conditions", Proceedings of STLE/ASME Joint International Tribology Conference, Ponte Vedra Beach, Florida.

Dubrovsky, R., and Titov, A., 2003, "Effect of Fullerene Contained Lubricants on Wear Resistance of Machine Components", International Workshop "Fullerenes and Atomic Clusters," St. Petersburg, Russia.

Adylkhanov, K.A., Titov, A.N., and Scherbakov, V. N., 1999, "Investigation and Prediction of Cracks Growth in Nonlinear Polymer Material", Industrial Laboratory: Diagnostics of Materials, **65**, pp. 48-51.

Adylkhanov, K.A., Titov, A.N., and Scherbakov, V. N., 1998, "Investigation and Prediction of Cracks Growth in Nonlinear Polymer Material," XXXVI Research conference of Moscow Institute of Physics and Technology, Dolgoprudnyi, Russia.

Scherbakov, V.N., and Titov, A.N., 1998, "Investigation of Kinetics of Cracks by Polarization Method", Industrial Laboratory: Diagnostics of Materials, **64**, pp. 44-48.

Scherbakov, V.N., and Titov, A.N., 1997, "Investigation and Prediction of the Process of Crack Growth in Non-linear Visco-elastic Polymer Material," XXXV Research conference of Moscow Institute of Physics and Technology, Dolgoprudnyi, Russia.

This work is dedicated to my beloved family and

to the memory of my grandparents

ACKNOWLEDGEMENTS

I would like to express my deepest appreciation to my research advisor, Dr. Roman Dubrovsky, for his remarkable guidance, constant supervision and moral support throughout this research. Special thanks are due to Dr. Pasquale J. Florio, Dr. Avraham Harnoy, Dr. Bernard Koplik and Dr. Melvin Zwillenberg, dissertation committee members, for providing many valuable suggestions.

I am very grateful to Dr. Valery Bezmelnitsyn, a member of the Surface Engineering Laboratory at NJIT for his support and inspiration. Many faculty and staff members of the Mechanical Engineering Department, especially Joe Glaz, deserve recognition for their support.

Finally, I appreciate the encouragement and help from my friends, Konstantin Babets, Oleg Petrenko, Oleksandr Dybenko and Max Roman.

TABLE OF CONTENTS

TABLE OF CONTENTS
(Continued)

TABLE OF CONTENTS
(Continued)

Chapter **Page**

TABLE OF CONTENTS
(Continued)

Chapter **Page**

LIST OF TABLES

LIST OF FIGURES

LIST OF FIGURES
(Continued)

LIST OF FIGURES
(Continued)

LIST OF FIGURES
(Continued)

LIST OF SYMBOLS

a	half-contact width
A_a	nominal contact area
A_c	contour contact area
A_r	real contact area
b	bearing area curve parameter
B	beta function
d_m	distance from the rotor axis to the point of reaction
E	Young modulus
E_{eq}	equivalent modulus of elasticity
$\dot{E}$	power
f	friction coefficient
F	friction force
F_k	kinetic (or dynamic) friction force
F_s	static friction force
h	depth of penetration
h_i	relative contact approach of *i-th* asperity
h_{max}	relative contact approach of highest asperity
H_1	distance between contact bodies in unloaded case
H_2	distance between contact bodies in loaded case
J	inertia moment of the system
L	length of cylindrical contact

LIST OF SYMBOLS
(Continued)

M	moment
n	number of cycles
n_c	total number of spherical segments
n_r	number of tips lying above level x
N	applied normal force
$\bar{N}$	dimensionless load
N_r	reaction force acting on the beam
N_{ro}	reaction force acting on the beam under zero applied load
p_a	nominal contact pressure
p_c	contour contact pressure
p_r	real contact pressure
p_{max}	maximum contact pressure
P	load per unit of projected area
r_r	roller radius
R	curvature radius
R_{eq}	equivalent contact radius
T	time period
U	rotational speed
W	weight loss
x	dimensionless coordinate
β	angular velocity

LIST OF SYMBOLS
(Continued)

ΔA_c	elementary contour contact area
ΔA_r	elementary real contact area
Δl	distance between center of roller and shoe's bottom
ε	relative approach of contact bodies
ε_{max}	maximum elastic deformation
Γ	gamma function
η	dynamic viscosity
η_{ij}	dimensionless area
κ_λ	numerical factor
λ	degree of approximation of bearing curve area
ν	Poisson ratio
Θ	generalized Kirchhoff elastic constant
ρ	material density
σ_T	yield tensile strength
τ	tangential stress of molecular bond

CHAPTER 1

INTRODUCTION

Wear caused by friction is one of the most important factors in the deterioration of machinery with moving components. It limits both service life and performance of the equipment. In order to decrease friction and reduce wear of rubbing parts, lubricants are used as a total or partial separator of surfaces in contact.

Presently, two most common approaches in lubricant improvement are development of synthetic lubricants and improvement of mineral oils by additives. Advantages of synthetic oils are their superior properties, disadvantages – their high cost. Additives are chemical compounds added to lubricating oils to impart specific properties to the finished oils. Some additives impart new and useful properties to the lubricant, some enhance already existing properties, while some act to reduce the rate at which undesirable changes take place in the product during its service life. Today, practically all types of lubricating oil contain at least one additive, and some oils contain additives of several different types. The amount of additive used varies from a few hundredths of a percent to 30% and more. The use of additives is inexpensive, compared to development of synthetic lubricants, and efficient way of getting desired properties of lubricants. Among the most widely used additives are graphite powder, zinc dialkyl dithiophosphate and others.

For efficient development of lubricants, it is important to understand the difference between two most important regimes of lubrication – hydrodynamic and boundary lubrication. In hydrodynamic lubrication, lubricant films are normally many

times thicker than the surface roughness. The film thickness normally exceeds 10^{-6} *m*. In boundary lubrication, the solids are not separated by lubricant; thus, fluid-film effects are negligible and there is considerable asperity contact. The properties of bulk lubricant are of minor importance, and the friction coefficient does not depend on the viscosity of the fluid in such extent as in hydrodynamic regime. The frictional behavior is similar to that encountered in dry friction between two solids.

Although the most common lubrication mode is hydrodynamic lubrication, the highest wear rate happens in occasional periods of boundary lubrication – in start-stop periods of machine operations. Thus, special attention should be paid to this regime and the ways, which can prevent extensive wear. Special interest of lubrication engineers is the development of additives, which will not be squeezed out in asperity contact. In this case, fullerenes separate surfaces of contacting bodies and prevent direct contact of materials. Another valuable property of fullerenes is that they may act as anti-oxidation agents, thereby lengthening lubricant service or storage life. Fullerenes may combine with and modify peroxides (initial oxidation products) to make them harmless. High elasticity, strength of C_{60} crystals, weak intermolecular interactions, low surface energy, and quazispherical shape of molecules confirm described views.

CHAPTER 2

BACKGROUND

2.1 Friction and Wear

Friction is a very complex phenomenon, which involves many different stages and parameters; its complexity is illustrated by the diagram in Figure 2.1. It shows the main factors, which must be allowed for in analyzing the frictional interaction between solids. This analysis can be facilitated if the friction and wear process is considered in three consecutive stages: interaction of surfaces, change in surface properties during sliding and surface damage.

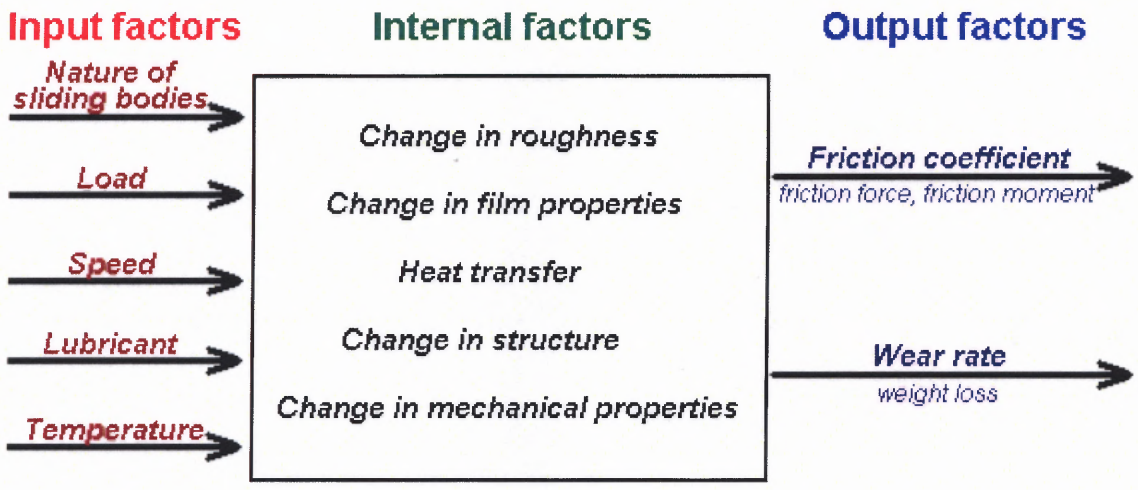

Figure 2.1 Factors that affect friction force and wear rate between solids.

Friction is not a measure of wear or the tendency to wear; therefore, it does not determine service life. Frictional heating sometimes causes a machine part to fail, but this usually occurs when circumstances create abnormal friction effects. To emphasize the

importance of friction in machine design, it is estimated that about 30 % of the power in an automobile is wasted through friction [1].

Although all described input factors are significant in friction lessening and wear rate reduction, not all of them can be easily changed. Lubricant is one of the most flexible input parameters and, therefore, attracts particular interest of tribologists and lubrication engineers. In this work, almost all parameters are considered constant, but lubricant is subject to change. To understand the effect lubricants make in friction process is important to recognize the nature of friction and types wear.

2.1.1 Friction

Friction is the resistance to motion during sliding or rolling that is experienced when one solid body moves tangentially over another with which it is in contact. The resistive tangential force, which acts in a direction directly opposite to the direction of motion, is called the friction force. Three types of friction that commonly encountered are: hydrodynamic, dry and boundary friction. Hydrodynamic friction describes the tangential component of the contact force that exists between adjacent layers in a fluid that are moving at different velocities relative to each other as in a liquid or gas between bearing surfaces. As its name suggests, dry friction describes the tangential component of the contact force that exists when two dry surfaces move relative to one another. Boundary lubrication is an intermediate case between dry and hydrodynamic modes of friction – in boundary friction, a lubricant presents in contact between surfaces, but direct contact between surfaces exists.

If the solid bodies are loaded together and a tangential force is applied, then the value of the tangential force that is required to initiate motion is the static friction force

F_s. It may take a few milliseconds before relative motion is initiated at the interface. The tangential force required to maintain relative motion is known as kinetic (or dynamic) friction force F_k. In the future, only kinetic friction force will be considered and subscript k will be omitted.

Two basic rules of intrinsic (or conventional) friction are generally obeyed over a wide range of applications [2]. The first rule is expressed by Equation (2.1)

$$F = f \cdot N \tag{2.1}$$

where F – friction force, N – applied normal force and f is friction coefficient, which is independent of normal load.

The second rule states that the friction force (or friction coefficient) is independent of apparent area of contact between the contacting bodies. Thus two bodies, regardless of their physical size, have the same coefficient of friction.

2.1.2 Wear

Wear is the surface damage or removal of material from one or both of two solid surfaces in a sliding, rolling, or impact relative to one another. In most cases, wear occurs through surface interactions at asperities. In the beginning of relative motion, material on the contacting surface may be displaced so that properties of the solid body are altered, but little or no material is actually lost. Later, material may be removed from a surface and may result in the transfer to the mating surface or may break loose as a wear particle. In the case of transfer from one material to another, net volume or mass loss of the interface is zero, although one of the surfaces is worn. Wear damage precedes actual loss of material and it may occur independently. Definition of wear is generally based on loss of material, but it should be emphasized that damage due to material displacement on a

given body, with no net change in weight or volume, also constitutes wear. Wear, like friction, is not a material property, it is a system response and, thus, subject to operating conditions.

Wear occurs by mechanical and/or chemical means and is generally accelerated by frictional heating. The intrinsic part of wear is the removal of solid material from rubbing surfaces [3-14]. Although there are fundamental works on lamination theory [15] and diffusion theory [16], five principal, quite distinct types of wear are: (1) adhesive, (2) abrasive, (3) fatigue, (4) impact by erosion and percussion and (5) chemical (or corrosive) wear. Other commonly encountered wear types - fretting and fretting corrosion – are not distinct mechanisms, but rather combinations of the adhesive, corrosive and abrasive forms of wear. According to some estimates, two-thirds of all wear encountered in industrial situations occurs because of adhesive- and abrasive-wear mechanisms. Wear by all mechanisms, except by fatigue mechanism, occurs by gradual removal of material. In many cases, wear is initiated by one mechanism and it may proceed by other wear mechanisms, thereby complicating failure analysis.

Adhesive wear. Adhesive wear occurs when two nominally flat solid bodies are in sliding contact, whether lubricated or not. Adhesion (or bonding) occurs at the asperity contact at the interface, and these contacts are sheared by sliding, which may result in detachment of a fragment from one surface and attachment to the other surface. As the sliding continues, the transferred fragments may come off the surface on which they are transferred back to the original surface or else form loose wear particles. Some are fractured by a fatigue process during repeated loading and unloading action resulting in

formation of loose particles. Schematic showing two possibilities of break (1 and 2) during shearing of an interface is shown in Figure 2.2.

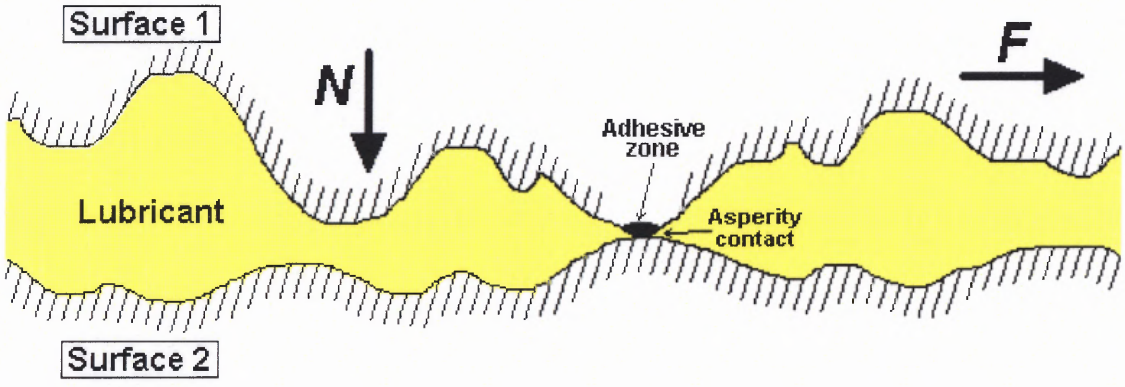

Figure 2.2 Adhesive wear, where N – normal applied load and F – friction force.

Abrasive wear. Abrasive wear occurs when asperities of a rough, hard surface or hard particles slide on a softer surface and damage the interface by plastic deformation or fracture, see Figure 2.3.

In the case of ductile materials with high fracture toughness (metals and alloys), hard asperities or hard particles result in the plastic flow of the softer material. Most metallic and ceramic surfaces during sliding show clear evidence of plastic flow, even some for ceramic brittle materials. Contacting asperities of metals deform plastically even at the lightest loads. In the case of brittle materials with low fracture toughness, wear occurs by brittle fracture. In these cases, the worn zone consists of significant cracking.

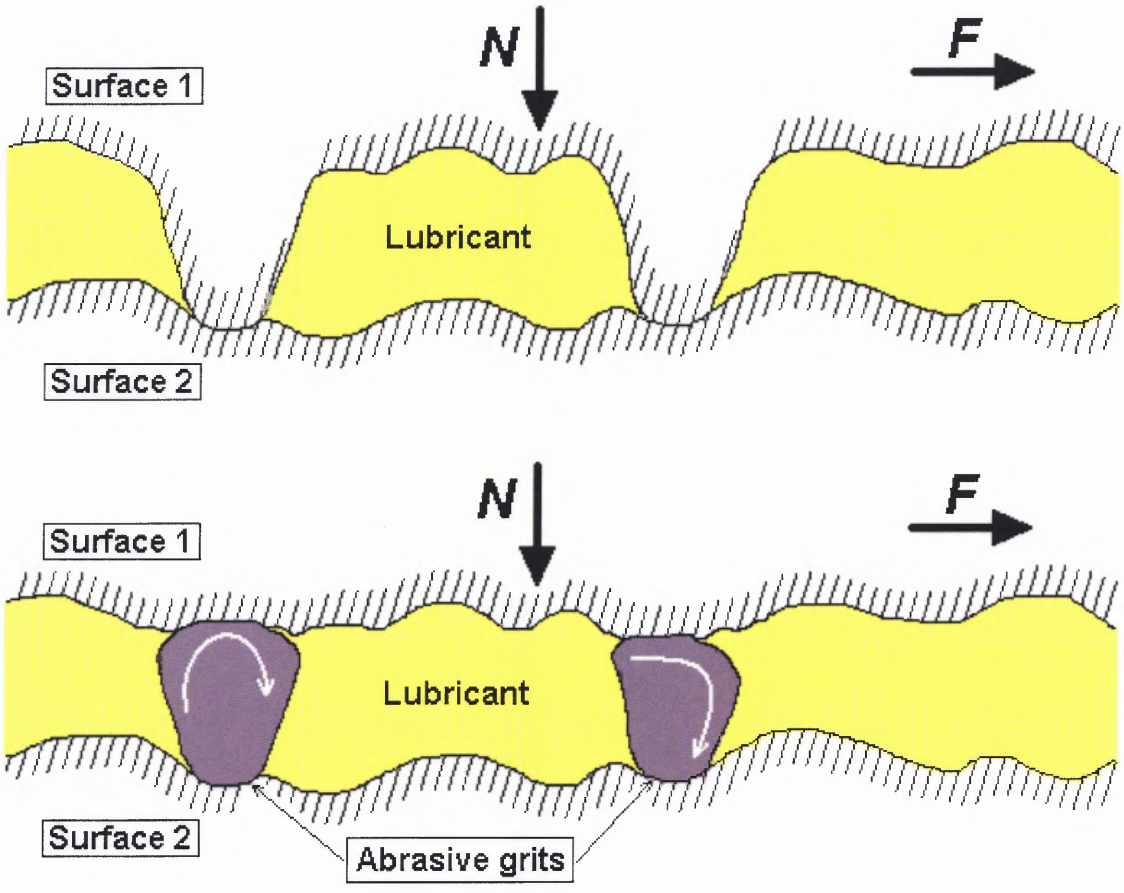

Figure 2.3 Growth mechanism of free abrasive grits.

Fatigue wear. Subsurface and surface fatigues are observed during repeated rolling (negligible friction) and sliding, respectively. The repeated loading and unloading cycles to which the materials are exposed may induce the formation of subsurface or surface cracks, which eventually, after a critical number of cycles, will result in the breakup of the surface with the formation of large segments, leaving large pits in the surface, also known as pitting. Prior to this critical point (which may be hundreds, thousands, or even millions of cycles), negligible wear takes place, which is marked contrast to the wear caused by an adhesive or abrasive mechanism, where wear causes a gradual deterioration from the start of running. Therefore, the amount of material removed by fatigue wear is

not a useful parameter. Much more relevant is the useful life in terms of the number of revolutions or time fatigue failure occurs.

Impact wear. Two broad types of wear phenomena belong under this heading: erosive and percussive wear. Erosion can occur by jets and streams of solid particles, liquid droplets, and implosion of bubbles formed in the fluid. Percussion occurs from repetitive solid body impacts. Repeated impacts result in progressive loss of solid material.

Solid particle erosion occurs by impingement of solid particles, see Figure 2.4. It is a form of abrasion that is generally treated rather differently because the contact stress arises from the kinetic energy of particles flowing in an air or liquid stream as it encounters a surface. As in the case of abrasive wear, erosive wear occurs by plastic deformation and/or brittle fracture, dependent upon material being eroded away and upon operating parameters.

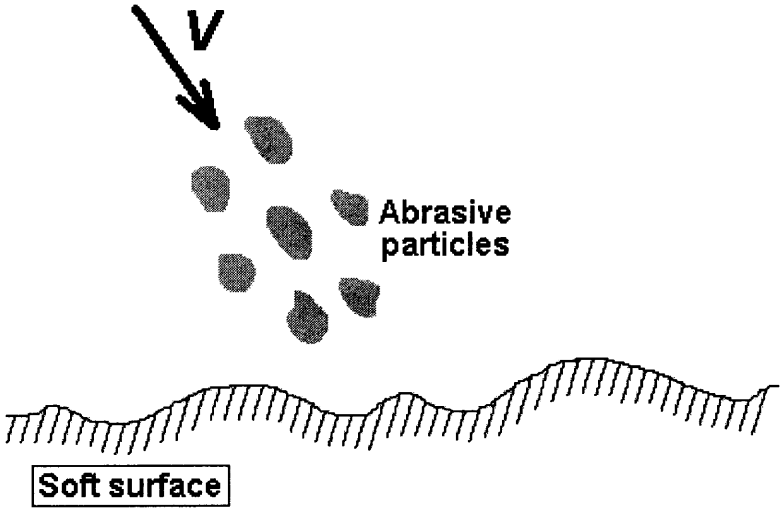

Figure 2.4 Jet abrasive particles hitting a surface at a high velocity.

Percussion is a repetitive solid body impact, such as experienced by print hammers in high-speed electromechanical applications and high asperities of the surfaces in a gas bearing. Percussive wear occurs by hybrid wear mechanisms, which combines several of the following mechanisms: adhesive, abrasive, surface fatigue, fracture, and tribochemical wear.

Chemical (corrosive) wear. Chemical or corrosive wear occurs when sliding takes place in a corrosive environment. In air, the most dominant corrosive medium is oxygen. Therefore chemical wear in air is generally called oxidative wear. In the absence of sliding, the chemical products of corrosion such as oxides would form a film typically less than a micrometer thick on the surfaces, which would tend to slow down or even arrest corrosion, but the sliding action wears the chemical away, so that the chemical attack can continue. Thus, chemical wear requires both chemical reaction (corrosion) and rubbing of surfaces in contact.

2.2 Measurement Methods of Friction and Wear

Understanding the nature of the interactions of two materials and, therefore, solving the various tribological problems heavily depend on obtaining as much as possible information about friction and wear behavior of bodies in contact. Although internal factors of frictional interaction such as changes in surface structure or roughness should be considered, friction coefficient and wear rate are two most important output factors, see Figure 2.1. The measurement of these parameters as well as friction force and weight loss of materials in contact is a fundamental task of tribologists and lubrication engineers.

Development of wear friction testing system plays important role in material and lubricant testing as well as making valid comparison with previously obtained results. Thus, the most important aspects of friction and wear testing have to be considered and analyzed. These aspects include contact geometry of bodies in contact, testing procedure and standard tests, description of friction regimes and approaches to wear assessment [2].

2.2.1 Contact Geometry

The most commonly used contact geometries for testing of components and materials are shown in Figure 2.5. Each of these contact geometries can be conforming (the contact is not a line or a point, it is some area) as well as non-conforming and has its advantages and disadvantages. For example, positive aspects of point-to-point geometry are elimination of alignment problems and opportunity to study wear from initial stages of the test, but negative feature is that the stress level of this geometry changes as the surfaces wear out.

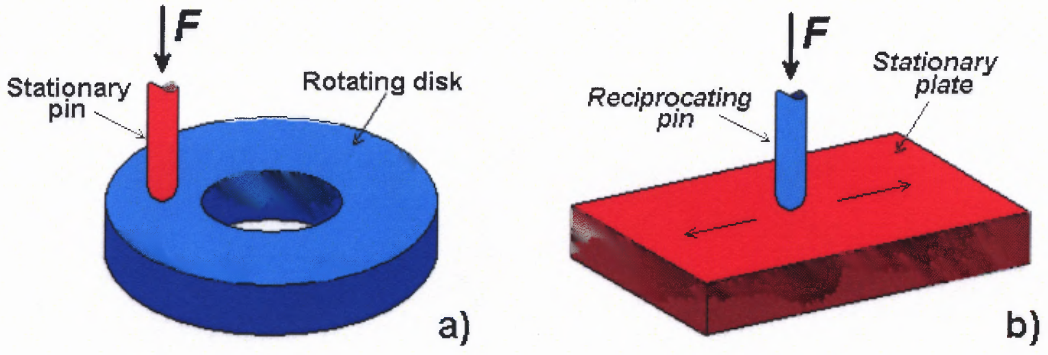

Figure 2.5 Typical contact geometries used for sliding friction and wear tests: a) pin-on-disk, b) pin-on-flat, c) pin-on-cylinder, d) thrust washers, e) pin-on-brushing, f) rectangular flats on rotating cylinder, g) cross cylinders and h) four balls.

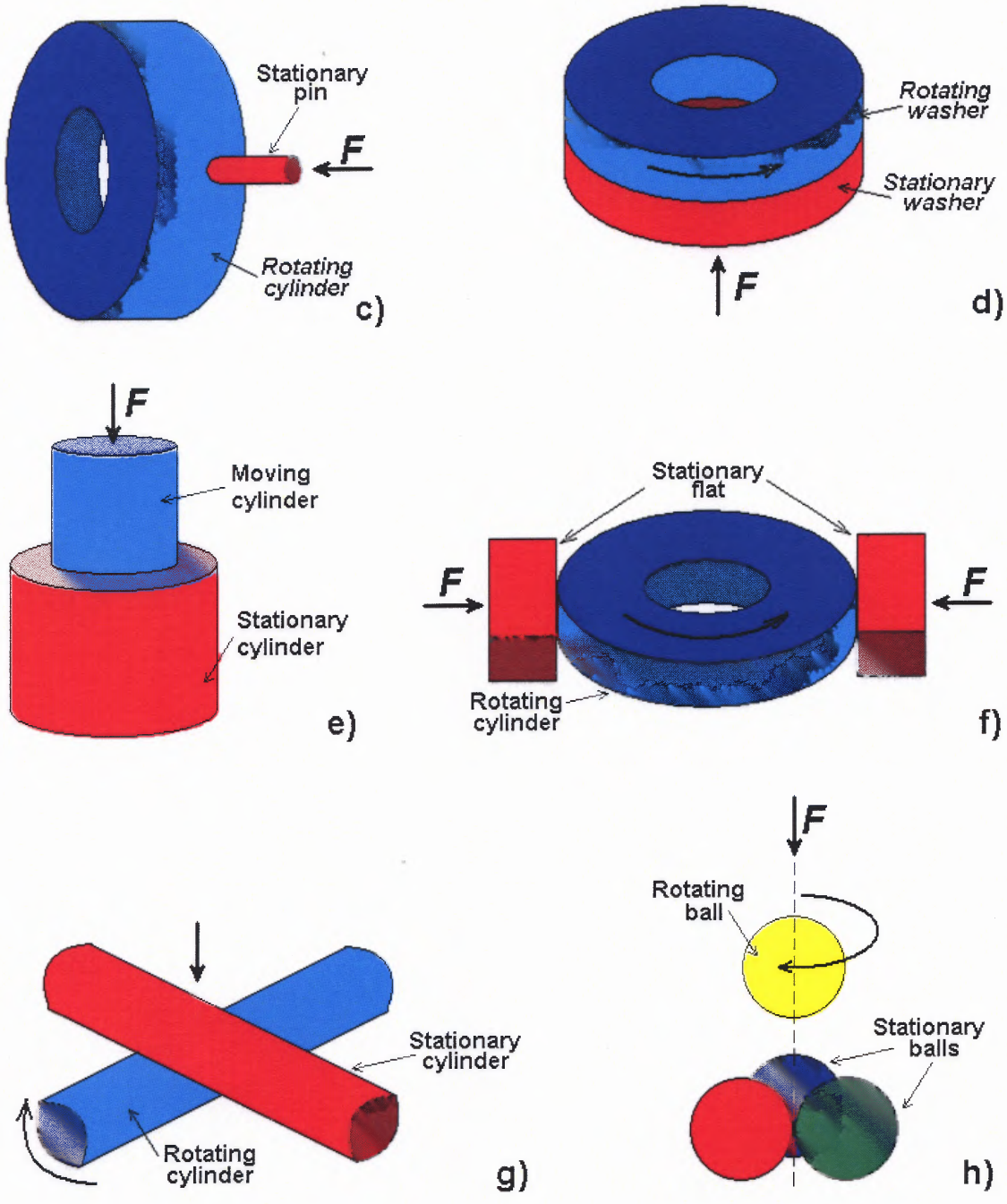

Figure 2.5 Typical contact geometries used for sliding friction and wear tests: a) pin-on-disk, b) pin-on-flat, c) pin-on-cylinder, d) thrust washers, e) pin-on-brushing, f) rectangular flats on rotating cylinder, g) cross cylinders, and h) four balls. (Continued)

Pin-on-disk. In the pin-on-disk test apparatus, the pin is stationary and the disk rotates (Figure 2.5-a). The pin can be a hemispherically tipped, a nonrotating ball, a flat-ended cylinder or a rectangular parallelepiped. This test apparatus is probably the most commonly used in tribological testing.

Pin-on-flat. In this apparatus, the flat moves relative to the stationary pin in reciprocating motion, such as in Bowden and Leben apparatuses (Figure 2.5-b). In some cases, the flat is stationary and the pin reciprocates. The pin can be a ball, a hemispherically tipped pin or a flat-ended cylinder. By using small oscillation amplitude at high frequency, fretting wear experiments can be conducted.

Pin-on-cylinder. The pin-on-cylinder test apparatus is similar to the pin-on-disk apparatus, except that loading of the pin is perpendicular to the axis of rotation or oscillation (Figure 2.5-c). The pin can be a flat or a hemispherically tipped.

Thrust washers. In the thrust-washer test apparatus, the flat surface of a washer (disk or cylinder) rotates on the flat surface of a stationery washer (Figure 2.5-d). The testers are face loaded because the load is applied parallel to the axis of rotation. This configuration is the most common for testing materials for low-stress applications, such as journal bearings and face seals.

Pin-into-bushing. In the pin-into-bushing test apparatus, the axial force necessary to press an oversized pin into a bushing is determined (Figure 2.5-e). The normal (axial) force acts in the radial direction and tends to expand the bushing; this radial force can be calculated from the material properties, the interference and the change in the bushing's outer diameter. Dividing the axial force by the radial force gives the coefficient of friction.

Rectangular flats on a rotating cylinder. In this test apparatus, two rectangular flats are loaded perpendicular to the axis of rotation of the disk (Figure 2.5-f). This apparatus includes some of the most widely used configurations such as the Hohman-6 tester. In the Alpha model LFW-1 or the Timken tester, only one flat is pressed against the cylinder. The major difference between Alpha and Timken testers is in the loading system. In the Falex tester, a rotating pin is inserted between two V-shaped (instead of flat) blocks so that there are four lines of contact with the pin. In the Almon-Wieland tester, a rotating pin is placed in between two conforming bearing shells.

Crossed cylinders. The crossed-cylinders test apparatus consists of a hallow (water-cooled) or solid cylinder as the stationary wear member and a solid cylinder as the rotating wear member that runs at the right angle to the stationary member, such as in the Reichert wear tester (Figure 2.5-g).

Although non-conforming contact geometry provides an opportunity to track friction coefficient and wear rate from the initial stages of the test, its major drawback is that the contact area and stress level of this geometry changes as the surfaces wear out. It creates some difficulties with monitoring friction and wear for extended time periods.

On the other side, conforming contact geometry generally allows mating parts to wear-in to establish uniform and stable contact geometry before taking data and, therefore, is considered excellent choice for simulation of stable friction and wear conditions. Conforming contact geometry permits to carry out prolonged experiments that simulate operational conditions of machine components in widely used mechanisms such as automobile engines and factory machines.

For the mentioned reasons, in wear friction testing machine, which is used for experimental investigation of the selected lubricants, a rectangular concave surface on a rotating cylinder with conforming contact geometry is employed. The detailed description of wear friction testing machine and contact characteristics is shown in Chapter 5.

2.2.2 Standardized Friction and Wear Tests

There are many models proposed for use in calculating friction coefficient and wear rate from system properties. However, because they invariably involve the use of information that is not readily available in handbooks or databases, these models are not widely accepted. The alternative is actual measurement of friction coefficient and wear rate.

A number of organizations have been developed standard tests for measuring friction coefficients [17]. These tests vary greatly in type and purpose. In the present day, ASTM standardized tests received the highest recognition and acceptance for the laboratory use. Some of them are designed for a particular application or material, while others are for general evaluation of materials. The most prevalent ASTM tests are:

B 460 – "Dynamic coefficient of friction and wear of sintered metal friction materials under dry conditions", material couple – friction material versus metal;

B 461 – "Frictional characteristics of sintered metal friction materials run in lubricants", material couple – friction materials versus metal;

B 526 – "Coefficient of friction and wear of sintered metal", material couple – friction materials versus gray cast iron;

D 1894 – "Static and kinetic coefficients of friction of plastic films and sheeting", material couple – plastic film versus stiff or other solids;

D 2047 – "Static coefficient of friction of polish coated floor surfaces as measured by the James machine", material couple – flooring materials versus shoe heels and soles;

D 2714 – "Calibration and operation of Alpha model LFW-1 friction and wear testing machine", material couple – steel ring versus steel block;

D 3028 – "Kinetic coefficient of friction of plastic solids and sheeting", material couple – plastic sheets or solids versus other solids.

Test *D 2037* was selected as the base test for the development of wear friction testing machine described in Chapter 5. The beneficial aspects of this test are material couple, flat-on-cylinder contact geometry and measured parameters. The test conditions that require applied normal load of 22 N and angular velocity of 7.54 s^{-1} (72 *RPM*) have been change to variable applied load and angular velocity of 23.9 s^{-1} (229 *RPM*). These changes provide some flexibility for testing procedure and make the designed computer controlled wear testing machine the key element of lubricant testing under boundary lubrication conditions.

2.2.3 Friction Regimes

Dependence between wear of surface in contact and friction coefficient for different systems is shown in Figure 2.6. This figure illustrates: a system that experiences insignificant wear or changes in behavior when wear occurs (a), a system where friction force increases with time until reaching a steady-state condition (b) and a system where friction force varies with each event in the wear process (c).

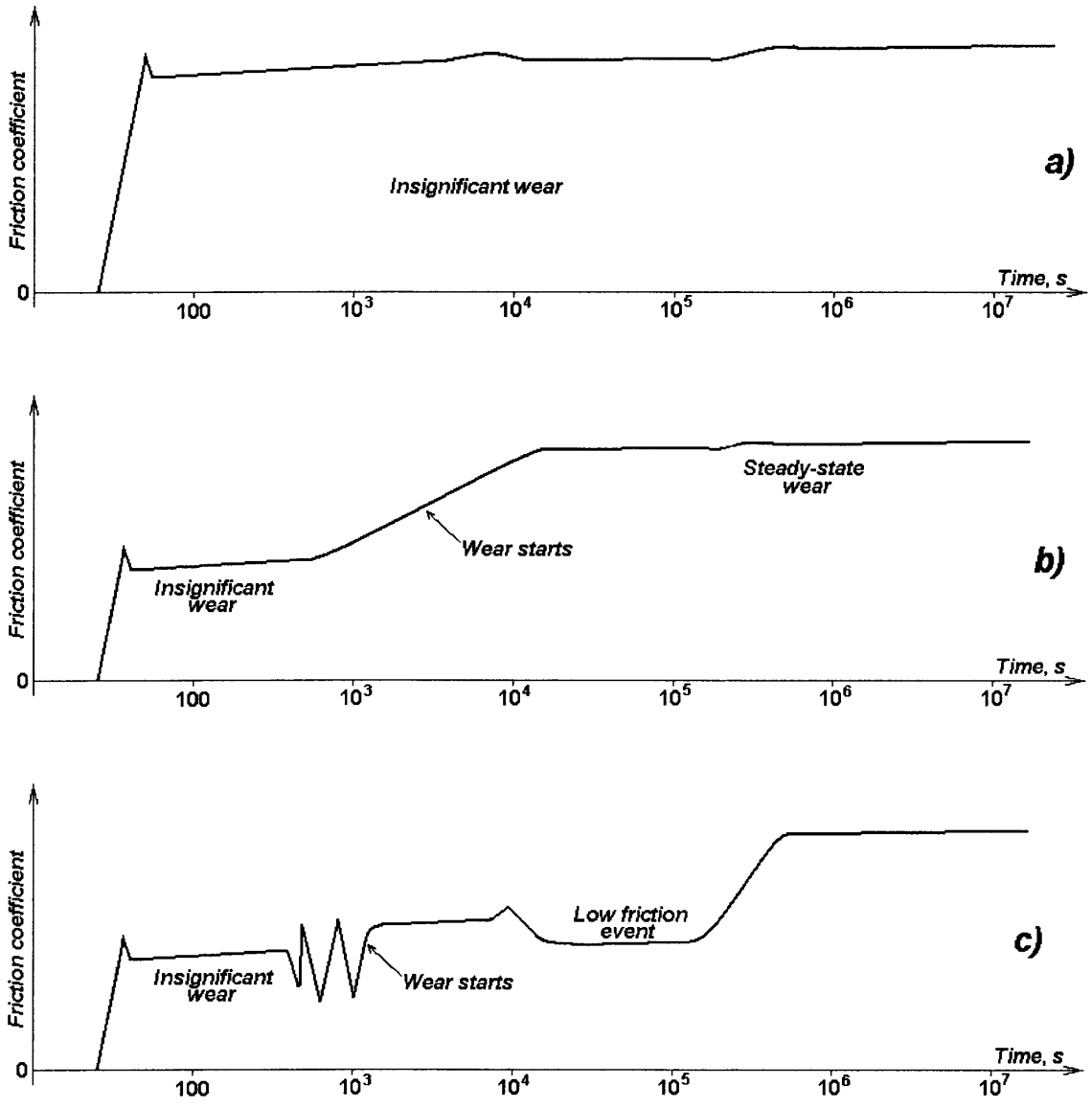

Figure 2.6 Effect of system wear on friction force: a) insignificant wear, b) steady-state wear and c) friction force varies with each event.

Each of the shown regimes can be encountered in various engineering applications. Figure 2.6-a shows the behavior of friction coefficient under stable conditions, which are the most beneficial for operation of machine components. This regime is characterized by stable friction coefficient as well as wear rate. Development of

these conditions reproduces common operation of moving parts and allows tracking friction test characteristics for extensive time periods.

2.2.4 Wear Rate

There is no single standard way to express wear rate. The units used depend on the type of wear and the nature of the tribosystem, in which wear occurs. Wear rate can be expressed [18] as (1) volume of material removed per unit time, per unit sliding distance, per revolution of a component or per oscillation of a body (that is, in sliding wear), (2) volume loss per unit normal force per unit sliding distance ($mm^3/N{\cdot}m$, which is sometimes called the wear factor), (3) mass loss per unit time, (4) change in a certain dimension per unit time or (5) relative change in dimension or volume with respect to the same changes in another (reference) substance. The manner of expressing wear rate is sometimes prescribed in specific standard test methods. In other cases, standards are established for given sectors of technology.

2.2.5 Test Preparation

The procedural considerations should be addressed to ensure that test procedure would produce valid data [2]. Friction is a system property and systems must be modeled carefully – same test parameters, same materials, same treatment and so forth. The factors that play vital role in setup of friction test include design methodology, sample preparation, friction and wear measurements and interpretation of data. Although simulation is the most critical issue, other issues should also be thoroughly studied.

Proper simulation ensures that the wear mechanism experienced in the test is identical to that of the actual system. Given the complexity of wear processes and the

incomplete understanding of wear mechanisms, test development is subject to trials and errors and is dependent on the capabilities of the investigator. A successful simulation requires similarity between the functions of the actual system and those of the test system, that is, similarity of inputs and outputs and of the functional input-output relations. To obtain this similarity, selection of the test contact geometry is a critical factor in simulating wear conditions. Other factors that significantly influence the success of a simulation include type of motion, load, speed, lubrication conditions and operating environment.

Operation testing is inexpensive and fast method of troubleshooting. However, if it is not done properly, the wear mechanism to be simulated may change. Wear change is normally caused by increase in load, speed or temperature, by decrease in lubricant supply on contact surfaces or by changes in other indirect factors.

Specimen preparation plays a key role in obtaining repeatable/reproducible results. For metals, surface roughness, geometry of the specimen, microstructure, homogeneity, hardness and the presence of surface layers must be inspected carefully for both contact materials. Similar controls are necessary for the wear-causing medium. For instance, in an abrasive wear test, purity, particle size, particle shape and the moisture content of the abrasive must be controlled.

2.2.6 Contemporary Tribotesters

Today the market of friction and wear testing apparatuses offers a selection of various products that allow not only to track changes in friction coefficient and wear rate, but also to control such factors as sample geometry, applied load, sliding velocity, ambient temperature and humidity. Wear and friction testing machines based on different

interface geometries are produced by such companies as Falex – Le Valley Corporation, USA, Cameron Plint Tribology, UK, Center for Tribology, USA, Optimol Instruments GmbH, Germany, and CSEM, Switzerland.

However, testing is not limited to the equipment produced by the industrial companies. For certain applications, new types of wear and friction testing equipment on the base of described geometries and principles are often designed. Such applications include boundary lubrication, simulation of special contacts of machine components and other applications.

2.3 Lubrication Regimes, Types of Lubricants and Oil Oxidation

2.3.1 Lubrication Regimes

The four distinct regimes of lubrication are hydrodynamic, mixed, boundary and dry lubrication. The relationship among first three regimes is shown by Stribeck curve, see Figure 2.7. This curve illustrates the relationship between coefficient of friction and dimensionless number ($\eta \cdot U/P$), where η is the dynamic viscosity, U is the speed (revolutions per minute for a journal), and P is the load per unit of projected area [18]. As can be seen in this graph, even insignificant changes in η, U or P can lead to substantial changes in friction coefficient and the lowest value of friction coefficient is in hydrodynamic lubrication, an excellent regime for any two parts in relative motion. The friction coefficient in this regime is much lower than that in boundary lubrication.

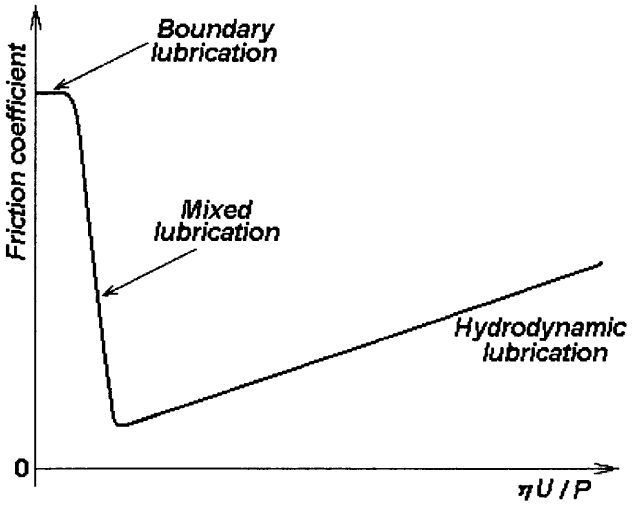

Figure 2.7 Stribeck curve shows the dependence of lubrication regime on the dimensionless number $\eta \cdot U/P$.

In hydrodynamic lubrication, the pressure in the narrow converging gap between bodies in contact enables a load to be transmitted between the surfaces with very low friction, since the surfaces are completely separated by a film of fluid [2], see Figure 2.8. In this situation, it is the physical properties of the lubricant, mainly the dynamic or absolute viscosity, that dictate the behavior of the contact. Thus, lubricant films are normally many times thicker than the surface roughness. The film thickness normally exceeds 10^{-6} *m*.

The other most common lubrication regime is boundary lubrication. In this lubrication regime, the solids are not separated by lubricant; thus, fluid-film effects are negligible and there is considerable asperity contact, see Figure 2.9.

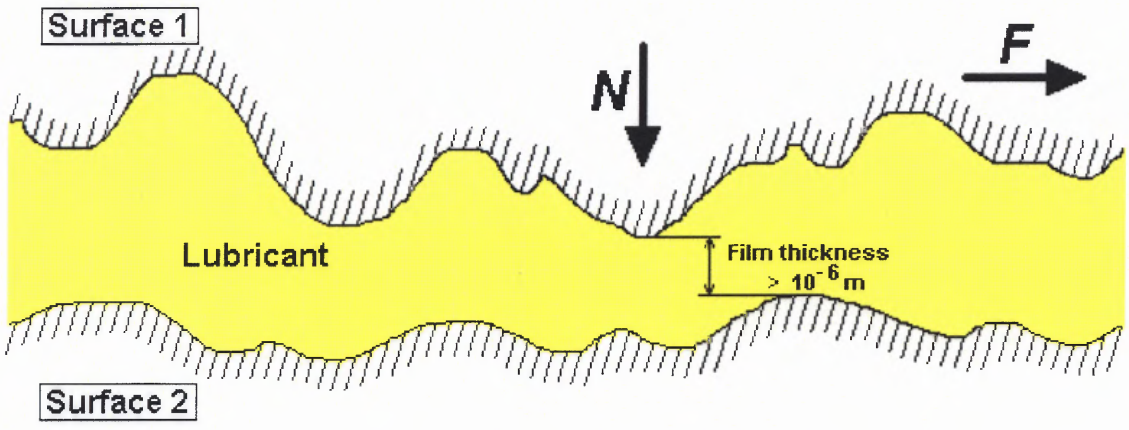

Figure 2.8 Hydrodynamic lubrication.

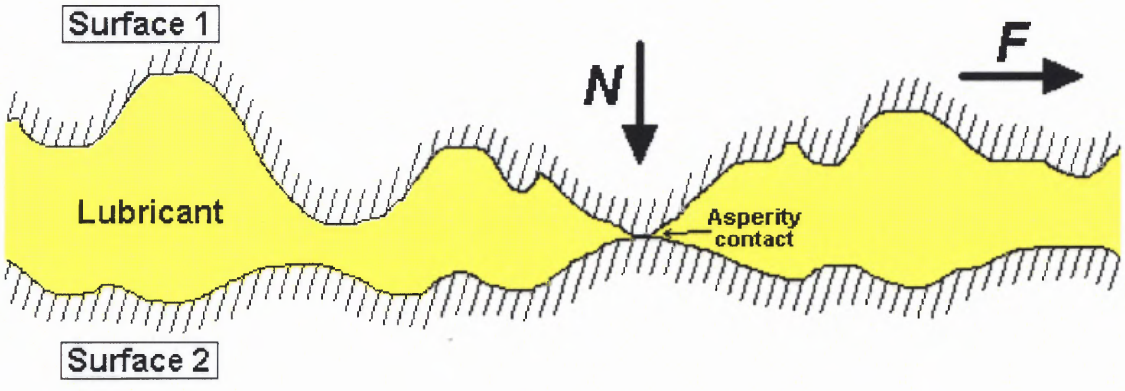

Figure 2.9 Boundary lubrication.

The properties of bulk lubricant are of minor importance, and the coefficient of friction is essentially independent of the viscosity of the fluid. The frictional behavior is similar to that encountered in dry friction between two solids. The surface films vary in thickness from 5×10^{-9} to 10^{-8} *m*.

Although hydrodynamic regime is the most practical lubrication regime, under some conditions, such as extreme pressures, low running speed or high surface roughness, penetration of the lubricant film occurs and boundary lubrication takes place.

Usually, this happens in the start and stop moments of machine running. The transition from hydrodynamic lubrication to boundary conditions is marked by a drastic change in wear rate.

2.3.2 Mineral Oils

The goal of lubricants, as previously discussed, is to physically separate two surfaces in relative motion to one another and prevent direct contact of rubbing surfaces. Industrial machinery lubricants must, therefore, be suitable, depending upon the particular application, either for hydrodynamic or boundary conditions (or sometimes mixture of the two). Common requirements for many industrial liquid lubricants used in different applications are chemical and thermal stability, friction reduction and load carrying ability (including extreme pressure lubrication).

Due to the use of increased loads, speeds and temperatures, which have come about by the development of greater efficiency of industrial design, increasing requirements are applied on the lubricating oils. Although the majority of industrial applications can still be adequately met by mineral oil products, in some special applications specially that require fire-resistance of lubricating oil, it has become necessary to use synthetic oils. Although synthetic oils are excellent for many applications in the technological point of view, and appear to be an obvious choice, they are not always economically viable [19].

Mineral oils are mixtures of vast number of hydrocarbons, but small amounts of sulphur and traces of nitrogen and oxygen compounds may be present. The composition of the hydrocarbon mixture may largely vary. However, most oils are mixtures of paraffins, naphthenes and aromatics, see Figure 2.10. The paraffinic oils are more

resistant to oxidation than the aromatic oils, but when oxidation is not a problem, the unsaturated ring type structures of the aromatics allows them to absorb greater quantities of energy before break-down occurs. This specific advantage of aromatic oils is exploited in the nuclear power field where lubricants are subjected to radiation in their working environment. It is also used, for example, in the field of high temperature transfer where the better thermal stability of the aromatic type oils becomes advantageous. However, when the oxidation stability of the oil is more important than its thermal stability, for example, in a quenching oil bath, then the paraffinic type of oil is preferred to the aromatics. In low temperature applications, such as refrigerator oils, the use of predominantly naphthetic type oils has been traditionally preferred.

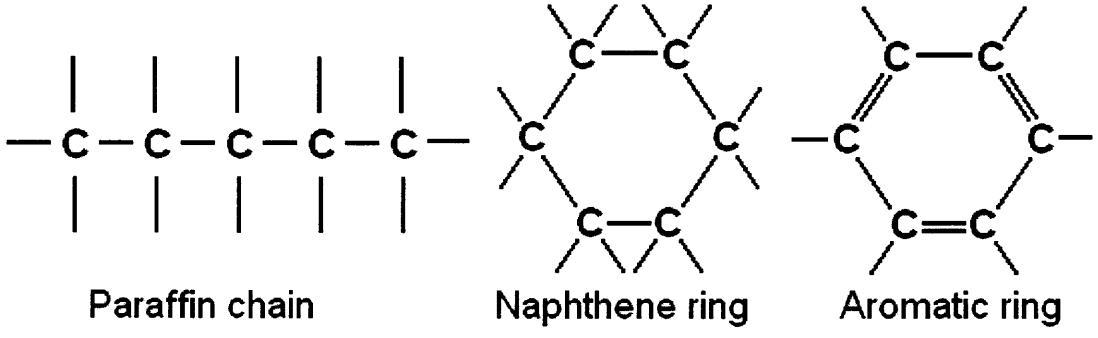

Figure 2.10 Hydrocarbon types.

The selection of lubricant grade, for a specific application, will often be influenced by the general state of the machinery and its age and past service record. Without doubt, the most important single physical characteristic of the oil selected will be friction coefficient, which depends on molecular weight of lubricant molecules [20], see Table 2.1.

In many traditional applications, the selection of certain oil may not be enough to cope with working conditions imposed on it and, thus, additives are usually used to enhance lubricant properties. The main types of additives used in mineral oils are the oxidation inhibitors, rust and corrosion preventives, anti-foam agents, load carrying and frictional characteristic improvers, pour point depressants and viscosity index improvers and anti-wear agents.

Table 2.1 Dependence of Friction Coefficient on Molecular Length of Lubricants (clean glass on glass, $f = 0.94$)

Material	*Coefficient of Friction*	*Molecular Weight*	*Formula*
Pentane	0.71	72.09	$C_5 H_{12}$
Hexane	0.69	86.11	$C_6 H_{14}$
Heptane	0.68	100.12	$C_7 H_{16}$
Octane	0.66	114.4	$C_8 H_{18}$
Undecane	0.58	156.19	$C_{11} H_{24}$
Nondecane	0.42	268.32	$C_{19} H_{40}$
Tetracosane	0.33	338.39	$C_{24} H_{50}$

2.3.3 Oil Oxidation

Oxidation is one of the most important problem of lubricants. Present day refining techniques yield oils of excellent oxidation stability, especially if they are of paraffinic origin. However, oil oxidation is inevitable process for any lubricant, which operates in oxygen content environment. Oil oxidation cannot be prevented, but it can be slowed

down. Even slight deceleration of oxidation process will give essential savings in operating expenses of machine components [22].

The main idea of oil oxidation is shown in Figure 2.11. Hydrocarbons, which are the base of any lubricants, under sufficient thermal extent, react with oxygen and the products of this reaction are oil soluble hydroperoxides such as aldehydes, ketones and acids [19]. Future oxidation turns them into oil insoluble gums and sludges, which cause essential damage to the surfaces in contact.

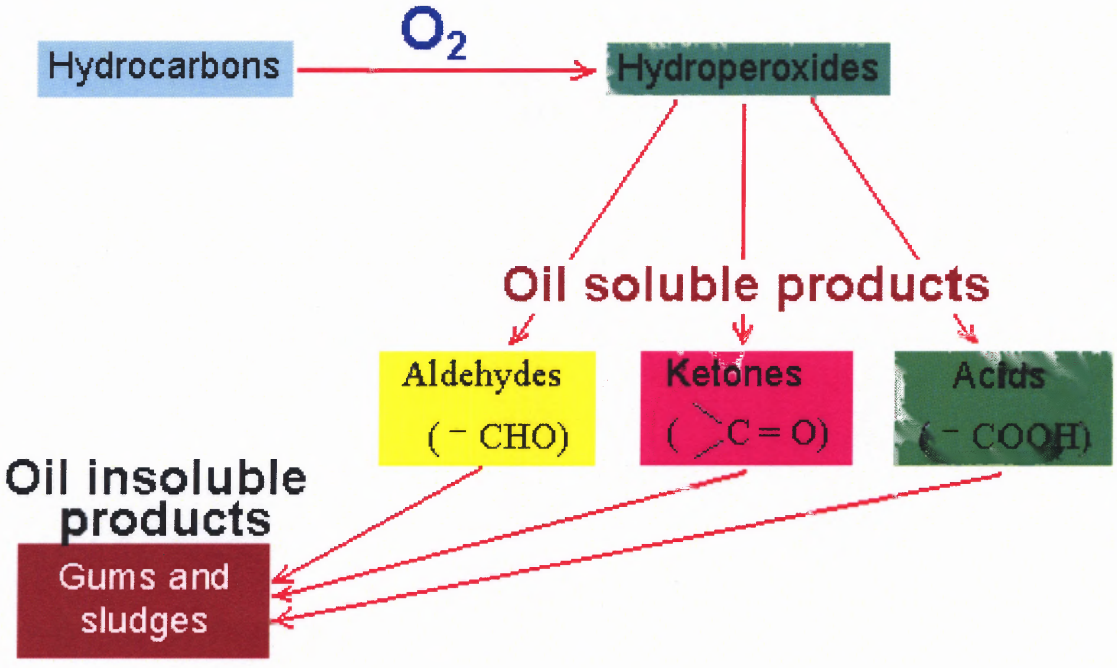

Figure 2.11 Mechanism of oil oxidation.

Oxidation related processes lead to loss of viscosity and loss of load carrying capacity of operating oils. Additives proposed today increase thermal stability of lubricants and reduce their degradation rate, but still lubricant degradation can be

reduced. The new approach is the use of new more stable chemical molecules that have lower degradation rate under oxygen influence. Nowadays, there are many works [21-23], which describe the use of fullerenes as lubricant additives – fullerenes posses the qualities that necessary to act as antiwear agent as well as oxygen inhibitor. The behavior of C_{60} films deposited on various surfaces was studied in oxidation tests [24, 25], which show that fullerene C_{60} has strong capability of bonding oxygen, thus, decreasing the oxygen concentration in the ambient medium.

Use of fullerenes, particularly C_{60} and C_{70}, as lubricant additives, opens great perspectives. Fullerenes can be easily dissolved in oils as well as in solvents such as toluene and benzene. The main advantages of fullerenes are their low surface energy, high chemical stability, spherical shape, weak intermolecular bonding and high load bearing capacity. These properties of C_{60} molecules offer potential for their various mechanical and tribological applications.

2.4 Lubricant Additives

The primary function of lubricant is to control friction, wear and surface damage over the intended life of a system that contains machine elements, such as gears and bearings. Other lubricant functions are prevention of surface corrosion and diminishing of heat, dirt and wear debris effects.

The choice of a base lubricant and appropriate additives depends on application, cost and health, safety and environmental considerations. Mineral oils have good characteristics and are less expensive than synthetic lubricants. Thus, additives help lubricants to get desired properties without significant effect on the product final price.

The amount of additive used in lubricants can vary from a few hundredths of a percent to 30 % and more. Some additives that offer advantages in one performance area may be destructive in other areas, whereas other additives work best in combination.

2.4.1 Types of Lubricant Additives

The widely used types of additives and their functions are following. Dispersants are additives that are used to suspend oil-insoluble resinous oxidation products and disperse contaminants in the bulk oil. Detergents perform functions that are similar to those of dispersants as well as neutralize acidic combustion and oxidation products, and hence, control rust, corrosion and resinous built-up in the engine. Rust and corrosion inhibitors help to prevent the damage done to metal surfaces by the attack of atmospheric oxygen and acidic products. Emulsifiers are chemical compounds that enable two immiscible fluids to form an intimate mixture known as an emulsion. Foam inhibitors slow down foam formation by changing the surface tension of the oil and by facilitating the separation of air bubbles from the oil phase. The principal function of a viscosity improver is to minimize viscosity variations with temperature. Oxidation inhibitors function by circumventing the radical chain mechanism of the oxidation process. Antiwear additives function by thermal decomposition and by forming products that react with the metal surface to form a solid protective layer.

Lubricant additives can be categorized as either chemically active or chemically inert [17]. Chemically active additives such as dispersants, detergents, antiwear and extreme pressure agents, oxidation inhibitors and rust and corrosion inhibitors, have an ability to chemically interact with metals to form a protective film and with polar oxidation and degradation products to make them harmless. Chemically inert additives,

which improve the physical properties critical to the effective performance of the lubricant, include emulsifiers, pour-point depressants, foam inhibitors and viscosity improvers.

Most lubricant additives, except some viscosity improvers and pour-point depressants, consist of an oleophilic hydrocarbon group and a hetero-atom (*N*, *O*, *S* and *P*) – based polar functionality. The hydrocarbon group has sufficient carbon length to deliver the desired solubility characteristics to the additive. The additives that require greater solubility in oil (dispersants, detergents and viscosity improvers) usually contain large hydrocarbon groups. Those that require either lower solubility or greater surface activity (foam inhibitors and extreme pressure agents) contain small hydrocarbon groups.

The major role in improving lubricant properties under boundary lubrication conditions is played by oxidation inhibitors and antiwear additives. Prevention of direct contact and development of protective layer are the primary goal of antiwear additives. Besides, reduction of oxygen effect in hot temperature zone of asperity contact can significantly decrease wear of contact surfaces under boundary lubrication conditions. Detailed description of oxidation inhibitors and antiwear additives is represented in the following chapters.

2.4.2 Oxidation Inhibitors

Due to their hydrocarbon base, all present lubricants are susceptible to oxidation [26, 27]. Each type of base stock (mineral or synthetic) has a stable threshold, beyond which stabilizers or oxidation inhibitors are needed to retard oxidation. High operating temperature and high air exposure applications make oxidation processes in the operating lubricant inevitable. During the initial stage, the lubricant reacts with oxygen to form free

radicals. During the propagation stage, these radicals react with the oxygen and the lubricant to form hydroperoxides. The hydroperoxides decompose to form a variety of additional radicals and oxygen-containing compounds. During the termination stage, the radicals either self-terminate or terminate by reacting with other lubricant compounds.

Today, oxidation inhibitors function by circumventing the radical chain mechanism of the oxidation process. Oxidation inhibitors can be classified as hydroperoxide decomposers and radical scavengers. The hydroperoxide decomposers convert the chain-propagating hydroperoxides to alcohols while getting themselves oxidized to higher oxidation levels. The radical scavengers remove the radicals from the oxidation process by transferring a hydrogen atom to the radical, thereby making it innocuous. Because radical scavengers act in the initial stage of lubricant decomposition, they are considered more effective means in oil oxidation.

Under boundary lubrication conditions, oil oxidation and lubricant decomposition processes are unavoidable and special attention should be paid to binding free radicals in the initial stage and preventing development of hydroperoxides. For solving these problems, fullerenes possess two qualities that are important to help free radicals to bind into new chemical compounds – high absorption ability and spherical shape. Because of high absorption ability, fullerenes bind fast neighbor free radicals developing "moss" around their spherical molecules, which does not significantly affect molecular strength of fullerene molecules. Spherical shape of fullerenes increase chances of development of new chemical compounds out of radicals bound to the fullerene surface. A schematic representation of free radical absorption by fullerene molecules and further development of new chemical compounds from these radicals is shown in Figure 2.12.

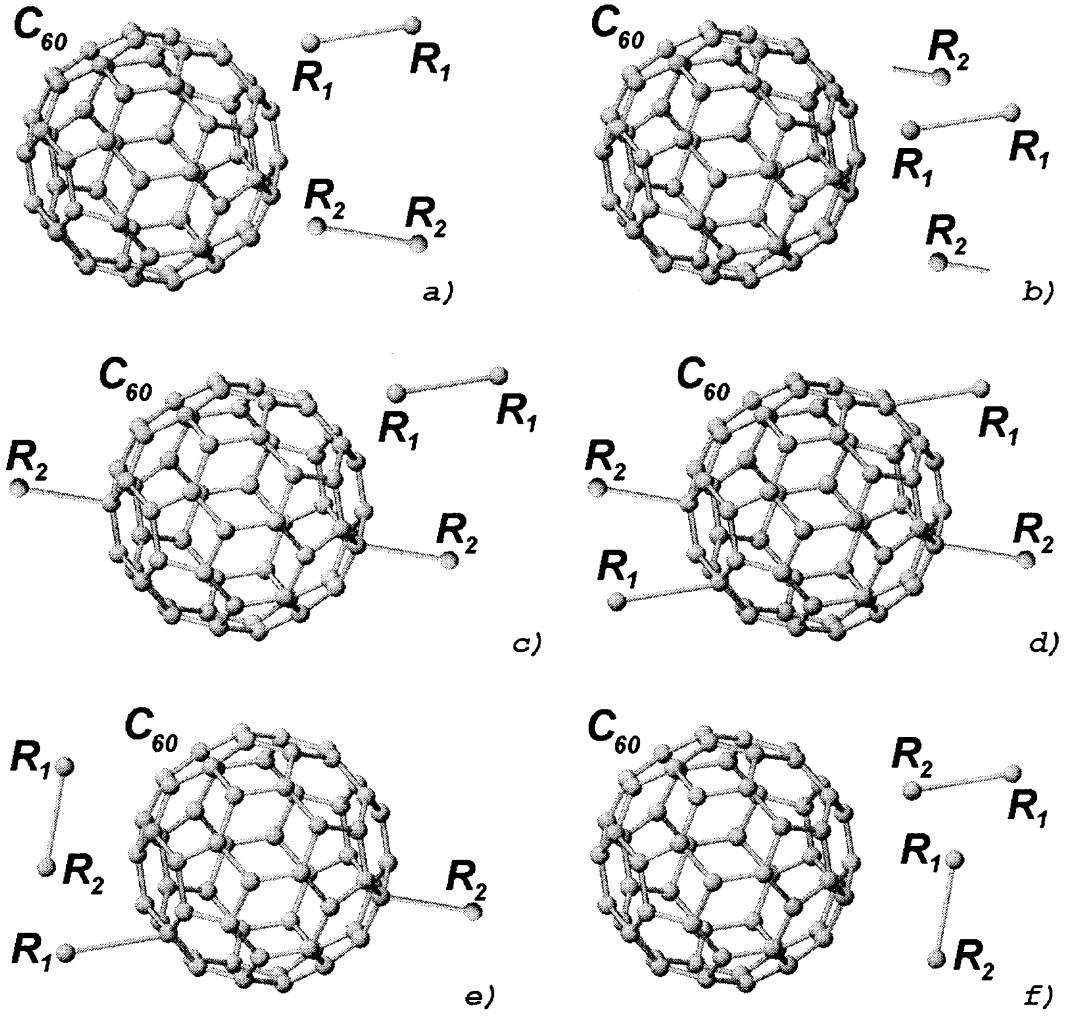

Figure 2.12 Schematic representation of functionalization of fullerene C_{60}: a) initial state of fullerene and radicals R_1 and R_2, b) in working conditions radicals break into parts, but fullerene stays untouched, c) free radicals start binding to fullerene, d) the process of breaking radicals and their binding to fullerene continues, e) radicals bound to fullerene start reacting to each other and f) all radicals bound to each other and clean fullerene surface for possible future reactions.

Spherical shape of their molecules gives fullerenes strong advantages over existing lubricant additives such as graphite. Although graphite has the same benzene structure, see Figure 2.13, and binds free radicals in the same way as fullerenes do, it has much lower absorption ability due to its laminar structure. Due to large distance between layers, jumps of free radicals from one layer to another are regarded as problematical.

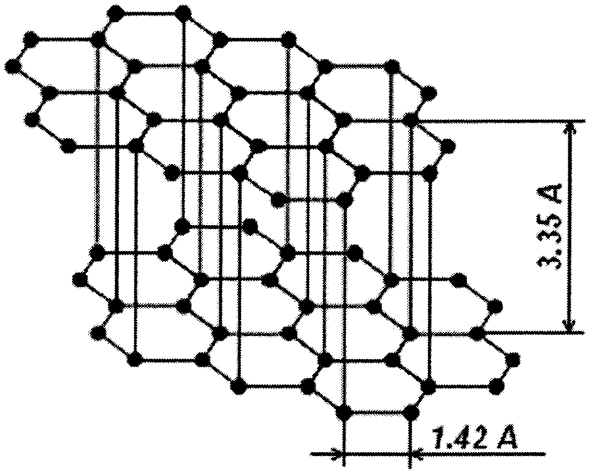

Figure 2.13 Graphite structure.

In comparison with phenols and arylames, fullerenes look more beneficial due to their strong molecular bonding and an ability to clean up their surface. Phenols and arylames have some limit in binding free radicals and over its limit become a burden for the lubricant. Unlike them, fullerenes can function as radical scavengers long time that lengthen their life as oxidation inhibitors.

2.4.3 Antiwear Additives

Antiwear additives offer protection under boundary lubrication conditions [28]. They function by thermal decomposition and by forming products that react with metal surface to form a solid protective layer. This solid metal film fills the surface asperities, thus reducing friction and preventing welding and surface wear. Depending on the antiwear agents, the metal film consists of iron halides, sulfides or phosphates.

Dithiophosphoric acid zinc salts are the most widely used antiwear additives. They are primary used in gasoline and diesel engine oils and in industrial lubricants. Zinc

dialkyl dithiophosphates or diaryl dithiophosphates are synthesized by chemical reaction of dithiophosphoric acids with zinc oxide.

The thermal and hydrolytic stability of these products depends on the nature of the organic group. The dialkyl dithiophosphates derived primary from alcohols are more thermally stable than those derived from the secondary alcohols. Although the diaryl dithiophosphates are the most thermally stable of this family, hydrolytically they are the least stable. They are not very effective and therefore not often used as antiwear agents. Dithiophosphate derivatives decompose (generally below 200 ^{o}C or 390 F) to form thiols, olefins, polymeric alkyl thiophosphates and hydrogen sulfide [29, 30].

Most antiwear additives contain sulfur, chlorine, phosphorus, boron or their combinations. Molybdenum disulfide and graphite are common examples that are generally used in greases, some industrial oils and various break-in lubricants. In general, antiwear agents are commonly used in engine and gear oils, automatic transmission fluids, power steering fluids and tractor hydraulic fluids.

Properties that may make fullerenes successful antiwear additives are spheroid shape, high elasticity and high load carrying capacity of their molecules. Different from the lubrication mechanism of widely accepted antiwear additives, fullerenes are expected to act as minute firm balls, which cannot be easily squeezed out from the contact. Due to fullerene chemical stability, they do not react with metal surface, but fill the surface asperities reducing friction and surface wear. Detailed consideration of fullerenes behavior in lubricant is covered in Chapter 7.

2.5 Overview of Fullerenes

Until recently, carbon was believed to exist in only two forms, diamond and graphite, but now a third previously unknown form – fullerene, buckminsterfullerene or buckyball – has been discovered. Since Sir Harold W. Kroto, Robert Curl, Jr. and Richard Smalley received Nobel Prize in Chemistry "for their discovery of fullerenes", fullerenes have been attracting scientists all over the World and increasing their attention to studies on their syntheses, properties and possible applications. The number of atoms in a fullerene molecule can be *2n*, where *n* is any integer number. Among a large variety of fullerenes (C_{24}, C_{28}, C_{32}, C_{80} and others), the most studied and easily produced ones are C_{60} and C_{70}, see Figure 2.14.

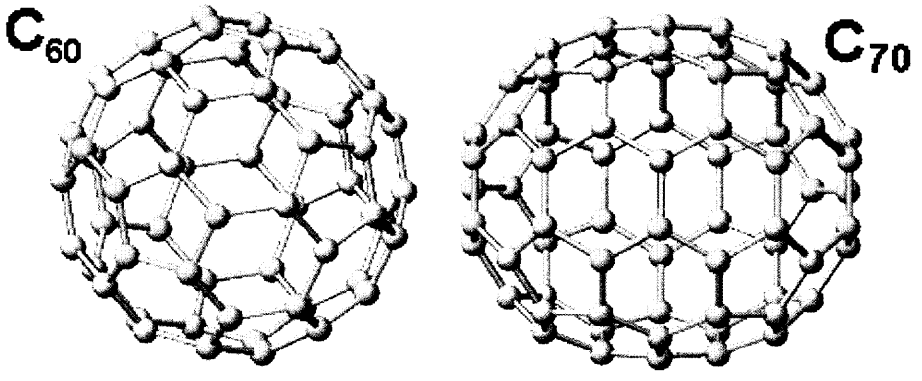

Figure 2.14 Structure of fullerene molecules.

Fullerene molecules have a form of hallow geodesic domes. All molecules are networks of pentagons and hexagons with covalently bonded carbon atoms. It has been reported that besides a certain number of hexagons, any fullerene must have precisely 12 pentagons in order to close into a spheroid and fullerene molecules may have carbon

numbers ranging from 32 to 960 [31]. However, the most stable molecules are C_{60} and C_{70}. The structure of C_{60} molecule has 20 hexagons in the dome taking the highest possible symmetry for any molecule (icosahedral) that assumes the shape of a soccer ball. The structure of C_{70} has 25 hexagons, producing a shape reminiscent of a rugby ball. The two interatomic distances within a C_{60} molecule are 0.140 *nm* between two carbon atoms shared by adjacent hexagons and 0.145 *nm* between the two carbon atoms shared by a hexagon and a pentagon. The C_{60} molecule forms a hallow carbon cage of 0.71 *nm* in diameter [32, 33]. One-dimensional arrangement of C_{60} molecule [34] is shown in Figure 2.15. Like other aromatic molecules, carbon atom in this new geodesic form is bonded to only three other atoms being satisfied in a strong double bond, delocalized over the geodesic sphere. All single bonds are strong covalent bonds. As the bonds in the C_{60} structure are examined, carbon-to-carbon bonds in the pentagon subunits are single bonds while alternate bonds in the hexagonal subunits are double bonds. It is further noted that to maintain the aromatic network, pentagonal subunits are not placed to each other.

Wilson and others [37] have shown that molecules in evaporated C_{60} films tend to order in hexagonal arrays. Based on scanning tunneling microscopy of C_{60} molecules, Bhushan and others [36] observed the atomic configuration of a C_{60} molecule and showed that solvated films consist of spherical clusters aggregate of molecules. X-ray diffraction studies of the single crystal of fullerenes show that at room temperature, the spheres, or C_{60} molecules, are packed in a face-centered cubic (FCC) lattice with the nearest neighbor distance, between two cage centers, of 1.003 *nm* and a lattice constant of 1.4198 *nm* [31]. The molecules in the FCC lattice are bonded by weak Van der Waals attractions. Carbon-13 NMR measurements of this solid form revealed that the fullerenes

are spinning freely even in the crystal lattice, at speeds over 10^8 revolutions per second. This motion is frozen out upon going to 77 *K*. A phase transition occurs to simple cubic near 253 *K* [37, 38].

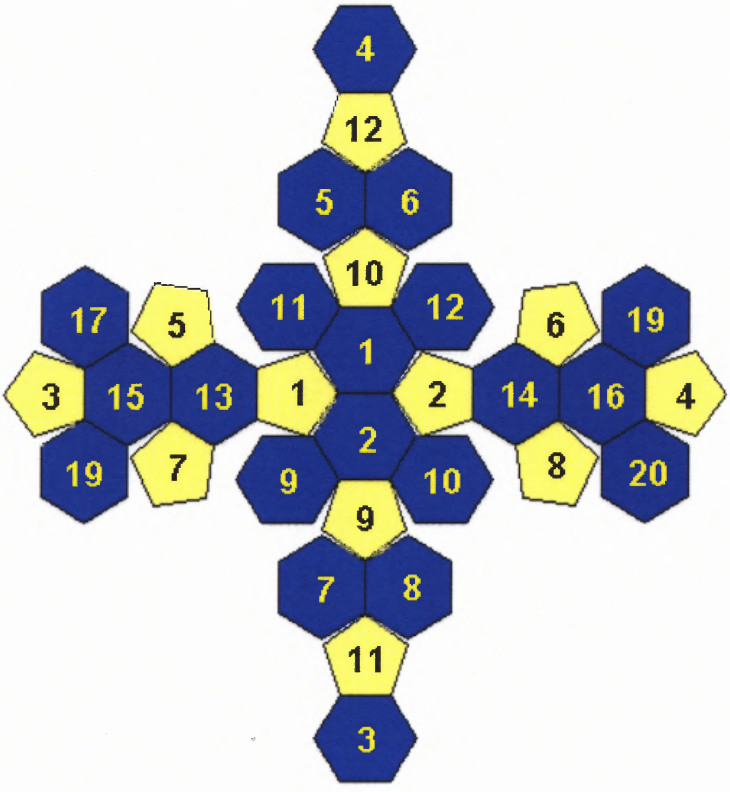

Figure 2.15 One-dimension arrangement of a molecule of C_{60}.

The fullerene C_{60} is a blackish powder. It sublimes readily at temperatures above 450 ^0C and dissolves in a wide range of solvents. Since C_{60} sublimes and is soluble at room temperature, it is unique among all other forms of pure carbon available. C_{60} is stable in air. When sublimed, C_{60} is found to produce yellow-gold colored film of excellent cohesive quality on a wide range of substrates. The fullerenes readily form crystals with a density of about 1.7 $g\ cm^{-3}$. Frum and others [39] reported the infrared spectrum of a C_{60} sample after heating above 500 ^oC differs from that of the original

material which suggests that C_{60} lattice structure may not be stable above 500 ^{o}C. The FCC phase of solid C_{60} remains stable under hydrostatic compression to at least 20 *GPa*, with an atmospheric-pressure isothermal bulk modulus of 18 *GPa*. However, under non-hydrostatic compression, a transition to a crystallographic structure of lower symmetry is observed at about 16 *GPa* [37]. Based on experimental evidence, Regueiro and others [41] reported that non-hydrostatic compression of C_{60} to a pressure of 20 ± 5 *GPa* transforms it instantaneously into bulk polycrystalline diamond at room temperature.

Since the C_{60} molecules are bonded with Van der Waals forces, the fullerene crystals are expected to be as soft as graphite. Based on nanoindentation measurements conducted using atomic force microscope, Ruan and Bhushan [42] have shown that fullerene clusters are loosely bonded and can be indented readily. However, at high pressures, approximately 20 *GPa*, they are expected to be very hard because of its phase transformation [41]. These experiments suggest that fullerene molecules can carry heavy loads.

The index of refraction of solid C_{60} is 2.2 at 630 *nm* wavelength, cohesive energies per C_{60} molecule and per atom are 1.5 *eV* and 7.4 *eV*, respectively, and the ionization potential is 7.6 *eV* [32]. As such, it is highly insulating at room temperature, but like all semiconductors, the conductive and photoconductive properties of these new materials should be highly sensitive to small amounts of dopants. Numerous researchers are doping fullerenes to change their properties, for example, to make them superconducting by doping with alkali metals. Selig and others [43] has produced fully fluorinated fullerenes (C_{60} F_{60}), which may be as good a lubricant as another fluorocarbon polytetrafluoroethylene (PTFE).

To date, it is possible to synthesize fullerenes by different methods, such as combustion method [43] or treatment of graphite electrodes by electric arc discharge [44], carbon arc plasma [45] and laser pyrolysis of benzene [46]. Although now fullerene production is not completely established and fullerene price is comparatively high, there is a hope that in next few years this problem will be successfully solved.

The fullerenes are perhaps the purest and most stable form of carbon. The other two forms, diamond and graphite, are not environmentally stable. Under normal conditions, the diamond surface is instantly covered with hydrogen or hydroxide, which ties up the dangling surface bonds. Graphite works in the same way. Thus, diamond and graphite can never be truly pure under normal conditions. The fullerenes, on the other hand, need no other atom to satisfy their chemical bonding requirements on the surface. In this sense, the fullerenes are the only known stable form of pure carbon. The molecules C_{60} and C_{70} are considered very important due to their high stability and applicability. However, higher fullerenes also have significant applications.

Fullerenes can be used as possible admixtures to different lubricants and conventional oils in order to increase antifrictional properties, wear resistance and even anticorrosive properties. Another beneficial aspect of fullerene use as lubricant additives is their strong absorption ability. There are works [47, 48], which describe strong absorption force of fullerene and nanotubes. This leads to the idea that they can function as oxidation inhibitors.

Some publications [49, 50] already suggest modification of lubricants in order to improve their durability. In addition, there is coverage on producing new additives to lubricants [51, 52]. Recently new developments such as [21, 53] propose to use fullerenes

C_{60} as additives for solid and liquid lubricants, as well as protective solid film for coatings. Because of high elasticity, strength of crystals, weak intermolecular interactions, low surface energy and quasi-spherical shape of molecules, fullerenes C_{60} can be used for solving various tribological problems.

Ginzburg and others [53] present results obtained on steel-to-steel method operated in friction-sliding mode. The additives considerably improve wear resistant properties for all loads in hand. It is known that intermolecular lacing of polymer coatings increases their wear resistance, and introduction of C_{60} fullerenes in lubricant oils is expected to increase wear resistance of friction couples. There are some works [21-23, 54], where a film of fullerene C_{60} is as a solid lubricant and as an additive for liquid or solid lubricants. Although there is some data of fullerene effect on wear resistance of materials in load contact, still there is no consistency in these data as well as there is no consensus on mechanism of tribological behavior of fullerene-enriched lubricants. Therefore, Gruen and others [21] proposed the idea that fullerene additives in lubricants serve as precursors for developing diamond films. At the same time, Ginzburg and others [22] suggested that fullerene-enriched lubricants create protective films on the metal surface. Bhushan and others [23] offered opinion that fullerenes in friction process function as tiny rigid balls that are not squeezed out from load contact as the host lubricant.

Analysis of fullerene properties leads to the point that fullerene content lubricants have many advantages over already existing materials, and an investigation of possible applications of fullerene content lubricants can give new approach in wear resistance of materials.

CHAPTER 3

GOAL AND OBJECTIVES

The goal of this work is to study performance of fullerene containing lubricants under boundary lubrication conditions.

In order to achieve this goal the following objectives should be met:

- Development and implementation of computer-controlled wear friction testing methodology for getting reliable and objective data of friction moment, friction force, coefficient of friction, weight loss and wear rate of the contact materials during load and sliding operation.
- Modification of heavy-duty standard motor oil by fullerene additives and assessment of physical properties of the prepared lubricants.
- Evaluation of surface topography characteristics of tested friction couples at different stages of the experimental study.
- Investigation of influence of fullerene containing lubricants on friction and wear of the tested materials.
- Evaluation of maximum pressure in real contact areas of the friction couple.
- Assessment of the role of fullerene additives to liquid lubricant in improvement of wear resistance of the selected materials.

CHAPTER 4

NATURE OF CONTACT

Due to the difficulties with characterization of real surface topography and materials, mechanics heavily relies on the assumptions that surfaces and materials in hand are ideal. These assumptions are acceptable in most problems where surface irregularities can be neglected. However, tribology problems require detailed consideration of surfaces in contact.

In general, contact of two solids involves both elastic and plastic deformations within and below asperities. Elastic deformations are described by Hertz's equations and give the size of the contact region and its stress distribution. The stress level that causes plastic deformations helps understand the nature of the contact. Finally, the development of asperity contact model makes possible calculation of real contact area and real contact pressure to draw the valid picture of the processes in contact and additive effects.

4.1 Hertzian Contact

Because of elasticity that is an intrinsic property of most engineering materials, the contact region of cylindrical and flat surfaces is not limited by a line – it has some width. The width of and the stress distribution in this region depend on the applied load and mechanical properties of the materials in contact – Young's modulus E and the Poisson ratio ν [55]. Equations that give the size of the contact region and the stress distribution are available in many forms, but the most complete description was made by Hertz.

Based on the Hertz's theory, the evaluation of contact area for the case of steel roller and bronze shoe is made.

4.1.1 Cylinder on Flat

Without the applied normal force, the only contact between the cylindrical and flat surfaces is a direct line [56]. After applying the normal load, due to elastic deformations the line contact becomes a rectangular area. The width of this contact is $2a$, as shown in Figure 4.1, where a is half-contact width.

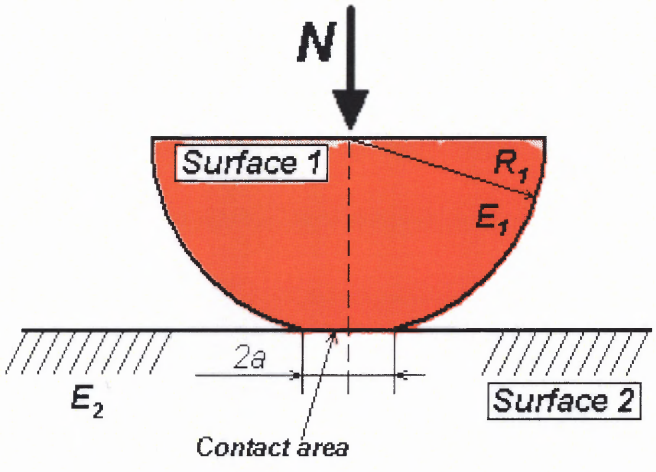

Figure 4.1 Contact area of a cylindrical surface and a plane.

The magnitude of a can be determined by Equation (4.1)

$$a = R_{eq}\left(\frac{8\bar{N}}{\pi}\right)^{1/2} \tag{4.1}$$

where R_{eq} is an equivalent contact radius and $\bar{N}$ is the dimensionless load which can be defined by the expression

$$\bar{N} = \frac{N}{LE_{eq}R_{eq}} \tag{4.2}$$

In this equation, N is the applied normal load, L – the effective length of the cylinder and E_{eq} is the equivalent modulus of elasticity. For a contact of two different materials, the equivalent modulus of elasticity E_{eq} can be determined by Equation (4.3)

$$\frac{2}{E_{eq}} = \frac{1-\nu_1^2}{E_1} + \frac{1-\nu_2^2}{E_2} \tag{4.3}$$

where ν_1 and ν_2 are Poisson's ratio and E_1 and E_2 are the modules of elasticity of the two materials in contact, respectively.

Equivalent radius R_{eq} of contact curvature is calculated as

$$\frac{1}{R_{eq}} = \frac{1}{R_1} + \frac{1}{R_2} \tag{4.4}$$

where R_1 and c of the convex contact. For a concave contact, see Figure 4.2, radius R_1 is negative, because the contact is inside this circle. The result is that the equivalent radius is derived according to Equation (4.5)

$$\frac{1}{R_{eq}} = \frac{1}{R_2} - \frac{1}{R_1} \tag{4.5}$$

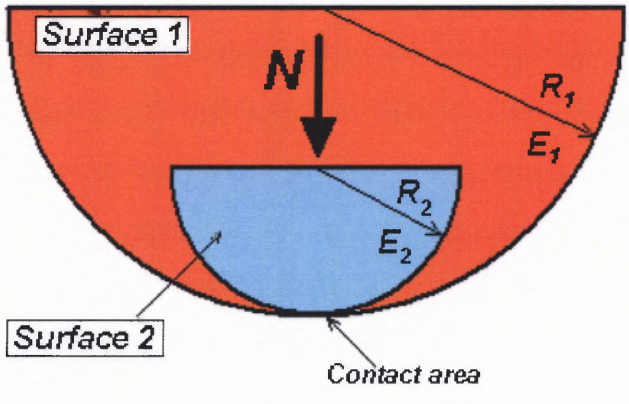

Figure 4.2 Concave contact, where R_1 – outside diameter and R_2 – inside diameter.

For cylinder-on-flat contact, the maximum elastic deformation of the roller in the direction normal to the contact area is

$$\varepsilon_{\max} = \frac{2\bar{W} R_{eq}}{\pi}\left[\ln\left(\frac{2\pi}{\bar{W}}\right) - 1\right] \tag{4.6}$$

According to Hertz's theory, there is a parabolic pressure distribution at the contact area, as shown in Figure 4.3.

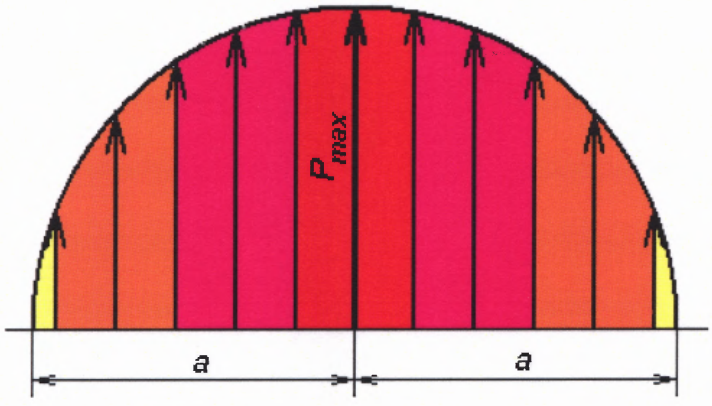

Figure 4.3 Pressure distribution in a rectangular contact area.

The maximum contact pressure is at the center of the contact area, and it equals

$$p_{\max} = E_{eq}\left(\frac{\bar{W}}{2\pi}\right)^{1/2} \tag{4.7}$$

According to Hertz's theory, contact width depends on the applied normal load, the effective length of the cylinder and the equivalent modulus of elasticity. Calculations of contact pressure show that it reaches the maximum value in the middle of the contact region, decreases to the sides and become zero on the borders of the contact region.

4.1.2 Calculations of Hertzian Contact Area and Pressure Distribution

In the case of initial contact of steel AISI 4340 roller and bronze SAE 40 shoe that are used in the experimental part, the material parameters and test characteristics are following

- R_r, radius of roller – $25.40 \cdot 10^{-3}\ m$;
- R_s, radius of shoe – $25.41 \cdot 10^{-3}\ m$;
- E_1, elastic modulus of roller (steel AISI 4340) – $200\ GPa$;
- E_2, elastic modulus of shoe (bronze SAE 40) – $93\ GPa$;
- ν_1, Poisson's ratio of roller (steel AISI 4340) – 0.32;
- ν_2, Poisson's ratio of shoe (bronze SAE 40) – 0.30;
- N, normal load – $640\ N$;
- L, length of cylindrical contact – $10^{-2}\ m$.

Substitution of above values for contact parameters into the expressions (4.1-4.7) gives the values of Hertzian contact characteristics

$$\frac{1}{R_{eq}} = \frac{1}{R_r} - \frac{1}{R_s} = 0.015 m^{-1} \tag{4.8}$$

$$R_{eq} = 64.5 m \tag{4.9}$$

The equivalent modulus of elasticity E_{eq}

$$\frac{2}{E_{eq}} = \frac{1-\nu_1^2}{E_1} + \frac{1-\nu_2^2}{E_2} = 1.41 \cdot 10^{-11} Pa^{-1} \tag{4.10}$$

$$E_{eq} = 1.42 \cdot 10^{11} Pa \tag{4.11}$$

The dimensionless load $\bar{N}$

$$\bar{N} = \frac{N}{LE_{eq}R_{eq}} = 7.0 \cdot 10^{-9} \tag{4.12}$$

The magnitude of a (half-contact width)

$$a = R_{eq}\left(\frac{8\bar{N}}{\pi}\right)^{1/2} = 8.6 \cdot 10^{-3} m \tag{4.13}$$

According to these calculations, the full width of contact is equal to $2a = 17.1 \cdot 10^{-3}$ m and the total contact area is

$$A_a = L \cdot 2a = 10^{-2} m \cdot 17.1 \cdot 10^{-3} m = 1.71 \cdot 10^{-4} m^2 \tag{4.14}$$

This value of total contact area demonstrates that the initial contact covers almost all area of bronze shoe and the maximum contact pressure is at the center of the contact area and equals

$$p_{\max} = E_{eq}\left(\frac{\bar{N}}{2\pi}\right)^{1/2} = 4.74 \cdot 10^{6} Pa \tag{4.15}$$

The above calculations show the Hertzian contact characteristics of the initial stage of roller-shoe contact. Although the described values of the maximum pressure and contact area are valid only for the initial period of testing, they have important meaning as a starting point of following consideration of elastic-plastic deformations and asperity contact.

4.2 Estimation of Elastic and Plastic Deformations

4.2.1 Classification of Friction Regimes

Destruction of the rubbing surfaces is generally manifested in the separation of particles of material of size varying from a few fractions of a micron to several microns. In rare cases, destruction is manifested by evaporation (dissociation) of the solid (abrasive wear). To a large extent, the way is prepared for the separation of these particles by the repeated load and temperature pulses on individual asperities. As a result of the constant accumulation of irreversible changes, inhomogeneity of structure and a condition of stress arise, that is, stress raisers are produced, or cracks may even appear, which form wear particles on linking up. Destruction is often preceded by a change in the properties of solids. Naturally, under these conditions, the changes, which precede destruction of the material and the nature of this destruction, are extremely variable, and this is reflected in the numerous classifications of different types of wear.

According to the classification based on the nature of the interaction between surfaces [57], the nature of the process involved in breaking a frictional bond and the group of processes occurring in the surface layers and microvolumes depend on numerous geometrical, mechanical, physical, and chemical factors. The geometrical factor, which characterizes the ratio of the depth of penetration or the magnitude of the compression to the radius of an individual asperity (h/R) is one of the most important of these. This characteristic provides a means of distinguishing elastic contact, plastic contact, and microcutting. The physico-mechanical factor, which characterizes the ratio of the tangential stress of a molecular bond to the yield point of the base material (τ/σ_T) is a second important factor. Two types of rupture of frictional bonds should thus be

distinguished: destruction of the bond along the separation surface between two bodies or along films coating these bodies (when the layers of base material are not affected), and rupture of the frictional bond in the bulk of the base material, in which case surface friction changes to subsurface friction. On the basis of the above, the following five types of frictional bond can be distinguished:

1. Elastic displacement of the material by the asperities of the counterface occurs when the actual load and the adhesion do not lead to stress in the contact zone exceeding the yield stress. In this case, damage to the material (wear) can occur only by frictional fatigue.

2. Plastic displacement or plugging of the material occurs when the contact stress reaches the yield stress but the material flows around the penetrating asperities of the counterface. In this case, wear will be the result of low cycle frictional fatigue.

3. Microcutting occurs when the contact stresses on deformation attain values large enough to produce damage (disturbance of the conditions for flow of deformed material around the penetrating asperities). In this case, damage occurs at the onset of interaction.

4. Adhesion disturbance of the frictional bond (along the same surface on which it arises) does not lead directly to damage, but provides a contribution to the contact stresses and strains, that is, it accompanies fatigue processes.

5. Cohesion rupture arises when the frictional bond is stronger than the underlying material and tearing occurs. In this case, as under (3), wear occurs at the onset of interaction.

Table 4.1 Classification of Frictional Bonds

Nature of deformation	***Elastic deformation***	***Plastic deformation***	***Microcutting***	***Adhesional disturbance***	***Cohesions rupture***
Number of cycles n*, leading to failure of base*	$n \to \infty$	$1 < n < \infty$	$n \to 1$	$n \to \infty$	$n \to 1$
Required conditions	$h/R < 0.01$ *(ferrous metals)*	$h/R > 0.01$	$h/R \geq \frac{1}{2}(1 - 2\tau/\sigma_T)$	$d\tau/dh > 0$	$d\tau/dh < 0$
	$h/R < 0.0001$ *(non-ferrous metals)*	$h/R > 0.0001$			

The fact that, depending on the type of damage to the frictional bond, see Table 4.1, the separation of material occurs as a result of different numbers of events, from very large ($10^6 - 10^8$ cycles) in elastic displacement to a single event in cutting of a material, is important for a proper understanding of the wear process.

4.2.2 Characteristics of Bodies in Contact

Classification of frictional bond helps to understand the nature of deformations of bodies in contact. In case of steel AISI 4340 roller and bronze SAE 40 shoe, the described parameters and evaluation of the nature of deformations are shown in Table 4.2.

Table 4.2 Characteristics of Bodies in Contact and the Nature of Deformations

Parameter	***Roller***, steel 4340	***Shoe***, bronze SAE 40
Depth of penetration, ***h***	***0.025 μm***	***0.25 μm***
Radius of individual asperity, ***R***	***25 μm***	***20 μm***
The geometrical factor, ***h/R***	***0.01***	***0.0125***
Tangential stress of a molecular bond, τ	***~ 80 MPa***	***~40 MPa***
Yield tensile strength, σ_T	***470 MPa***	***125 MPa***
Physico-mechanical factor, $\frac{1}{2}(1 - 2\tau/\sigma_T)$	***~ 0.3***	***~ 0.2***
Comparison of geometric and physicomechanical factors	$h/R < \frac{1}{2}(1 - 2\tau/\sigma_T)$	$h/R < \frac{1}{2}(1 - 2\tau/\sigma_T)$
Number of cycles, ***n***	***13, 700***	***13, 700***
Nature of deformation	***Elastic deformations; plastic deformations – negligible; microcutting – negligible***	***Elastic deformations; plastic deformations; microcutting - negligible***

Contact materials, their surface texture characteristics and test parameters are selected in such a way that only one material – bronze shoe – experiences both elastic and

plastic deformations. Meanwhile, steel roller has only elastic deformations and its plastic deformations can be neglected. This selection facilitates the development of real contact model for evaluation of real contact pressure and real contact area.

4.3 Estimation of Real Contact Characteristics

When two surfaces come into contact, the contact is not continuous, and only certain parts of the surface will carry the applied load. The sum of these discrete contact areas forms the real contact area. Accordingly, the real contact area defines those parts of the surfaces where there is strong interaction between the bodies. Consequently, if other parameters are equal, friction force and wear rate can be directly related to the real contact area.

Surface damage to solids during sliding (wear) is also closely bound up with the magnitude of the real contact area, since the most highly stressed elements of the layers near the surface are determined by its dimensions. Formation of the real contact area under load occurs as a result of the penetration or crushing of individual microasperities, and the greater the deformation, the larger the real contact area. Determination of the contact deformation is important for calculating the real contact area and for some other reasons. It has now been established that under the loads generally used in engineering, the deformations, which develop at a contact region, are mainly responsible for determining the change in the mutual positions of interacting components.

4.3.1 Types of Contact Areas

The discrete nature of the contact is a characteristic feature of all contacts between solids without exception and is related to their roughness. The lack of uniformity in the distribution of the contact points is not quite so characteristic, although it always occurs with sufficiently extended contacts and depends on the existence of waves on the surfaces of solids, see Figures 4.4 and 4.5. Waviness, as with surface roughness, arises during the manufacture of components (manufacturing waviness) and during use (service waviness). The ratio of the frequency characteristic to the amplitude can be used as a criterion for distinguishing between waviness and surface roughness. The wave height is comparable with the asperity height, but the wave spacing is much larger than average distance between asperities. For waves, the ratio of wave spacing to wave height is much larger than for asperities. This criterion is used as the basis for a classification of the irregularity of real surfaces [58].

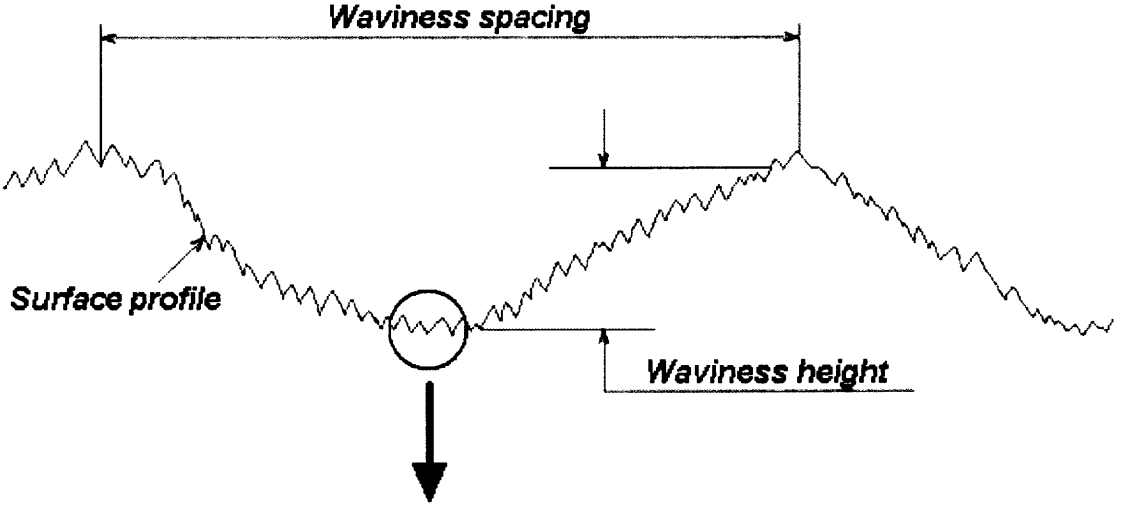

Figure 4.4 Surface waviness parameters.

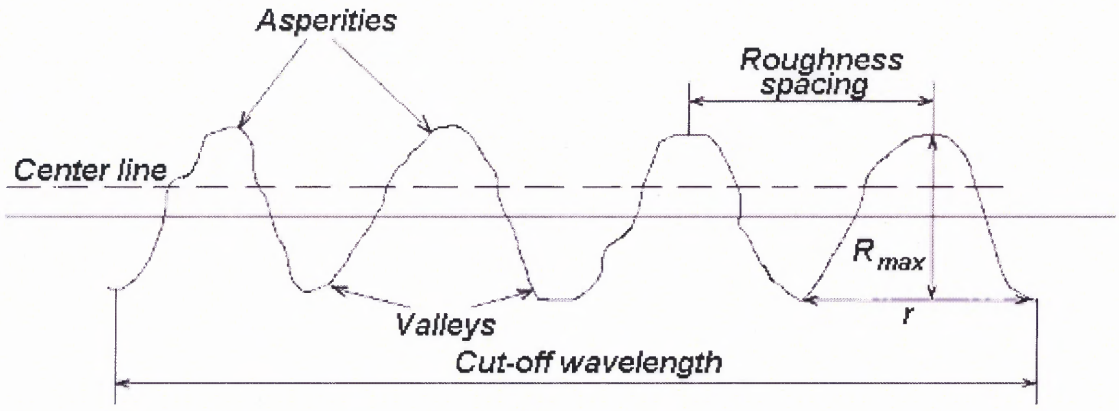

Figure 4.5 Surface roughness parameters.

When components make contact, because of the waviness of their surfaces, the real contact points will arise mainly at the wave tips. Each such region will be bounded by a contour containing the real contact points, an elementary contour area ΔA_c, see Figure 4.6. These contours are separated by a distance equal to the wavelength. The contour contact area A_c is equal to the sum of the elementary areas ΔA_c [3].

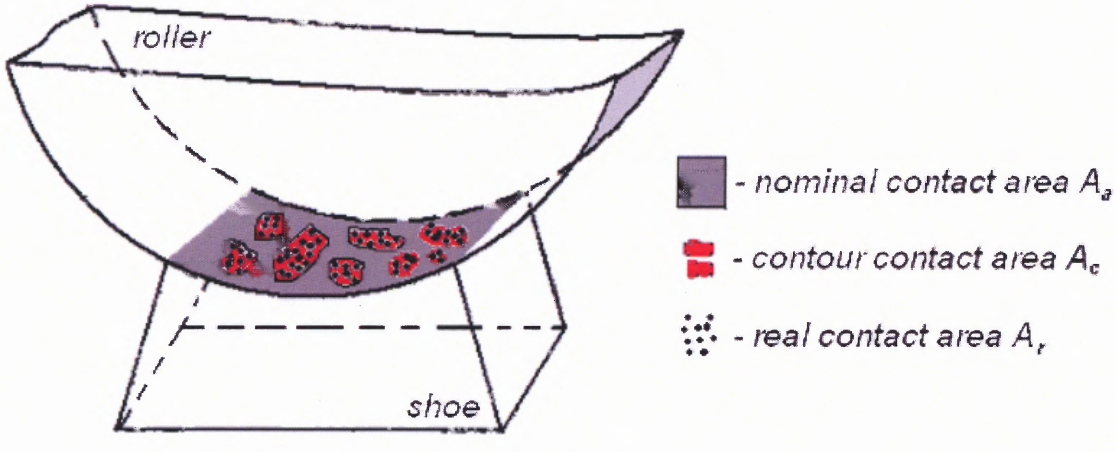

Figure 4.6 Diagram of three contact areas.

Introduction of the contour area concept is necessary for the following reasons. The surface relief is assessed from a profilogram, which is obtained from a very restricted part of the surface. The base line (for the most widely occurring surface roughness classes) varies over the range 0.25 – 0.8 *mm*, which is less, or in the limiting case of the same order as the wavelength. Accordingly, a profilogram does not reflect the true relief of the whole surface, but gives an indication of a small part of it.

The presence of waves is associated with localization of regions where microcontacts can exist, which leads to an increase in their density, so that the commonly used theory of the absence of any mutual effect between microcontacts must be erroneous. The contact area arises as a result of deformational processes concentrated in the surface layers of contacting bodies, and thus depends essentially on the load and the mechanical properties of the material. The contour area is a fictitious area and is introduced as a stepping-stone in the transition from the nominal area A_a to the real contact area A_r.

The real contact area A_r is the sum of the elementary real contact area ΔA_r arising from deformation of individual asperities. This area determines the region of strong interaction between two rough bodies determined by intermolecular interaction. Calculation of the real contact area is, thus, one of the most important parts of friction and wear evaluations.

Nominal contact area A_a is the area over which bodies would make contact if they had ideally smooth surfaces. In the case of bodies with a surface of uneven contour, this is the area, over which two smooth bodies of same contour would make contact when a load is applied. This area arises from deformation of the bodies (mainly elastic), and,

thus, as with the two areas described above, is determined by contact geometry, the mechanical properties of the materials and the applied load. In calculating the nominal contact area, it is reasonable to use the appropriate solutions of contact problems in theory of elasticity. The quantity A_a as well A_c is a fictitious quantity, and it is convenient to use dimensionless areas

$$\eta_{r,c} = \frac{A_r}{A_c} \qquad \eta_{c,a} = \frac{A_c}{A_a} \qquad \eta_{r,a} = \frac{A_r}{A_a} \tag{4.16}$$

Evidently,

$$\eta_{r,c} \cdot \eta_{c,a} = \eta_{r,a} \tag{4.17}$$

Three types of pressure can be distinguished – the actual pressure p_r, the contour pressure p_c and the nominal pressure p_a that equal

$$p_r = \frac{N}{A_r} \qquad p_c = \frac{N}{A_c} \qquad p_a = \frac{N}{A_a} \tag{4.18}$$

4.3.2 Surface Roughness Models

The wide volume of experimental material, which has accumulated on the real contact area, enables the most characteristic features of the process of forming it to be classified as follows:

1. the contact of rough surfaces has a discrete character;
2. elementary contacts (real contact points) arise as a result of both elastic and plastic deformation;
3. the real contact area and the load are related by Equation (4.19)

$$A_r = const \cdot N^z \tag{4.19}$$

where $z = 1$ in plastic contact and is very close to 1 ($z \cong 0.8\text{-}0.9$) in elastic contact;

4. with increase in load the increase in real contact area occurs mainly because of the appearance of new contact points, the mean size of the contact points remaining almost constant.

According to point (1) above, a surface roughness model can be represented in the form of a set of asperities, which must be described by a number of parameters characterizing their geometrical profile. Investigation of surface relief by various methods gives some ideas of the shape and dimensions of these asperities. A very good imagination would be required to perceive the true geometrical profile in actual contours of asperities. However, in the interests of simplicity and clarity the model of an individual asperity should be selected from a series of the simplest geometrical profiles. In fact, the contact problems of elasticity and plasticity theory, which are the basis of calculations of the real contact area, have comparatively simple solutions only on bodies of regular geometrical profile. At this point, it is simply noted that of the numerous forms of asperities, spherical, cylindrical and elliptical asperities are the ones, which most completely fulfill all the required conditions. For setting up a universal model suitable for calculating the real contact area and for friction and wear calculations in general, the spherical model is to be preferred because of axial symmetry. In addition, a spherical model reflects the isotropic character of friction, whereas a flat die and a wedge models describe anisotropic effects.

4.3.3 Contact Area of Two Real Surfaces

In deriving the theoretical relations the following assumptions are made:

I. The surface roughness model consists of spherical segments or radius r on a rigid base. The approach of two bodies is thus determined only by the deformation of the smooth body and of rough layer.

II. It is assumed that close contacts do not affect each other and the existence of an unambiguous connection between the load and deformation at the contact point is assumed.

The first assumption depends on the following considerations. Formation of the real contact area is closely bound up with irregularity of deformations. If a system of concentrated forces with a spacing s is applied to the surface of the body, according to the St. Venant principle [59], the stress distribution at a distance from the surface commensurate with the value of s is the same as if a uniform load distribution acted on the surface. Consequently, the dimension of a layer with non-uniform strain distribution is of the same order as s. It can be assumed that a concentrated force acts at each contact point that the dimensions of this layer can then be assessed at around 100 μm, which is more than an order of magnitude higher than the height of the asperities.

However, the stresses in this layer are significantly less than those, which arise at the asperities themselves – about 1/100 – 1/1,000 of these stresses. Accordingly, movement of the underlying layer of material because of deformation is less than the contact movements by a factor of 10-102, so that this movement can be ignored in the calculations.

The contact between a smooth body S and a rough body R will be considered. In the unloaded state body R makes contact with the surface *00* of body S at its highest asperity. Figure 4.7-a represents a section through the contacting bodies in a plane perpendicular to the smooth surface of body S. On applying a load N the bodies are drawn together by an amount H_1-H_2, see Figure 4.7-c.

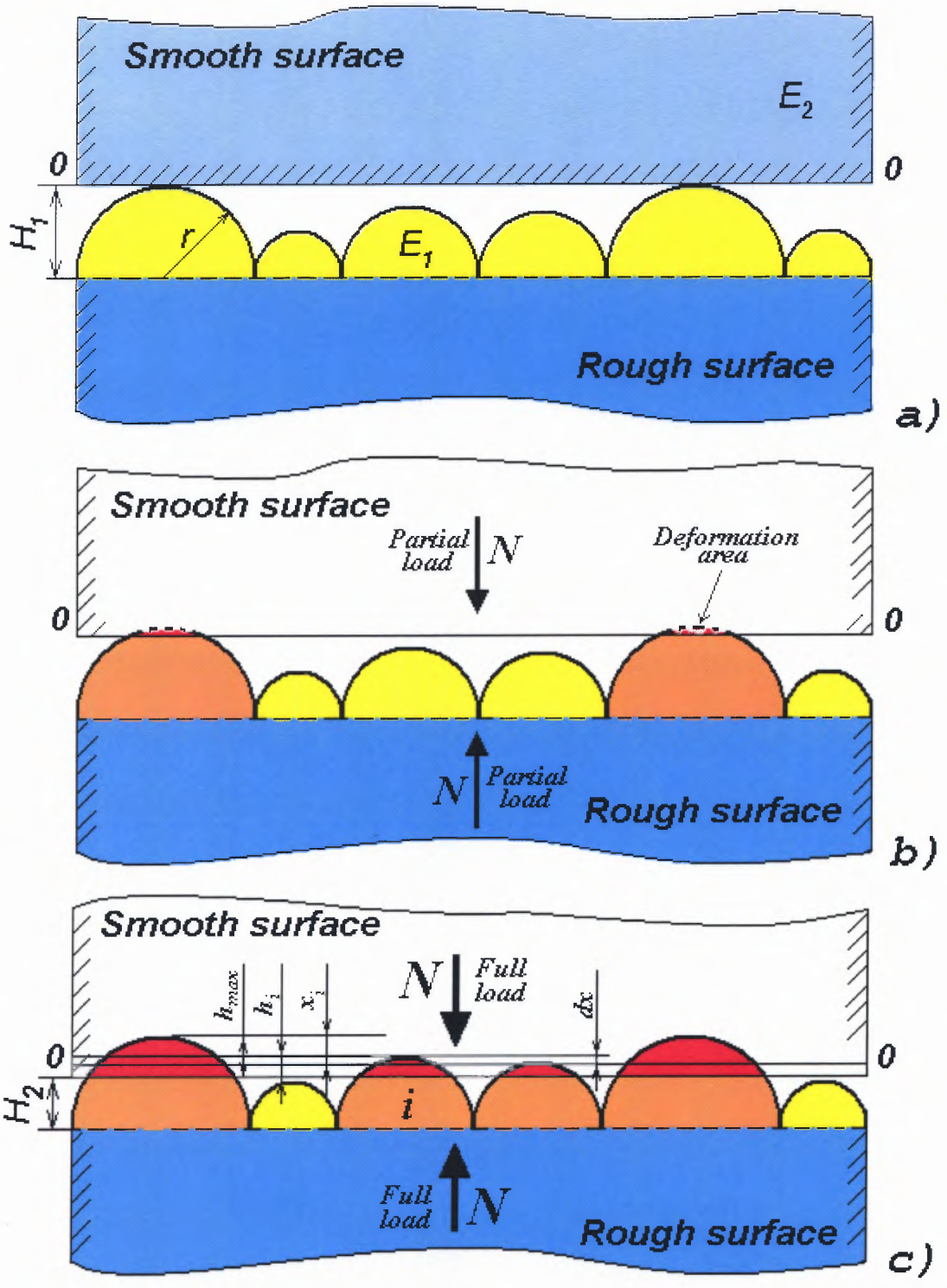

Figure 4.7 The contact between ideally smooth and rough surfaces: a) initial position, b) intermediate position with partial load and c) position after applying a compressive force. On these pictures: H_1 and H_2 – distances between bodies in contact in unloaded and loaded cases, respectively, h_{max} – the relative contact approach of the highest asperity, h_i – the relative contact approach of *i-th* asperity, dx – a elementary layer of thickness, x_i – a distance from the tip of the largest asperity to a elementary layer dx.

The boundary between the rigid base of body R and a certain point on the surface of body S that is sufficiently far from the contact region, is taken as a basis for calculating the magnitude of the "approach", that is the relative approach of the two surfaces under load after the initial contact has been made.

The dotted line in Figure 4.7-c shows the spherical segments in the unloaded state. All the asperities, the tips of which lie above the line *00*, enter into the contact, and the given approach of the surfaces will be attained when each i-th asperity of the asperities entering into the contact approaches body S by the amount h_i. The magnitude of the approach is taken to be the displacement of the i-th asperity and body S as calculated at the moment of contact. The approach of two bodies is thus numerically equal to the approach, or hypothetical interpenetration, of the largest asperity and the body S.

As a distance x from the tip of the largest asperity there is a layer of thickness dx. All the asperities with tips in this layer are approached by the surface of body S by the same amount, equal to $\varepsilon - x$, where ε is the relative approach of the bodies, which is equal to

$$\varepsilon = h_{max}/R_{max} \tag{4.20}$$

where x is a dimensionless coordinate which is equal to

$$x = X/R_{max} \tag{4.21}$$

and where X is the distance from the tip of the largest asperity to the layer.

The positions of the spherical segments of the model are given by

$$\varphi(x) = \frac{n_r}{n_c} = Cx^{\beta} \tag{4.22}$$

where n_r is the number of tips lying above the level x, n_c is the total number of spherical segments, and C and β are constant. Assuming that the function $\varphi(x)$, see Equation

(4.22), is continuous, the number of asperities with the tips in the layer between levels x and $x+dx$ can be calculated from

$$dn_r = n_c \varphi'(x) dx \tag{4.23}$$

Assuming that for given conditions of interaction there is an unambiguous connection between the load received by the asperity and the magnitude of its approach, $N = N(\varepsilon\text{-}x)$, it is possible to find the load for all asperities having tips with coordinates in layer dx

$$dN = n_c N(\varepsilon - x)\varphi'(x) dx \tag{4.24}$$

Summing over all the layers containing the tips of the contacting spheres, and writing the equilibrium conditions, an equation is arrived at which connects the approach of the rough and smooth bodies with the applied load

$$N = n_c \int_0^{\varepsilon} N(\varepsilon - x)\varphi'(x) dx \tag{4.25}$$

The function $N(\varepsilon\text{-}x)$ can be expressed in terms of the mean normal pressure on the contact $p_r(\varepsilon - x)$, and the projection of the area of an individual contact on a plane parallel to the smooth surface $A_r^o = A_s^o$, where A_r^o is cross-sectional area of an asperity at a distance $\varepsilon - x$ from its tip. The factor ε depends on the type of contact (elastic or plastic).

For spherical model consideration of the geometry shows that the area A_s^o can be calculated from

$$A_s^o \approx 2\pi r R_{\max}(\varepsilon - x) \tag{4.26}$$

In deriving this equation the square of the sphere penetration is ignored by comparison with the derivative $2r \cdot R_{max}(\varepsilon\text{-}x)$, since in these calculations it is always true that $r >> R_{max}\,(\varepsilon\text{-}x)$.

Allowing for the above, Equation (4.25) can be written in the form

$$N = 2\pi r R_{\max} n_c \alpha \int_0^{\varepsilon} (\varepsilon - x) p_r(\varepsilon - x) \varphi'(x) dx \tag{4.27}$$

Equations (4.25) and (4.27) are written in the most general form. The factor α and the functions $n(\varepsilon - x)$ and $p_r(\varepsilon - x)$ in these equations depend on the type of deformation arising on contact of the bodies, so that further consideration of the problem is impossible unless this has been established. Between two types of real asperity contact, elastic and plastic, elastic contact, which is generally found in sliding applications, has vast practical importance.

Elastic contact. From a solution of the Hertz problem for the contact between a sphere and a flat surface it follows that the function $N(\varepsilon - x)$ has the form

$$N(\varepsilon - x) = \frac{4}{3} \frac{r^{1/2} R_{\max}^{3/2}}{\Theta} (\varepsilon - x)^{3/2} \tag{4.28}$$

where $\Theta = (1 - \nu_1^2)/E_1 + (1 - \nu_2^2)/E_2$ is generalized Kirchhoff elastic constant, and E_i and ν_i are the elastic modulus and Poisson's ratio of the bodies, respectively.

Allowing for the fact that

$$\varphi'(x) = C\beta \cdot x^{\beta - 1} \tag{4.29}$$

and inserting Equations (4.28) and (4.29) into Equation (4.25), it is found that

$$N = \frac{4}{3} C n_c \beta \frac{r^{1/2} R_{\max}^{3/2}}{\Theta} \varepsilon^{\beta + 3/2} \int_0^1 (1 - \gamma)^{3/2} \gamma^{\beta - 1} d\gamma \tag{4.30}$$

where $\gamma = x/\varepsilon$.

The integral in Equation (4.30) consists of a beta function *B (5/2; β)*, which can be expressed as a gamma-function

$$B(5/2;\beta) = \frac{\Gamma(5/2)\Gamma(\beta)}{\Gamma(5/2+\beta)} \tag{4.31}$$

Using the expression for β and C show details

$$\left.\begin{aligned} \beta &= \lambda - 1 \\ Cn_c &= \frac{A_c \lambda b}{2\pi r R_{\max}} \end{aligned}\right\} \tag{4.32}$$

Allowing for Equation (4.32) and making some transformations, the equation obtained is

$$\varepsilon = \left\{ \frac{2\sqrt{\pi}\, p_c \Theta}{\kappa_\lambda} \left(\frac{r}{R_{\max} b^2} \right)^{1/2} \right\}^{\frac{2}{2\lambda+1}} \tag{4.33}$$

where b is bearing area curve parameter and $\kappa_\lambda = \Gamma(\lambda+1)/\Gamma(\lambda+3/2)$ is a numerical factor which depends on parameter for the degree of approximation of the bearing curve area λ and contour pressure p_c.

If the elastic modulus of one of the bodies is significantly larger than the other, then the first body can be considered absolutely rigid and in this case the approach will be determined only by the elastic properties of the second body.

The quantities in Equation (4.33) can be classified in the following terms:

External conditions. An example is the contour pressure pc. The approach is proportional to the contour pressure in the index $2/(2\lambda+1)$, which is less than unity.

Elastic properties of material. This is represented by the symbol Θ. Since Poisson's ratio changes insignificantly for a wide range of materials, the stiffness of the contact depends mainly on the elastic modulus. The approach is inversely proportional to the elastic modulus in the index $2/(2\lambda+1)$.

Surface microgeometry. The effect of surface microgeometry appears in two ways. Firstly, the parameter ν takes part in forming the index for p_c and Θ. Secondly, in passing from relative values of the approach to an absolute value, all the surface microgeometry criteria can be united in the complex expression $r^{1/2}R_{\max}^{\lambda}/\kappa_{\lambda}b$

It is generally known that the higher the surface roughness class of mating surfaces, it means the smaller the value of R_{max}, the more rigid the joint. In this relation, the complex expression $r^{1/2}R_{\max}\kappa/\lambda b$ only confirms a widely known rule. What is new in principle is that surface treatment methods, on which the remaining characteristics in the equation depend, are very important as well as the surface roughness class. For example, the radius of curvature of the asperity tips for the same class of surface roughness can vary within two orders of magnitude, depending on the type of surface treatment, which leads to an approximately tenfold change in the penetration.

The following considerations are used in calculating the real contact area. The radius of a circular contact area is given by

$$a_i = \left\{\frac{3}{4}N_i r\Theta\right\}^{1/3} \tag{4.34}$$

The area of a single contact formed by an asperity with its tip at the level x is then given by

$$A_r^o = \pi\left\{\frac{3}{4}N_i r\Theta\right\}^{2/3} = \pi\left\{\frac{3}{4}N(\varepsilon - x)r\Theta\right\}^{2/3} \tag{4.35}$$

All these asperities form an area

$$dA_r = \pi n_c\left\{\frac{3}{4}N(\varepsilon - x)r\Theta\right\}^{2/3}\varphi'(x)dx \tag{4.36}$$

Substituting for $N(\varepsilon\text{-}x)$ and $\varphi'(x)$ as given by Equations (4.28) and (4.29) and integrating, the obtained equation is

$$\eta_{r,c} = \frac{A_r}{A_c} = \frac{1}{2}b\varepsilon^{\nu} \tag{4.37}$$

If waviness of the surface in contact is negligible, contour contact area A_c is considered equal to nominal contact area A_a that leads to $\eta_{a,c} \cong \eta_{r,c}$.

The multiplier ½ in Equation (4.37) is α. Allowing for (4.33) Equation (4.37) takes the form

$$\eta_{r,c} = \left\{\frac{\pi^{1/2}}{2^{1/2\lambda}\kappa_\lambda}p_c\left(\frac{rb^{1/\lambda}}{R_{\max}}\right)^{1/2}\Theta\right\}^{\frac{2\lambda}{2\lambda+1}} \tag{4.38}$$

It can be seen from Equation (4.38) that the real contact area is proportional to the contour pressure and inversely proportional to the elastic modulus when the index is close to the unity.

4.3.4 Calculations of Real Contact Area and Pressure

Below are shown surface roughness profiles of bodies in contact – roller of steel AISI 4340, see Figure 4.8-a, and shoe of bronze SAE 40, see Figure 4.8-b. The major surface texture parameters are shown in Figure 4.9.

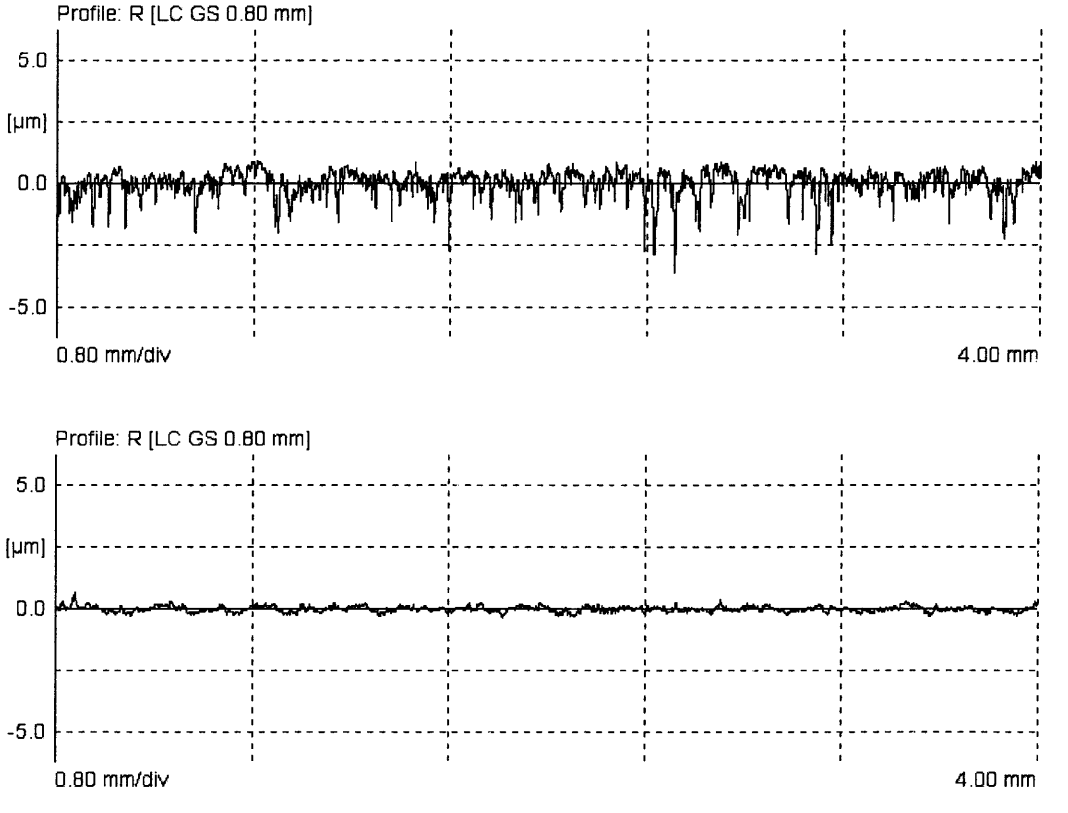

Figure 4.8 Roughness profiles of the bodies in contact: a) roller and b) shoe.

Parameter field for steel roller:		
Ra	0.39	µm
Rz	3.54	µm
Rq	0.54	µm
Rp	0.87	µm
R3z	2.60	µm
R Sk	-1.68	
R Ku	7.42	
Rv	2.67	µm
Rv1	2.01	µm
Rv2	2.75	µm
Rv3	2.72	µm
Rv4	3.61	µm
Rv5	2.27	µm
Rv sigma	0.55	µm
Rdq	0.182	
Rk	0.98	µm
MR1	4.99	%
MR2	81.80	%

a)

Parameter field for bronze shoe:		
Ra	0.11	µm
Rz	0.88	µm
Rq	0.14	µm
Rp	0.41	µm
R3z	0.57	µm
R Sk	-0.50	
R Ku	3.61	
Rv	0.47	µm
Rv1	0.58	µm
Rv2	0.40	µm
Rv3	0.51	µm
Rv4	0.36	µm
Rv5	0.49	µm
Rv sigma	0.08	µm
Rdq	0.035	
Rk	0.39	µm
MR1	6.76	%
MR2	87.34	%

b)

Figure 4.9 Surface texture parameters: a) roller and b) shoe.

For the calculations of real contact area and pressure, waviness of the surface in contact is negligible and contour contact area A_c is considered equal to nominal contact area A_a. The values of the following parameters are used:

- R_{max}, maximum height of profile asperities – *3.1 μm*;
- r, radius of an individual asperity – *30.5 μm*;
- λ, parameter for degree of approximation of the area curve – *2*;
- b, bearing area curve parameter – *2*;
- E_1, elastic modulus of roller (steel AISI 4340) – *200 GPa*;
- E_2, elastic modulus of shoe (bronze SAE 40) – *93 GPa*;
- ν_1, Poisson's ratio of roller (steel AISI 4340) – *0.32*;
- ν_2, Poisson's ratio of shoe (bronze SAE 40) – *0.30*;
- N, normal load – *640 N*;
- A_c, contour area – *1.7 10^{-4} m^2*.

Substituting the values of these parameters into the expressions for following values, we get the value of the generalized Kirchhoff elastic constant Θ

$$\Theta = (1-\mu_1^2)/E_1 + (1-\mu_2^2)/E_2 = 1.41 \cdot 10^{-11} Pa \tag{4.39}$$

A numerical factor

$$\kappa_\lambda = \Gamma(\lambda+1)/\Gamma(\lambda+3/2) = 2/3.32 = 0.60 \tag{4.40}$$

The contour pressure p_c

$$p_c = \frac{N}{A_c} = 3.76 \cdot 10^6 Pa \tag{4.41}$$

The relative approach of the bodies

$$\varepsilon = \left\{ \frac{2\sqrt{\pi} p_c \Theta}{\kappa_\lambda} \left(\frac{r}{R_{\max} b^2} \right)^{1/2} \right\}^{\frac{2}{2\lambda+1}} = 0.047 \tag{4.42}$$

The relationship between A_r and A_c

$$\eta_{r,c} = \left\{ \frac{\pi^{1/2}}{2^{1/2\lambda} \kappa_\lambda} p_c \left(\frac{r b^{1/\lambda}}{R_{\max}} \right)^{1/2} \Theta \right\}^{\frac{2\lambda}{2\lambda+1}} = 0.0023 \tag{4.43}$$

The real contact area

$$A_r = \eta_{r,c} \cdot A_c = 0.39 \cdot 10^{-6} m^2 \tag{4.44}$$

The real contact pressure

$$p_r = \frac{N}{A_r} = 1.63 \cdot 10^9 Pa \tag{4.45}$$

The performed calculations show that the real contact area is only a small fraction of contour area and, therefore, the real contact pressure p_r, see Equation (4.45), is much higher than contour p_c, see Equation (4.41).

CHAPTER 5

METHODOLOGY

Wear friction testing methodology and equipment, which are developed, manufactured and implemented in Surface Engineering Laboratory at NJIT, consists of computer controlled wear friction testing machine (WFTM) and various research techniques of both quantitative and qualitative analysis of friction-wear experiment output. These methods include evaluation of friction moment, friction force and friction coefficient, calculation of wear rate and weight loss of a tested sample, examination of contact surfaces before and after experiment and processing and representation of obtained data.

5.1 Computer Controlled Wear Friction Testing Machine

5.1.1 Design of the Machine

The overall design of wear-friction testing machine [60, 61] is shown in Figure 5.1. It consists of electric motor (1) with suspended stator, reducer (2), cycle counter (3), driving shaft (4), rubbing couple – roller (5) and shoe (6), loading mechanism (7), strain gages beam (8), strain gages (9), strain indicator (10), computer (11) and digital linear indicator (12). For collecting and processing of experiment data, the LabView application was developed and implemented – for friction measurements, and Visual C++ program was built and set up – for wear measurement part. The rubbing couple – *AISI 4340* steel roller and bronze *SAE 40* shoe – was selected in such a way that only shoe manufactured of a soft material experiences noticeable wear and weight loss. Wear of roller is minimal and

is neglected in this research. The final output of friction-wear test is friction coefficient of the rubbing couple, wear rate and weight loss of the shoe.

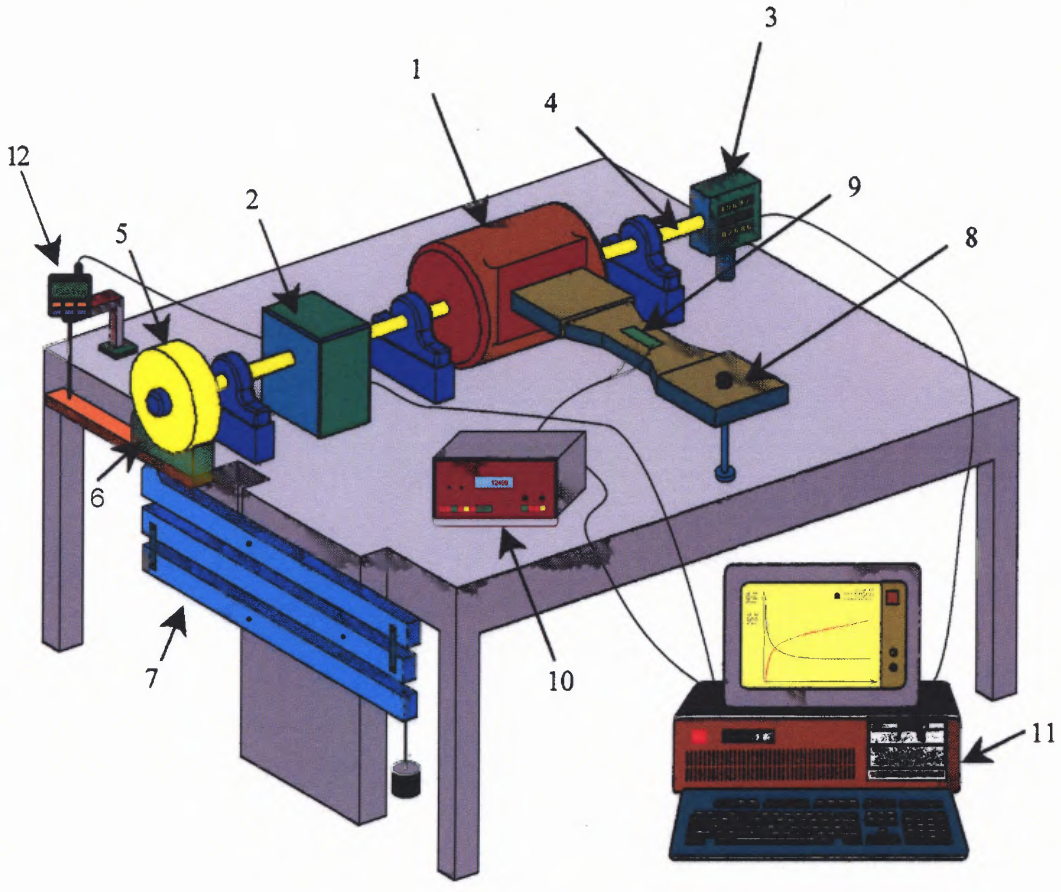

Figure 5.1 Computer controlled wear friction testing machine.

This machine design makes possible to calculate motor's power changes, which are triggered by changes in friction force between shoe and roller. The distinctive point of the proposed computer-controlled wear friction testing machine is the use of suspended electric motor placed between two bearings. This design allows to measure motor's power losses by attaching strain gages beam by one end to the stator of electric motor and the other end on a stopper fixed to the unmovable table. If the stator of the motor under

the effect of established magnetic field between the rotor and the stator tends to rotate around the rotor attached to the driving shaft (4), the beam (8) experiences bending stresses. These stresses depend on motor's consumed power and can be measured by strain gages placed in the middle of the beam. Strain gages resistance changes due to beam elongation registered by strain gage amplifier go to the computer. Computer receives and saves the data that are later used for calculations of friction characteristics. Detailed discussion of friction test characteristics is shown in Section 5.2.

The other task of WFTM is online recording and calculation of wear rate and weight loss of a tested sample. For these purposes, wear testing machine is furnished with digital linear gage (12) (DLG), which is placed between movable shoe holder and the table and can provide online recording of distance change between the center of the roller and the bed of the shoe holder. This distance change is used in calculation of wear rate and weight loss of a shoe, see Section 5.3.

5.1.2 Tribotest Flow Chart

Development of computer controlled wear friction test solution consists of implementation of sub solutions for different stages of the whole process. The principal stages of whole process, which have to be accomplished during a test, are listed below:

> *start; power is on for the testing system; start AC motor; warm up period for AC motor; 10 second warning for warm-up period end; start DA system; start solenoid of lubrication supply device and selection of lubrication cycle; start load mechanism and load mode selection; 10 second wait and start load test data; test duration time; pre warn duration of test finishing; unload test load; wait 10 second for full unload; turn off lubrication; complete test cycle; reset.*

Operational steps of computer controlled wear friction testing machine are shown on the flow chart in Figure 5.2.

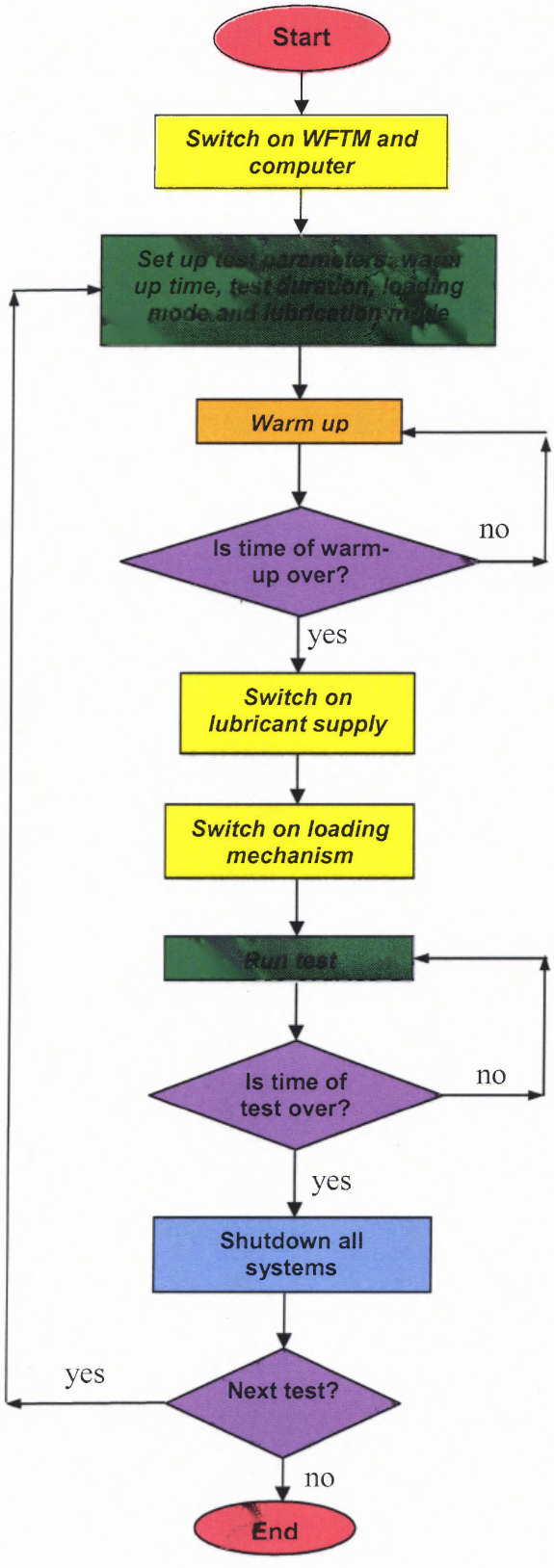

Figure 5.2 Flow chart of the wear-friction testing process.

5.1.3 Description of the System

The described wear-friction testing machine employs parallel measurement of wear rate and friction coefficient. For measurements of friction and wear parameters, two independent subsystems of data collecting are used, see Figure 5.3. Detailed description of each element on this diagram is given in Subsections 5.1.3-5.1.9.

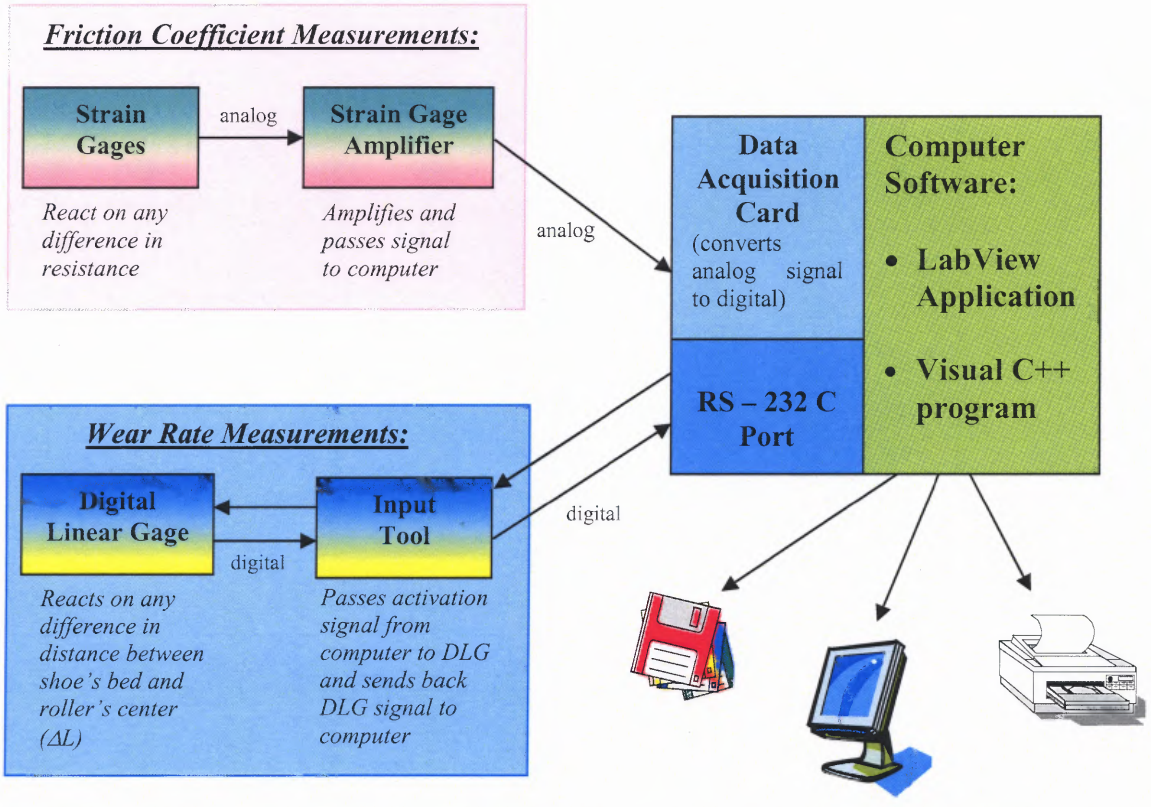

Figure 5.3 Block system for measuring and collecting of friction and wear data.

5.1.4 Strain Gages and Strain Gage Amplifier

Strain gages placed on the beam for monitoring of bending stresses are sensitive to any stresses developed in the beam, which are the key point in measuring changes in motor's moment. Strain gages are a product of Omega, model SG-7/350-DY11. Encapsulated

with ribbon leads these strain gages are easily glued to the beam. Nominal resistance is 350 *Ohm*, dimensions of the grid are 7.0 *mm* on 3.8 *mm* and dimensions of the carrier are 12.0 *mm* on 11.0 *mm*. Maximum permitted bridge energizing voltage is 15 *V*.

The role of strain gage amplifier is to monitor resistance changes in strain gages, strengthen this signal and transmit it to the computer. The Model 3800 Wide-Range Strain indicator is a highly versatile, precision instrument specifically designed for use with strain gages and strain-gage-based transducers. Gage factor varies from 0.0500 to 50.00. The balance controls of the Model 3800 provide a total balance range of greater than +100 % of full-scale reading at a gage factor of 2.000. The balance range is further subdivided into 32 overlapping ranges to obtain precise settability and resolution. All balance voltages are electronically injected into the input amplifier. This method eliminates potentiometric bridge loading errors and does not compromise the measurement range of the instrument. The excitation voltage of the Model 3800 is precisely settable by a front-panel thumbwheel switch over a range of 1 to 15 *V* in one-volt increments. The amplifier gain is automatically adjusted in inverse ratio to the excitation setting so that gage factor is independent of excitation. Ultra-stable internal half-bridge, 120/1000-*Ohm* and 350-*Ohm* dummy gages are provided. Shunt calibration is achieved by connection of shunt calibration resistors across dummy gages. Connections to the Model 3800 may be made via the front-panel binding posts or the rear-panel transducer connector.

Special attention in setting and tuning of strain gages is paid to calibration of strain gages stresses and conversion of the obtained signal to stresses developed in the

beam. Calibration of strain gages was done by gradual applying of known moment values to the beam and taking respective data from strain gage amplifier.

5.1.5 Data Acquisition Card

This data acquisition card (DAC) serves as converter and stabilizator of the signal received from strain gage amplifier. The PCI-DAS1001 data acquisition card is multifunction analog and digital I/O board designed to operate in computers with PCI bus accessory slots. The board provides 16 single-ended/8 differential analog inputs with sample rates as high as 150 *KHz*. The board is fully plug-and-play, with no switches or jumpers to set, and fully auto- and self-calibrating with no potentiometers to adjust. All calibration is performed via software and on-board trim D/A converters. This board is fully supported by the Universal Library software driver library as well as a wide variety of application software packages.

5.1.6 Loading Mechanism

The role of loading mechanism is to develop various loading-unloading modes during a test – cyclic mode, stable load and others simulating different real machinery processes. Loading mechanism is motor-controlled system, which can be operated in manual and automatic modes. It consists of shoe holder, sliding bearing, lever mechanism, DC motor and cam. The loading cycle of cam can be preset on computer. Design of loading mechanism is based on a cam configuration and reinforced by effective leverage of 72. Setting different programming modes for the cam gives different simulations of real friction processes.

5.1.7 Lubricant Supply Device

Lubrication mode plays important role during a test and requires precious delivery in contact. For this purpose, lubrication supply device was developed and installed. It includes lubricant pot, control valve, electric supply, connecting pipe and pipette. Operational regime of valve is to be set up before test and can be variable or stable.

5.1.8 LabView Application

For receiving and processing signal from strain gages, which is strengthened by strain gage amplifier and converted by DAC, LabView Virtual Instruments application has been developed and installed. This program allows multi-level processing of the obtained signal, such as signal synchronization with timer, conversion signal into a required format, displaying obtained data on the computer screen and saving them in a file. Figure 5.4 shows major steps of data processing. The first step (1) is to define a number of cycles in test. Operational frequency of data collecting can be set up as high as 50 *Hz*, but because of system synchronization, data collecting of this LabView application is lined up with C++ program and frequency is set up on 1 *Hz*. Empty Path (2) is responsible for tracking any errors in the cycle. Timer (3) sends signal to (4) every 1000 milliseconds, and this signal after being divided by 1000 is displaying test time in second on the screen (7). Data acquisition board number, channel number and data range are identified in (5). After error filter (6), current signal is displayed on the screen (7). Next stage is data formatting, compiling and recording to file. For these purposes, time and strain gage signal are being converted to decimal number (8), divided by tabulation for easing future processing and accumulated in one data line (9). Saving to file (10) is final step of the

cycle and after its completing cycle start over. This application uses so called "for" loop – program works for number of cycles determined in the beginning.

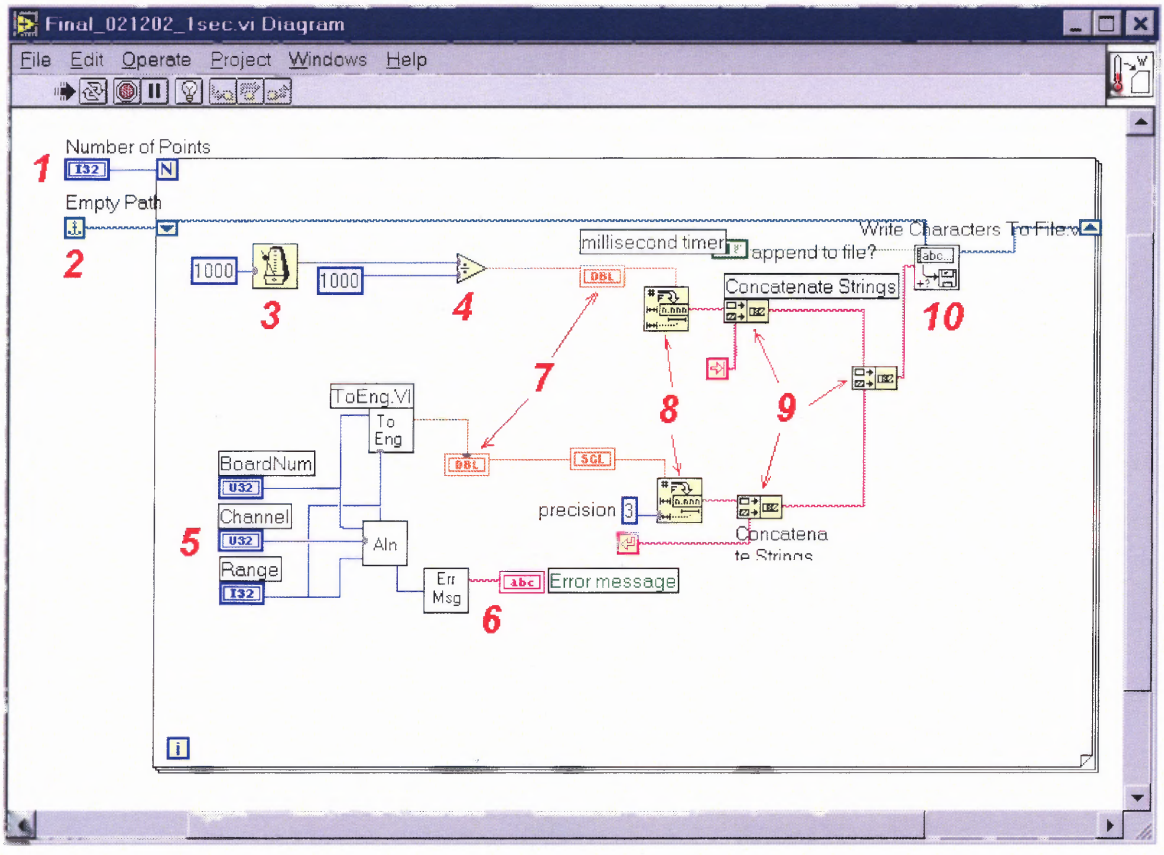

Figure 5.4 Scheme of LabView Virtual Instruments diagram.

Figure 5.5 shows computer screen in a pilot test. Information on screen indicates technical data such as DA board number, channel, signal range and number of points in test. In the left bottom corner second timer is located. Time data as well as friction coefficient readings are being sent to file with initially specified frequency. On the big graph, dynamics of friction coefficient in boundary lubrication regime is shown. Horizontal axis of this graph is time and vertical axis is friction coefficient. Initially

friction coefficient is stable on some level, after applying normal load friction coefficient steadily goes up and, after unloading, drops back to initial level.

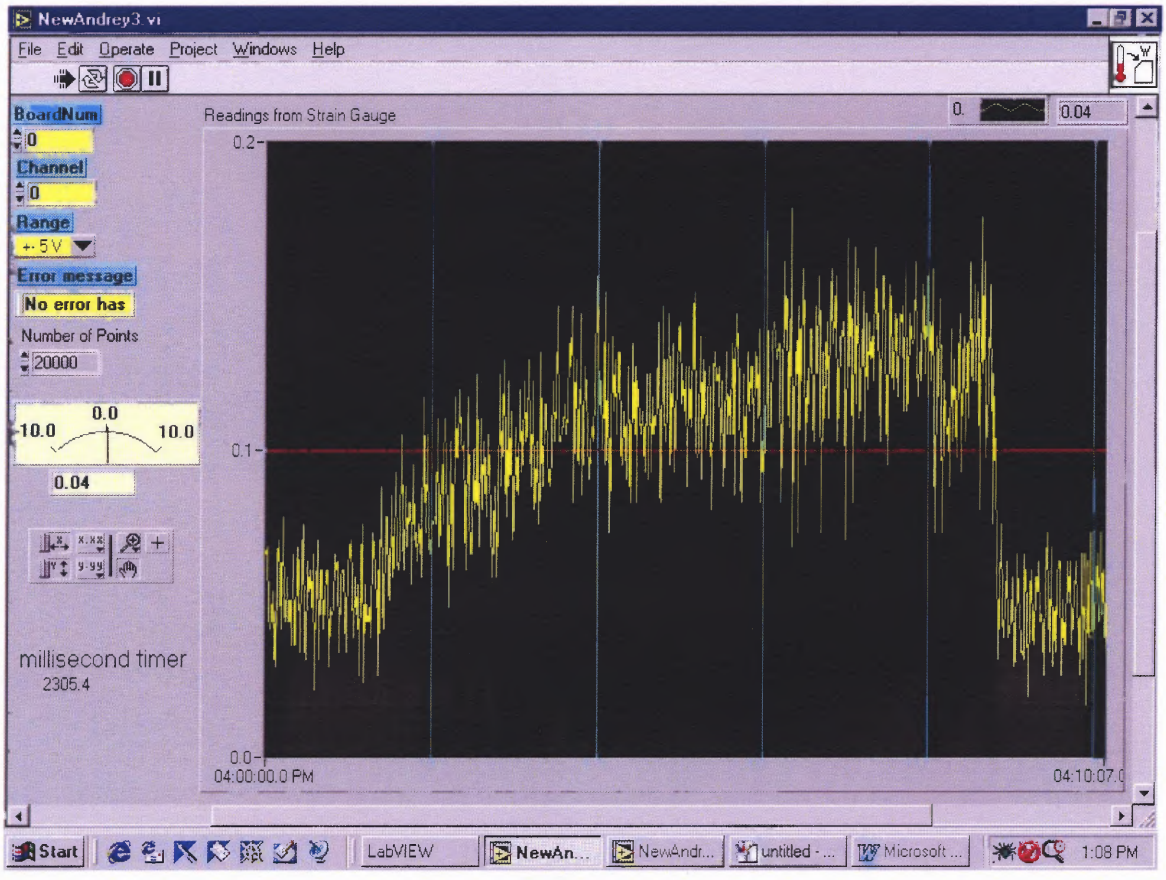

Figure 5.5 Computer screen displays strain gages readings.

5.1.9 System Characteristics

For the design of WFTM, AC motor with constant angular velocity of 150.8 s^{-1} (1,440 *RPM*) was selected. Conversional ratio of the reducer is 6.3 and angular velocity of roller of 23.9 s^{-1} (229 *RPM*), which equivalent of about 0.61 *m/s* sliding speed. Installation of DC motor could make sliding speed variable. The load mechanism consists of the lever system with transmission ratio 72 and the linear sliding-pusher, which can work in

manual and automatic modes. Applied load on entrance lever from 0.23 *kg* (0.5 *lb*) to 1.81 *kg* (4 *lb*) provides 160-1280 *N* range on the shoe. For selected nominal contact area A_a of a shoe, nominal contact pressure ranges from 0.94 *MPa* to 7.5 *MPa*.

5.2 Friction Measurements

Calculations of friction force and friction coefficient are based on measuring power losses in motor that are caused by friction between shoe and roller. Because rotational speed of the motor is constant, any changes in motor power result in changes of moment produced by the stator. General form of moment balance law is following

$$\sum_i \vec{M}_i(t) = J \cdot \frac{d\beta(t)}{dt} \tag{5.1}$$

where J – the inertia moment of the system, $\beta(t)$ – the angular velocity and M_i – moments of all system power generating and power consuming elements. Averaging over a time period T, the fluctuations in the angular velocity disappear and this problem transfers to quasi-stationery equation

$$\frac{1}{T}\int_t^{t+T} \sum_i \vec{M}_i \cdot dt = \sum_i \left\langle \vec{M}_i \right\rangle = 0 \tag{5.2}$$

In WFTM system, M_1 is feeding (driving) moment between stator and rotor to overcome all frictional moments in the system, M_2 is frictional moment in all bearings and reducer and M_3 is frictional moment between shoe and roller. Multiplying this equation by constant angular velocity β leads power balance equation

$$\vec{\beta} \cdot \sum_i \vec{M}_i = 0 \qquad \text{or} \qquad \sum_i \dot{E} = 0 \tag{5.3}$$

Then Equation (5.3) can be expressed as

$$\dot{E}_1 = \dot{E}_2 + \dot{E}_3 \tag{5.4}$$

where $\dot{E}_1$ is the total power necessary to spend in order to compensate all losses in the system, $\dot{E}_2$ is the power necessary to compensate losses in all bearings and reducer, and $\dot{E}_3$ is the power necessary to compensate losses between roller and shoe.

$\dot{E}_2$ depends on power $\dot{E}_3$ and can be expanded as $\dot{E}_2(\dot{E}_3)$ function into the Taylor series. Only first two members of $\dot{E}_2(\dot{E}_3)$ Taylor series can be considered and Equation (5.4) becomes

$$\dot{E}_1 = \dot{E}_{20} + \frac{\partial \dot{E}_2}{\partial \dot{E}_3} \cdot \dot{E}_3 + \dot{E}_3 \tag{5.5}$$

where $\dot{E}_{20}$ is constant frictional losses, which do not depend on $\dot{E}_3$. $\dot{E}_3$ can be derived from Equation (5.5)

$$\dot{E}_3 = \frac{\dot{E}_1 - \dot{E}_{20}}{1+k}, \text{ where } k = \frac{\partial \dot{E}_2}{\partial \dot{E}_3} \tag{5.6}$$

Assuming that power losses in bearings have both constant and linearly changing components and so k is a constant of the system, friction moment can be determined.

For measuring magnetic moment between rotor and stator in AC electrical motor, the beam with strain gages was attached to the suspended stator. Schematic representation of the suspended motor and description of the used terms are shown in

Figure 5.6. Thus, $\dot{E}_3$ can be expressed through friction force F between roller and shoe and $\dot{E}_1$ and $\dot{E}_{20}$ through the reaction forces N_r and N_{ro}

$$\dot{E}_3 = F \cdot r_r \cdot \beta_o \tag{5.7}$$

$$\dot{E}_1 = N_r \cdot d_m \cdot \beta_t \tag{5.8}$$

$$\dot{E}_{20} = N_{r0} \cdot d_m \cdot \beta_t \tag{5.9}$$

where F is the friction force between the roller and the shoe, r_r – radius of the roller, β_t and β_o – angular speed of the rotor and roller respectively, N_r – the reaction force acting on the beam, N_{ro} – the reaction force acting on the beam under zero applied load and d_m – the distance from the rotor axis to the point of reaction.

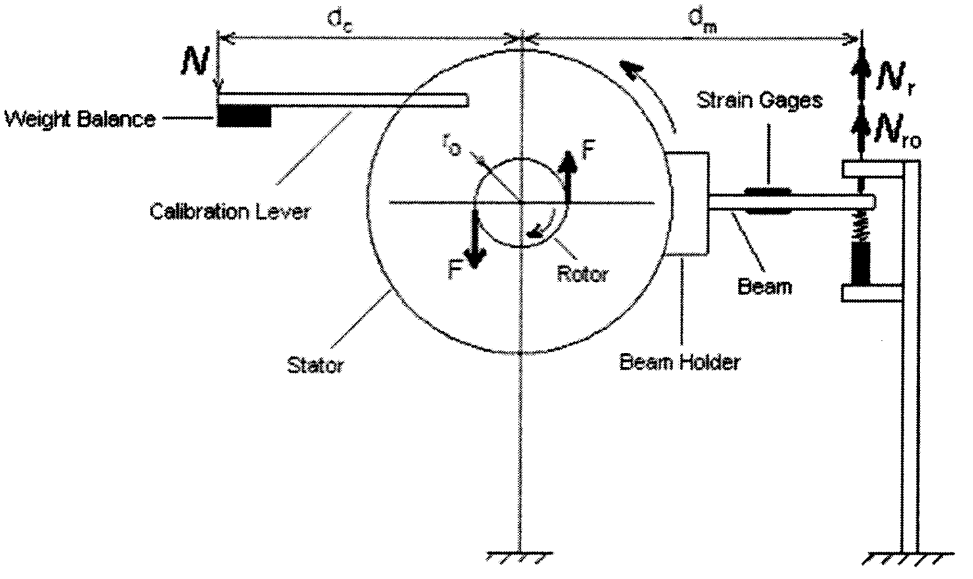

Figure 5.6 Scheme of the suspended motor.

Substitution of Equation (5.7-5.9) into Equation (5.6) gives

$$F \cdot r_r \cdot \beta_o = \frac{1}{1+k} \cdot (N_r - N_{ro}) \cdot d_m \cdot \beta_t \tag{5.10}$$

Friction force F is equal to product of friction coefficient f on applied normal force N. Then friction coefficient f can be calculated by following expression

$$f = \frac{1}{N(1+k)} \cdot (N_r - N_{ro}) \cdot \frac{d_m \beta_t}{r_r \beta_o} \tag{5.11}$$

In this formula k, β_o, β_t, d_m and r_r are the constants of the system and the value of N_r can be obtained from strain gauges. Calibration of the system is done by gradually applying known forces N_c on the distance d_c from the rotor center on the side of the motor opposite to the stator's bar as shown in Figure 5.6. Calibration chart, shown in Figure 5.7, represents relationship between strain gage readings and calibration moment, which can be calculated as

$$M_m = W_c \cdot d_c \tag{5.12}$$

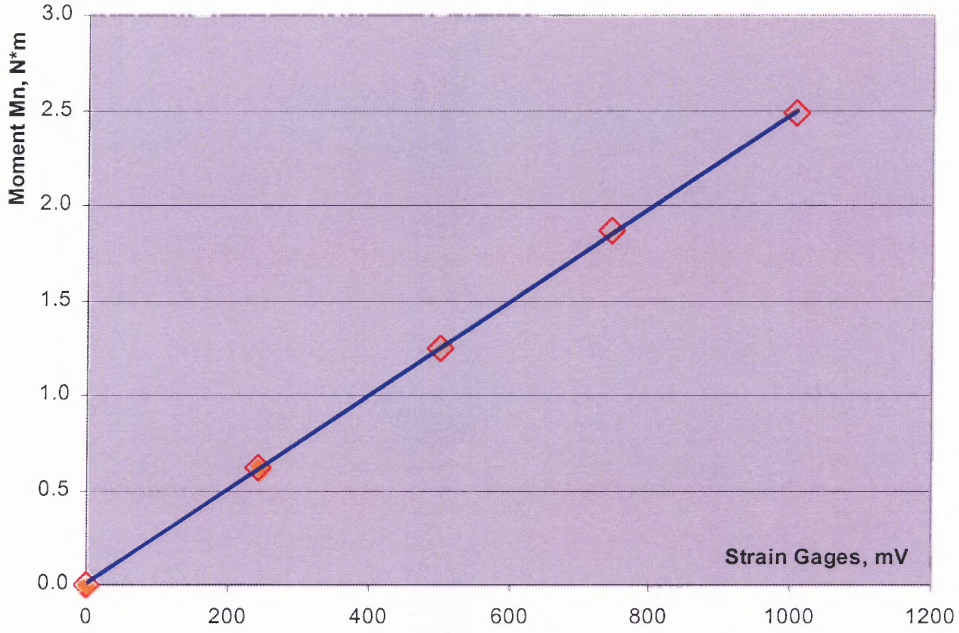

Figure 5.7 Calibration chart of strain gages.

As the result of this calibration, the dependence between strain gauge readings and reactive moment was developed. Using the calibration graph, computer system converts the signal obtained from strain gauges to the moment generated by stator and, as a result, calculates friction moment, friction force and friction coefficient. This approach provides the researcher with needed test data at any moment of a test. These data help to define different stages of friction and wear and are an important step in understanding the processes that take place in friction phenomenon.

5.3 Wear Measurements

The idea of wear rate evaluation is based on measurement of distance between the center of roller and the shoe's bottom. For these purposes, Digital Linear Gage is attached to the moving table on which the shoe is fixed.

5.3.1 Digital Linear Gage

Operable by remote control, IDF Digimatic Indicator of Mitutoyo allows tracking any changes in thickness of a tested material. Figure 5.1 shows the scheme of wear rate measurements. On this picture, steel roller fixed to stationary axle rubs against bronze shoe, which is placed on movable platform that is loaded by applied normal force N. During test time, bronze shoe experiences wear and its thickness decreases. Digital linear gage attached to the stationary axle, as shown in Figure 5.8, tracks changes in shoe thickness Δl during test.

Digital linear gage can work in two modes: manual – pushing button on the gage top triggers sending its current reading through the input tool to the computer and automatic – computer program periodically forwards 1-bit signal through the input tool to

the gage and gets back reverse signal from the digital linear gage. Technical characteristics of the gage also include a miniature linear encoder, preset capability and SPC output, a maximum response speed is 31.5 *"/s*. The operational range of this model is from zero up to 25 *mm* (1*"*) with accuracy of up to .00005*"* (0.001 *mm*).

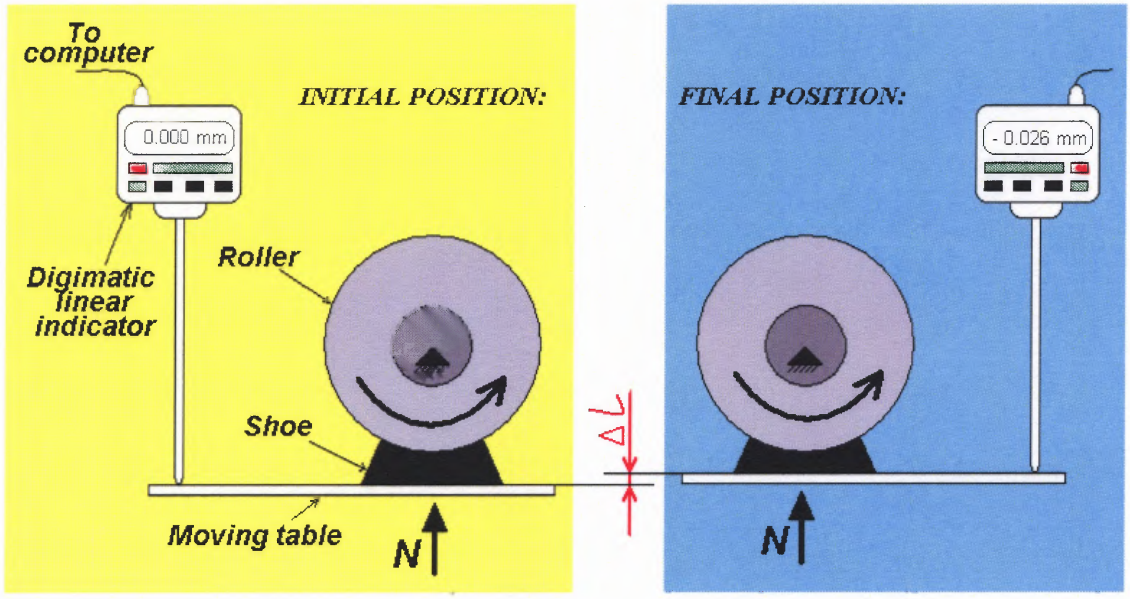

Figure 5.8 Scheme of wear rate assessment.

Input tool IT-007 R of Mitutoyo passes activation signal from the computer to the linear gage and sends back data signal from linear gage to the computer. This mode provides automatic measurement and control. Input tool is PC/AT, PC/AT-compatible, and compatible machines with an R-232C interface.

5.3.2 Visual C++ Application

For the control of digital linear gage, Visual C++ program was developed and installed. The tasks of this program are sending 1-bit signal with specified frequency, receiving back signal from digital linear gage, synchronizing obtained signal with timer and saving all this information to file. Because of synchronization of this program with LabView application program, the frequency of data collecting is set up at 1 *Hz*. The complete Visual C++ program is shown in Appendix B.

5.3.3 Calculations of Wear Rate

Estimation of wear rate and weight loss is based on the measurement of distance between the center of the roller and the shoe's bottom. This distance multiplied by nominal contact area A_a and material density ρ gives weight loss W of the tested sample

$$W = \Delta l \cdot A_a \cdot \rho \tag{59}$$

In addition, tested samples have been weighed before and after each test. The performed experiments for heavy-duty boundary conditions showed good alignment – within 5 % – between online data and before-and-after test weight measurements.

5.4 Surface Texture Analysis

Surface analysis is applied to both roller and shoe and assesses various parameters of examined surface texture such as profile depth P_t, roughness depth R_z, mean roughness R_a, material ratio t_p and others. For these purposes, Perthometer PGK of Mahr Federal with testing accuracy of 0.01 μm was used. Some surface texture profiles and parameters are shown in Figure 5.9 and Table 5.1.

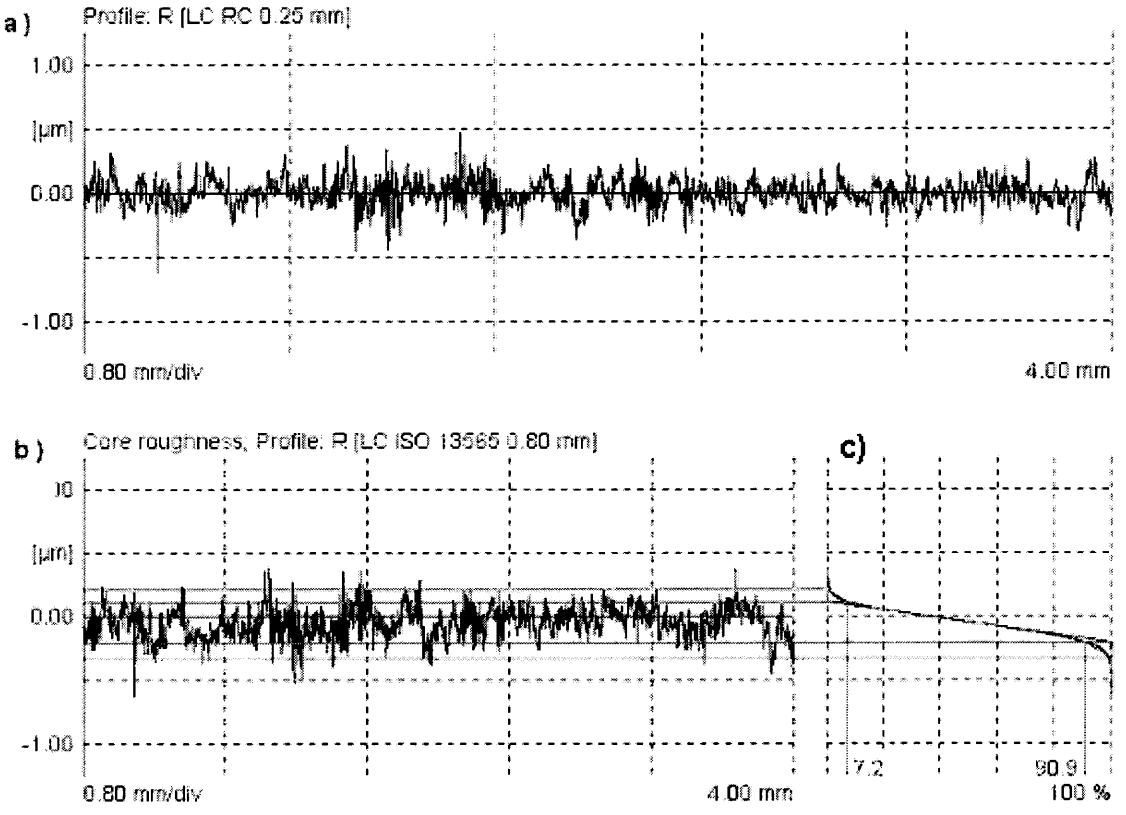

Figure 5.9 Surface analysis characteristics: a) roughness profile, b) core roughness and c) material ratio profiles.

Table 5.1 Major Surface Texture Parameters

Term	*Symbol*	*Value*	*Term*	*Symbol*	*Value*
Cutoff	*LC (RC)*	0.25 mm	Core roughness depth	R_k	0.32 µm
Traversing Length	*LT*	5.60 mm	Reduced peak height	R_{pk}	0.10 µm
Evaluating Length	*LM*	4.00 mm	Reduced valley depth	R_{vk}	0.12 µm
Roughness average	R_a	0.08 µm	Waviness height	W_t	1.48 µm
Mean roughness depth	R_z	0.71 µm	Arithmetic mean deviation	W_a	0.30 µm
Maximum single roughness depth	R_z *max*	0.93 µm	Profile depth	P_t	3.46 µm
Mean profile valley depth	R_v	0.40 µm	Arithmetic mean deviation	P_a	0.55 µm

Surface texture observations were performed on Olympus optical microscope furnished with Clemex imaging system, which allows to examine texture of shoe and roller before and after experiment, store and process these data later on. The tools of image processing include assessment of surface material structure, seizure, pits, bulk distortion and others. An example of optical microscope image is shown in Figure 5.10.

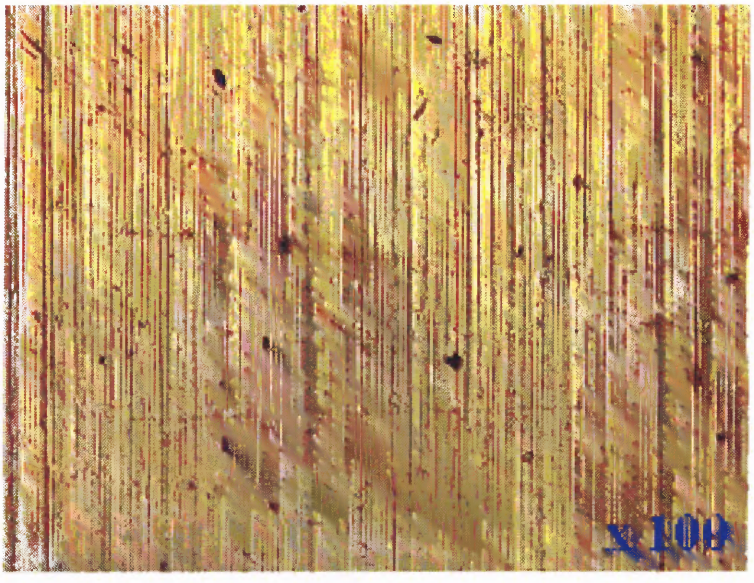

Figure 5.10 Optical microscope image of bronze shoe (x 100).

5.5 Data Processing

After data collecting, readings are processed on Microsoft Excel. Final test data include all essential characteristics of the test such as length of the test, applied normal load, normal force, strain gage readings, power losses, friction moment, friction force, friction coefficient, digital linear gage readings and wear rate and weight loss of a tested sample. The graphs of friction coefficient and wear or weight loss are superimposed on each other and their dependence on time is shown. Examples of the described dependence are shown in Figures 5.11 and 5.12.

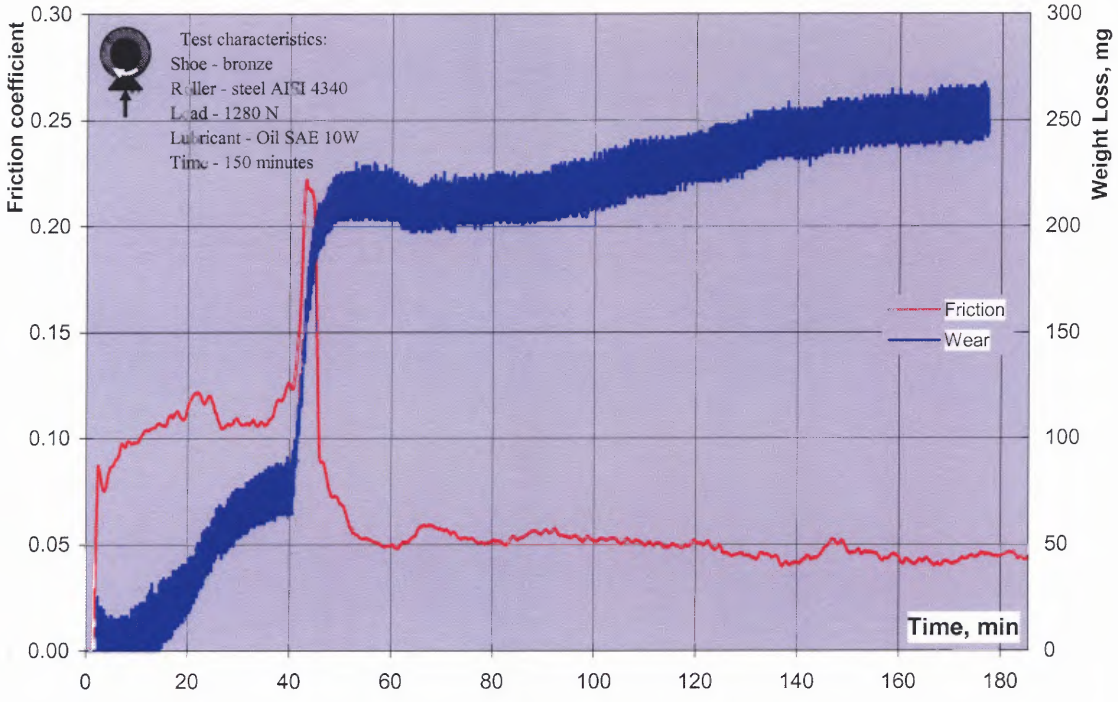

Figure 5.11 Dependence of friction coefficient and total weight loss of bronze shoe on time.

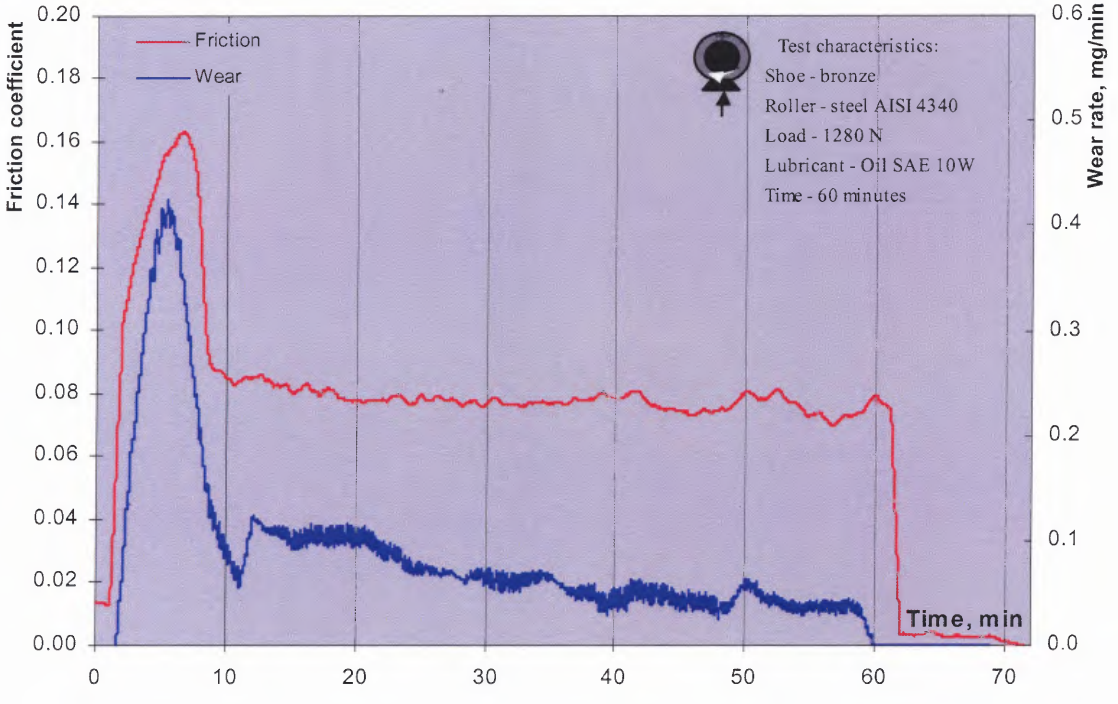

Figure 5.12 Dependence of friction coefficient and wear rate on time.

CHAPTER 6

EXPERIMENTAL RESULTS

Experimental performance analysis of the base lubricant modified by the selected additives is based on evaluation of friction behavior of bronze-steel couple, assessment of wear rate and weight loss of materials in contact and their surface texture analysis before and after experiments. The experimental setup, test condition and lubrication regime are described in Chapter 5. Tested materials bronze SAE 40 and steel AISI 4340 and their surface texture characteristics are demonstrated in Section 6.1. The grounds of the selection of the base heavy-duty motor oil SAE 10 and its properties are listed in Section 6.2. Summary of fullerene C_{60} properties and brief overview of other fullerenes and fullerene containing soot is illustrated in Section 6.3.

Study was carried out in two experiment series – Series 1 and Series 2. Series 1 included analysis of three types of additives - fullerene C_{60}, fullerene mixture C_{60} and C_{70} (1 to 1) and graphite powder. Series 2 consisted of analysis of graphite powder, 3 *w%* fullerene soot, 7 *w%* fullerene soot and fullerene mixture C_{60} and C_{70} additives as well as plasma treated oil SAE 10. Selected additives in both series 1 and 2 and brief description of their physical properties are shown in Section 6.4. Sections 6.5 and 6.6 are devoted to weight loss and friction measurement results for the selected lubricants.

6.1 Description of Tested Materials

6.1.1 Material Composition and Mechanical Properties

The couple selected for this series of experiments represents common conditions of rubbing materials in mechanisms. First, the materials of rubbing couple are selected in such a way that hardness of one material, roller made of steel AISI 4340, is higher than that of the other, shoe made of bronze SAE 40. This choice creates situation when only soft material experiences noticeable wear and weight loss. Meanwhile, the wear of the second, hard material, can be neglected, see calculations in Chapter 4. Chemical composition and mechanical properties of steel AISI 4340 and bronze SAE 40 are shown in Tables 6.1-6.3.

Table 6.1 Chemical Composition of Steel AISI 4340

Element	*Fe*	*C*	*Ni*	*Cr*	*Mn*	*Mo*	*P*	*S*	*Si*
%	96	0.37 – 0.43	1.83	0.7 – 0.9	0.7	0.2 – 0.3	0.035	0.04	0.04

Table 6.2 Chemical Composition of Bronze SAE 40

Element	*Cu*	*Pb*	*Sn*	*Zn*
%	85	5	5	5

Table 6.3 Mechanical Properties of Steel AISI 4340 and Bronze SAE 40

	Steel AISI 4340 *(annealed)*	*Bronze SAE 40*
Hardness, Brinell	217	60
Tensile Strength, Ultimate	745 MPa	255 MPa
Tensile Strength, Yield	470 MPa	125 MPa
Modulus of Elasticity	200 GPa	93 GPa

Second, selected conforming block-on-ring contact geometry allows to perform extended experiments that simulate operational conditions of machine components in various common mechanisms such as automobile engines and industrial machines.

6.1.2 Surface Texture Parameters

Surface analysis is applied to both contact bodies – steel AISI 4340 roller and bronze SAE 40 shoe. Although surface texture parameters, which can be assessed by available equipment such as Perthometer of Mahr Federal include about 200 various parameters, only major parameters are selected for the detailed consideration. These parameters consist of average roughness R_a, mean roughness depth R_z and skewness R_{sk}. Detailed description of some surface finish parameters is given below:

- average roughness R_a is the arithmetic average of the absolute values of the roughness profile ordinates

$$R_a = \frac{1}{l}\int_0^l |Z(x)|dx \tag{6.1}$$

where l is evaluation length and $Z(x)$ – profile ordinates of the roughness profile.

- mean roughness depth R_z is the arithmetic mean value of single roughness depths R_{zi} of n consecutive sampling lengths

$$R_z = \frac{1}{n}(R_{z1} + R_{z2} + ... + R_{zn)} \tag{6.2}$$

- skewness R_{sk} is a measure of the asymmetry of the amplitude density curve; a negative skewness value indicates a surface with good bearing properties

$$R_{sk} = \frac{1}{R_q^3} \cdot \frac{1}{l}\int_0^l |Z^3(x)|dx \tag{6.3}$$

where R_q – is root mean square roughness.

The accuracy of 0.01 μm and repetitive measurements assure comprehensive picture of the state of contact surfaces. Preparation of surfaces before series of experiments includes development of conforming contact geometry and formation of certain surface texture profiles for both contacting bodies. Each series of experiments has similar surface profiles, but slightly different parameters of steel roller. Due to plastic deformations of bronze shoe, its surface profile experiences slight variations in the way of experiments that, according to the obtained experimental data, did not affect experiment output. Figures 6.1 and 6.2 show surface profiles of roller and shoe (different vertical scales) and values of major surface parameters for Series 1. Statistical analysis of surface texture parameters is shown in Table 6.4.

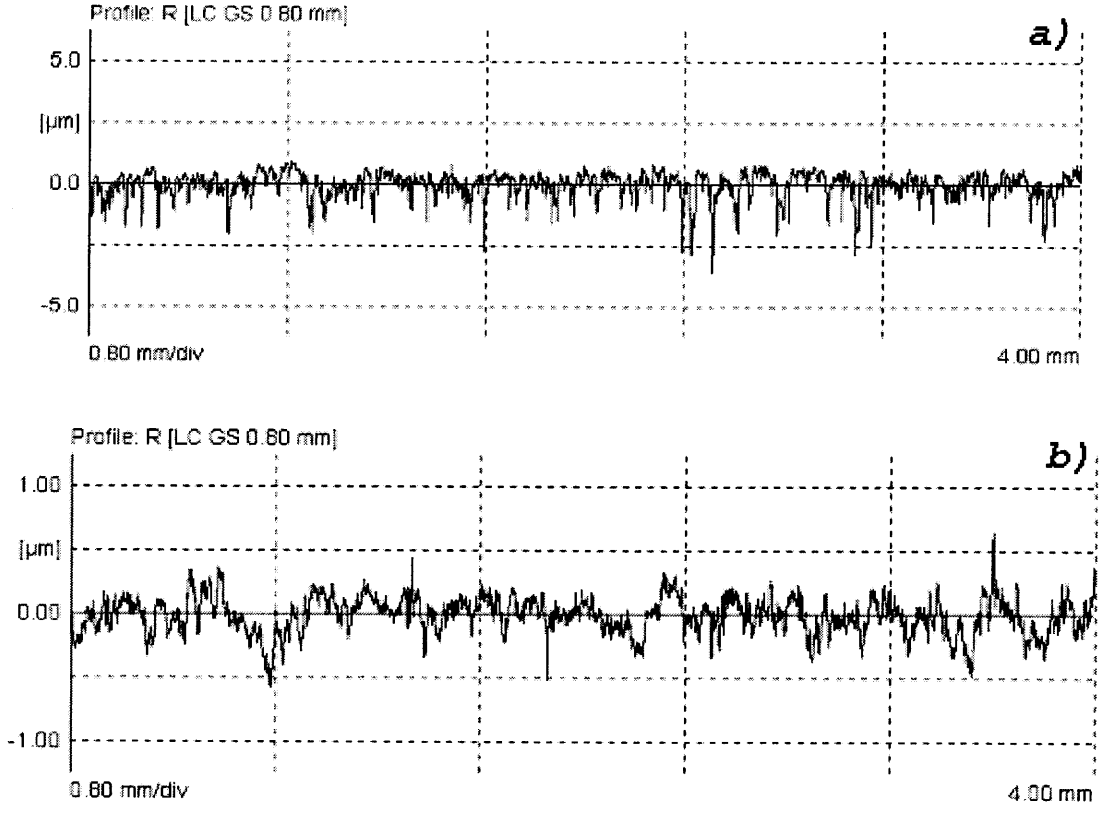

Figure 6.1 Surface texture profile for steel 4340 roller (a) and bronze SAE 40 shoe (b) used in Series 1.

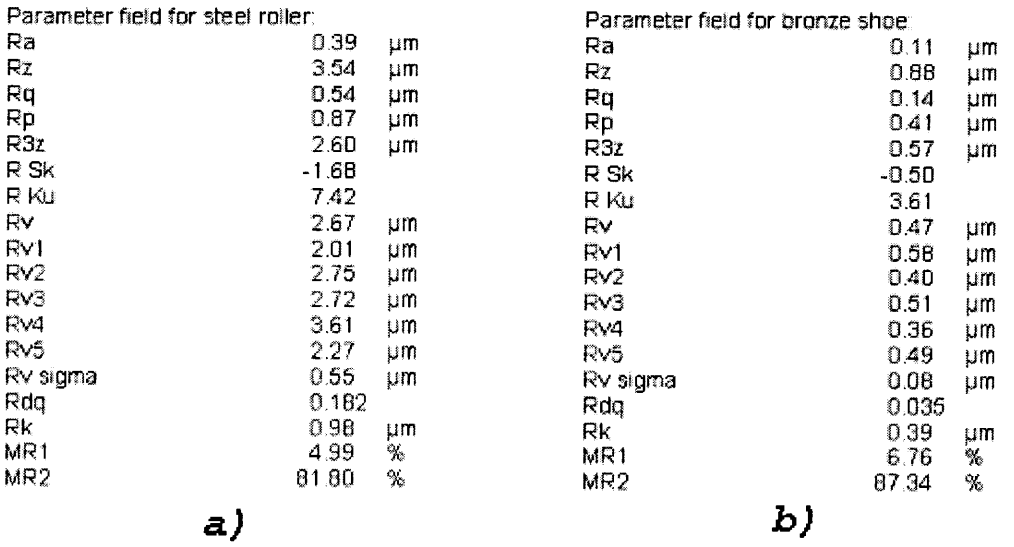

Figure 6.2 Surface texture parameters for steel 4340 roller (a) and bronze SAE 40 shoe (b) used in Series 1 (cut-off LC - 0.25 *mm*, evaluating length LM – 4.00 *mm*).

Table 6.4 Statistical Analysis of Surface Parameters in Experiment Series 1

Parameter	*Average value*	*Standard deviation*	*Standard variance*
R_a, *µm*	0.29	0.03	0.00
R_z, *µm*	3.00	0.47	0.22
R_{sk}, *µm*	1.95	0.48	0.23

Surface profiles of roller and shoe in experiment Series 2 and statistical analysis of surface texture parameters are shown in Figure 6.3 (identical vertical scales) and Table 6.5. Detailed description of surface texture profiles and parameters for both shoe and roller is presented in Appendix A.

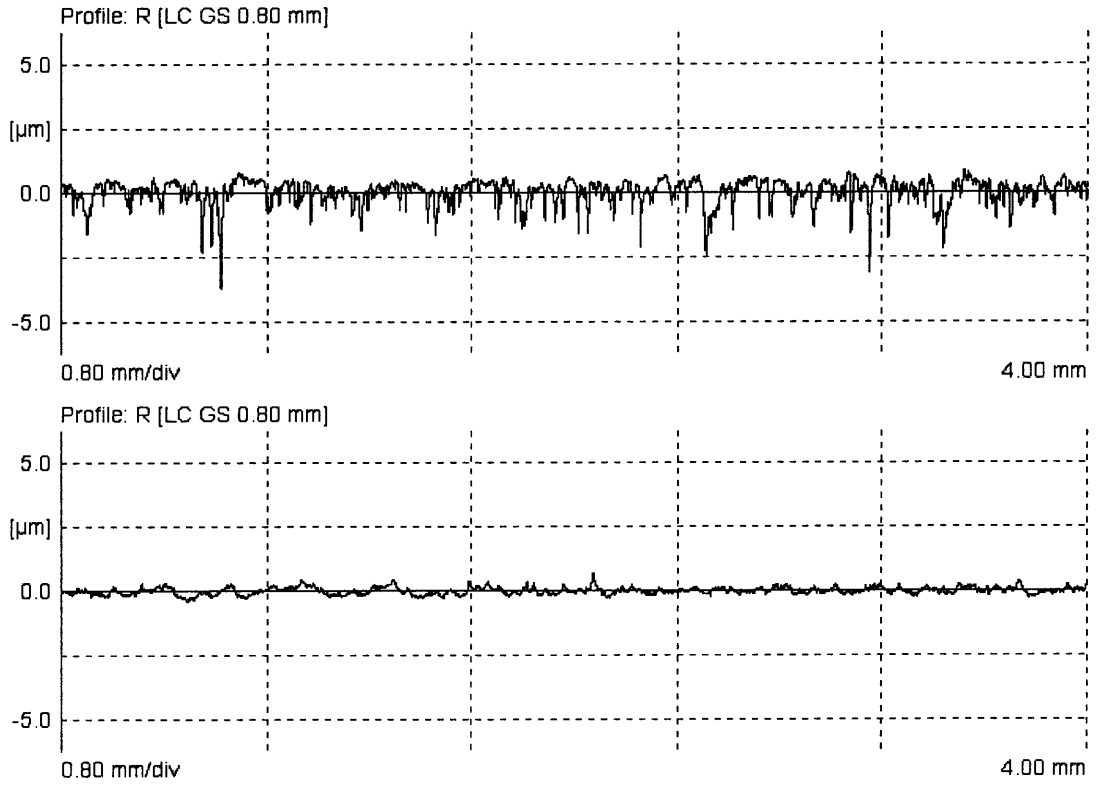

Figure 6.3 Surface texture parameters for (a) steel 4340 roller and (b) bronze SAE 40 shoe used in Series 2 (cut-off *LC* - 0.25 *mm*, evaluating length *LM* – 4.00 *mm*).

Table 6.5 Statistical Analysis of Surface Parameters in Experiment Series 2

Parameter	*Average value*	*Standard deviation*	*Standard variance*
R_a, *µm*	0.31	0.03	0.00
R_z, *µm*	3.00	0.36	0.13
R_{sk}, *µm*	1.77	0.34	0.12

Comparative analysis of surface texture data shows the difference in surface preparation of samples for Series 1 and 2. Although this is not considerable difference, it generated certain difference in results of wear rate and weight loss, which are shown in Section 6.5.

6.2 Base Lubricant

The choice of the base lubricant was dictated by its properties, low price and wide use. Heavy-duty motor oil SAE 10 of Illinois Oil Products is common and inexpensive motor oil, which has applications in such areas of lubrication as automobile motors. This oil is designed for heavy-duty applications in automobile motors and operates in contacts similar to conforming block-on-ring contact presented in wear friction testing machine. Because of its heavy-duty applications, paraffins contribute substantial part to this oil, meanwhile content of aromatic is limited by about 2.4 % and content of naphthenes is negligible. Summary of physical and chemical properties of this base oil is presented in Table 6.6.

Table 6.6 Physical and Chemical Properties of Heavy-duty Motor Oil SAE 10

Content of paraffins (approximate)	**96 %**
Content of aromatics (approximate)	**> 2.4 %**
Naphthene content	**Negligible**
Specific gravity	**0.88**
Viscosity at 40 °C	**11 cSt**
Viscosity at 100 °C	**2.8 cSt**
Appearance	**Amber to light**
Solubility in water	**Negligible**

Presented properties and negligible content of additives make this oil a good starting point for modifications by additives. Selected additives and their properties for both series are discussed in Section 6.4.

6.3 Fullerene Properties

Although tested lubricant additives include various carbon-based materials, fullerene C_{60} is selected as the principal additive for the base oil. Overview of fullerenes is presented in Section 2.5 and summary of basic properties of C_{60} and fullerene FCC structure are shown in Table 6.7 and Figure 6.4.

Table 6.7 Summary of C_{60} Fullerene Properties

Interatomic distance	0.140 and 0.145 *nm*
Molecule diameter	0.71 *nm*
Crystalline structure	*FCC* lattice
Distance between two nearest cage centers	1.003 *nm*
Lattice constant	1.4198 *nm*
Type of molecular bond	Van der Waals
Spinning speed	10^8 *RPS*
Temperature of a phase transition	253 *K*
Crystal density	1.7 $g\ cm^{-3}$
Compression stability	20 *GPa*
Isothermal bulk modulus	18 *GPa*
Cohesive energy per C_{60} molecule	1.5 *eV*
Cohesive energy per atom	7.4 *eV*

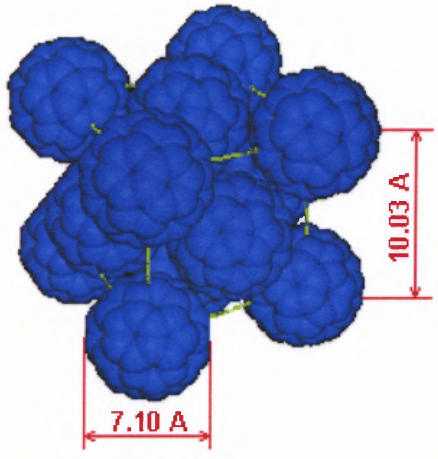

Figure 6.4 Face-centered cubic structure of fullerene C_{60}.

The other additives that used for valid and comprehensive analysis include graphite, C_{70} fullerenes and fullerene containing soot. Chemical and physical properties of C_{70} are analogous to those of C_{60} shown in Table 6.7. Fullerene containing soot consists of various amorphous forms of carbon and carbon onions, brief explanation of which is given in next chapter.

6.4 Tested Additives

6.4.1 Description of Additives

Tested lubricants have been prepared on the base of heavy-duty motor oil SAE 10 by adding one weight percent of selected additives. The amount of 1 *w%* is selected as the maximum solubility of fullerenes C_{60} and C_{70} in SAE 10 oil. In experiment Series 1, the tested lubricants are following:

1. oil SAE10 (base lubricant);
2. oil SAE 10 plus 1 *w%* of graphite powder;
3. oil SAE 10 plus 1 *w%* of C_{60} and C_{70} (1 to 1);
4. oil SAE 10 plus 1 *w%* of C_{60}.

Series 2 was focused on confirmation of results obtained in Series 1 for fullerene C_{60}+C_{70} and graphite mixtures as well as getting comparative results for other modified lubricants. These lubricants include oils with 3 and 7 *w%* fullerene soot and plasma treated oil. The complete list of lubricants used in Series 2 is shown below

1. oil SAE10 (base lubricant);
2. oil SAE 10 plus 1 *w%* of graphite powder;
3. oil SAE 10 plus 1 *w%* of 3 *w%* fullerene soot;

4. oil SAE 10 plus 1 *w%* of 7 *w%* fullerene soot;
5. oil SAE 10, plasma treated;
6. oil SAE 10 plus 1 *w%* of C_{60} and C_{70} (1 to 1).

Graphite powder used in these experiments has surface area – 80 m^2/g and bulk density – 200-230 kg/m^3. Fullerene containing soot, which was used in additives 3 and 4 of Series 2, contains 3 and 7 *w%*, respectively, of fullerenes C_{60} and C_{70} mixture (ratio 1 to 1). The rest is a mixture of amorphous carbon (70-85 *w%*) and variety of carbon onions (10-20 *w%*). Amorphous carbon is a graphite-like structure that possesses low structural as well as chemical stability. Carbon onions are generally described as nanoparticles composed of concentric graphitic layers and exhibit strength of molecules close to that of fullerenes. Transformation of carbon onions to diamond requires pressure above 10 *GPa* and high temperatures. The spacing between the onion shells is about 0.34 nm and the diameter varies from 5 to 40 *nm*.

Incorporation of additives in oil has been performed by ultrasound mixer. In order to avoid any possible impurities, lubricants with fullerene additives C_{60} and C_{70} have been filtered by *Whatman 1* filter paper. The characteristics of this paper are following: particle retention is more than 11 μm, porosity – medium and filtration speed is 40 *s* by ASTM standard test and 150 *s* by Herzberg standard test.

6.4.2 Viscosity Measurements of Prepared Lubricants

To ensure valid comparison of prepared lubricants, their viscosity has been established. Method of measurements is chosen as *falling ball in a tube*. Schematic representation of measuring method is shown in Figure 6.5 and test parameters are following:

Length of the tube, m	$2.95*10^{-1}$
Radius of the ball, m	$5.00*10^{-4}$
Mass of the ball, kg	$8.19*10^{-6}$
Density, kg/m^3	*890*
Ambient temperature, C	*20*

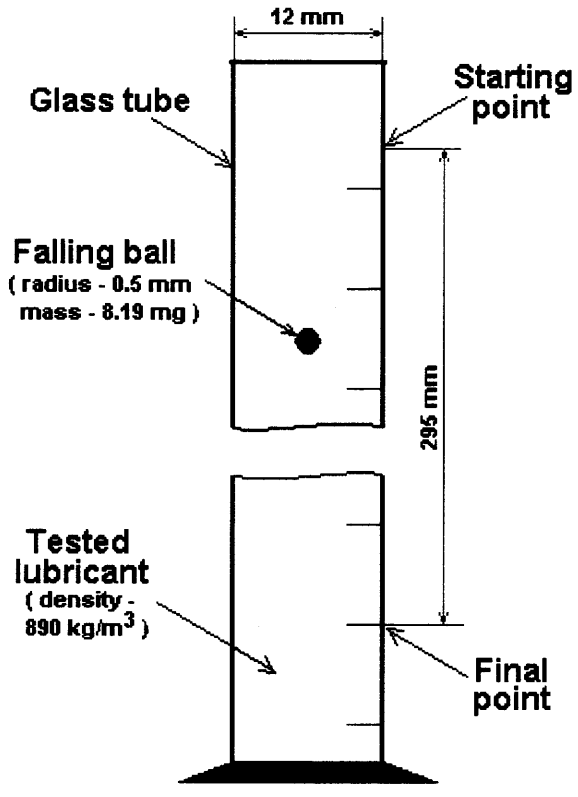

Figure 6.5 Schematic representation of viscosity measuring method.

Test results for dynamic and kinematic viscosity (10 readings for each lubricant) as well as some auxiliary data are shown in Table 6.8.

Table 6.8 Viscosity Test Results for Tested Lubricants

	Time, sec	*Velocity U, m/s*	*Dynamic viscosity, kg/m*s*	*Dynamic viscosity, cP*	*Kinematic viscosity, cSt*
Oil SAE 10	3.43	0.086	0.021	20.6	23 ± 1
Oil + graphite powder	3.35	0.088	0.020	20.2	23 ± 1
Oil + mixture of C_{60} and C_{70}	3.22	0.092	0.020	19.5	22 ± 1
Oil + C_{60}	3.24	0.093	0.020	19.5	22 ± 1
Oil + 3 w% soot	3.52	0.084	0.021	21.2	24 ± 1
Oil + 7 w% soot	3.82	0.077	0.023	23.0	26 ± 1
Plasma oil	3.21	0.092	0.020	19.3	22 ± 1

Kinematic viscosity can be calculated from dynamic (or absolute) viscosity by dividing its value by lubricant density. Dynamic viscosity is presented in two units – kg/m*s and centiposes *cP* and kinematic viscosity in centistokes *cSt*. Viscosity measurements showed that introduction of one weight percent of described additives does not significantly affect the viscosity of the host lubricant and, thus, wear and friction changes in the presence of these lubricants cannot be attributed to changes in viscosity.

6.5 Wear Evaluation of Contact Bodies

Wear evaluation of contact bodies is based on on-line measurements of wear rate and measurements of weight loss of shoe after test. Weight loss results of steel roller showed that it does experience negligible weight loss that confirmed the evaluation made in Chapter 4. Presented data of shoe weight loss are based on 60-minute tests with at least five independent measurements. The length of experiments was selected as 60 minutes (total distance – 2, 200 m) in order to diminish the importance of wear effects in the

beginning period of experiment and to make test relatively long to evaluate performance of lubricants in an extended run. According to online wear measurements, 250-minute experiments showed that except for some initial time period, wear rate stays stable for the entire experiment and wear in the initial period can be neglected. For 30 and less minute experiments, wear in the initial period has to be considered separately that makes weight loss calculation essentially complicated.

The range of applied normal loads was set up as 320 – 640 *N*. Upper limit of this selection, 640 *N*, was selected as the maximum applied load under which friction coefficient can be stable. Loads higher than 640 *N* sometimes cause catastrophic wear of contact bodies that is unacceptable in these experiment series. Lower limit of applied loads was dictated by capabilities of wear friction testing machine – below 320 *N*, and even at this load, experimental data become inconsistent. These limitations are associated with vibrations of the whole system. Despite its relatively low value, system vibrations significantly affect experiment outcome for low applied normal loads.

6.5.1 Experimental Data for Series 1

Results of weight loss measurements for applied normal loads of 320 *N*, 480 *N* and 640 *N* for experiment Series 1 are shown in Figure 6.6-6.8. Presented diagrams show that introduction of 1 *w%* of C_{60} and C_{60}+C_{70} mixture as well as graphite powder into the base lubricant improves its properties.

Shoe weight loss results have similar character for both loads – 480 and 640 *N* and illustrate certain advantage of C_{60}+C_{70} mixture over C_{60} additive and graphite lubricants. C_{60} additives improve the wear performance of the host lubricant by approximately 12 % for applied normal load of 640 *N* and about 22 % for 480 *N* loads.

C_{60}+C_{70} mixture additives decrease the weight loss of tested materials by about 33 % for 640 *N* and about 50 % for 480 *N*. Graphite powder shows improvement of wear results by about 15 % for 640 *N* and 39 % for 480 *N* load.

Comparative analysis of the presented lubricants shows that both C_{60} and C_{60}+C_{70} mixture notably improve the performance of the base lubricant. Moreover, C_{60}+C_{70} mixture showed better performance than graphite powder by about 27 % for 640 *N* load and about 28 % for 480 *N* load. In addition, C_{60}+C_{70} mixture has advantage in performance over C_{60} additive – about 25 % for 640 *N* applied load and about 29 % for 480 *N* load.

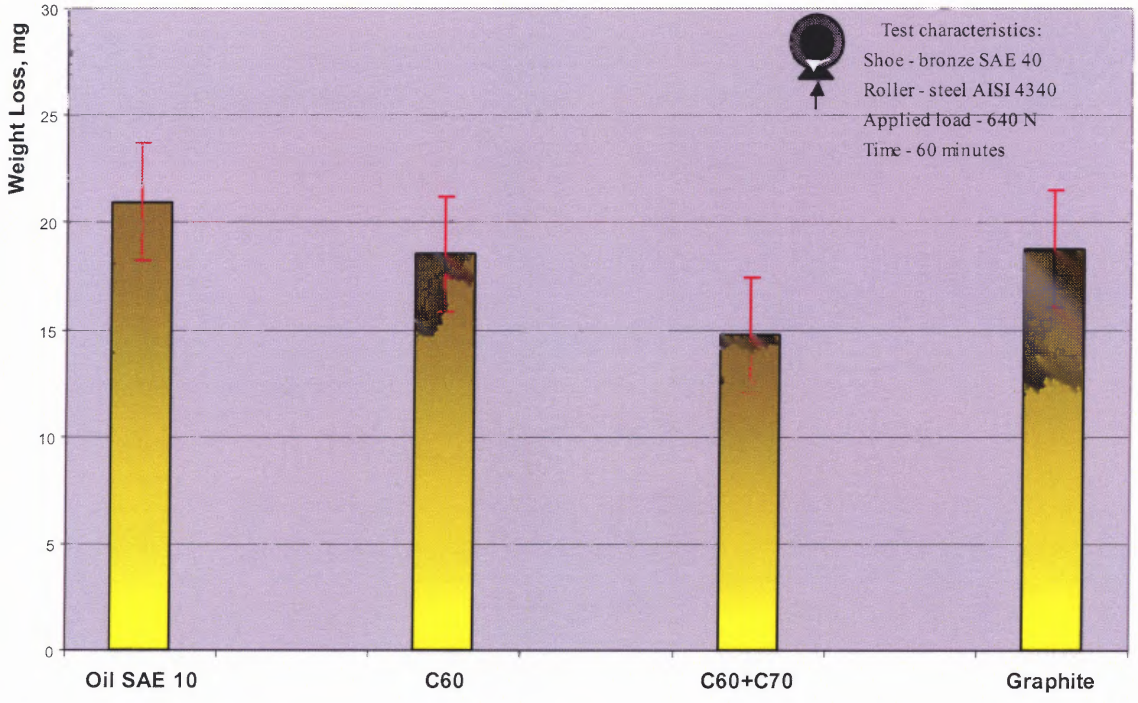

Figure 6.6 Weight loss of bronze shoe against steel roller for 640 *N* load for different lubricants in Series 1.

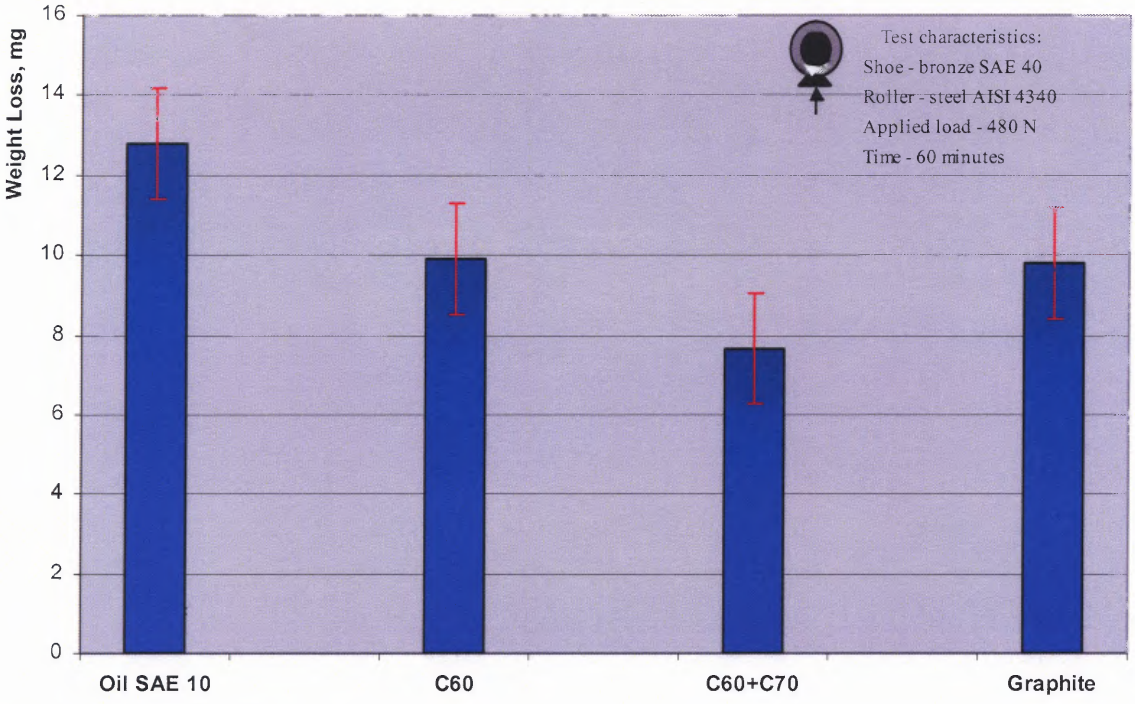

Figure 6.7 Weight loss of bronze shoe against steel roller for 480 *N* load for different lubricants in Series 1.

Finally, C_{60} additives and graphite powder demonstrated similar wear improvement performance; there is negligible difference of about ± 1 % for both 480 and 640 *N* applied normal loads.

Although the data for applied normal force of 320 *N* does not show consistency, data for other two sub series – 480 *N* and 640 *N* – stay in line with the proposed idea. Possible explanation of discrepancy between 320 *N* sub series and other two sub series is that the designed wear friction testing machine does not possess appropriate sensitivity for low applied normal loads.

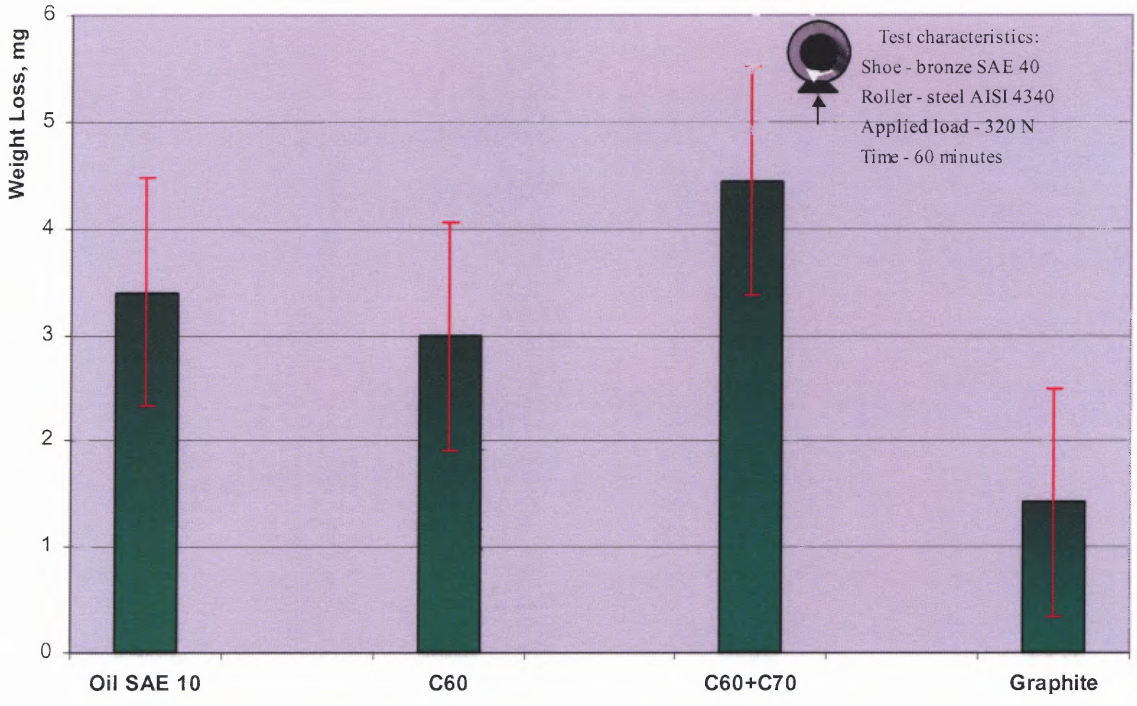

Figure 6.8 Weight loss of bronze shoe against steel roller for 320 *N* load for different lubricants in Series 1.

6.5.2 Experimental Data for Series 2

The goal of Series 2 was obtaining additional experimental data for C_{60}+C_{70} mixture performance as well as assessment of other additives. This series of experiments includes testing of, besides the base oil, five different lubricants; their description is given in Chapter 6.4. Results of weight loss measurements in Series 2 are shown in Figures 6.9-6.11.

Comparison of the performance of C_{60}+C_{70} mixture and graphite powder showed results similar to those obtained in Series 1. C_{60}+C_{70} mixture demonstrates better performance than graphite mixture for both applied normal loads. Finally, introduction of these additives showed some improvement in comparison with the host lubricant in both series.

Introduction of fullerene containing soot into the base lubricant gives results similar to those for fullerene C_{60} and mixture of C_{60} and C_{70}. Possible explanation of this outcome is chemical composition and properties of this soot. Although presented soot has low fullerene content, the presence of carbon onions (10-20 *w%*) and amorphous carbon (70-85 *w%*) in its composition makes it valuable lubricant additive. Similar nanoparticles but on the base of halogens, tungsten and sulfur are currently used in lubrication applications.

Performance data for the oil with both 3 *w%* and 7 *w%* fullerene containing soot show close results – these lubricants improve wear by 10 and 11 *%*, respectively, over the base lubricant for applied normal load of 640 *N*. Comparison of fullerene containing soot with C_{60}+C_{70} mixture and graphite powder lubricant demonstrates that although fullerene containing soot is better than graphite (4 *%*), it is still inferior to fullerene C_{60}+C_{70} mixture.

Results for plasma treated oil show that for both loads 480 *N* and 640 *N* its performance is poorer than that of the base lubricant. This outcome is in line with the concept that heat-treating of oil and its following degradation make deteriorating effect on oil performance.

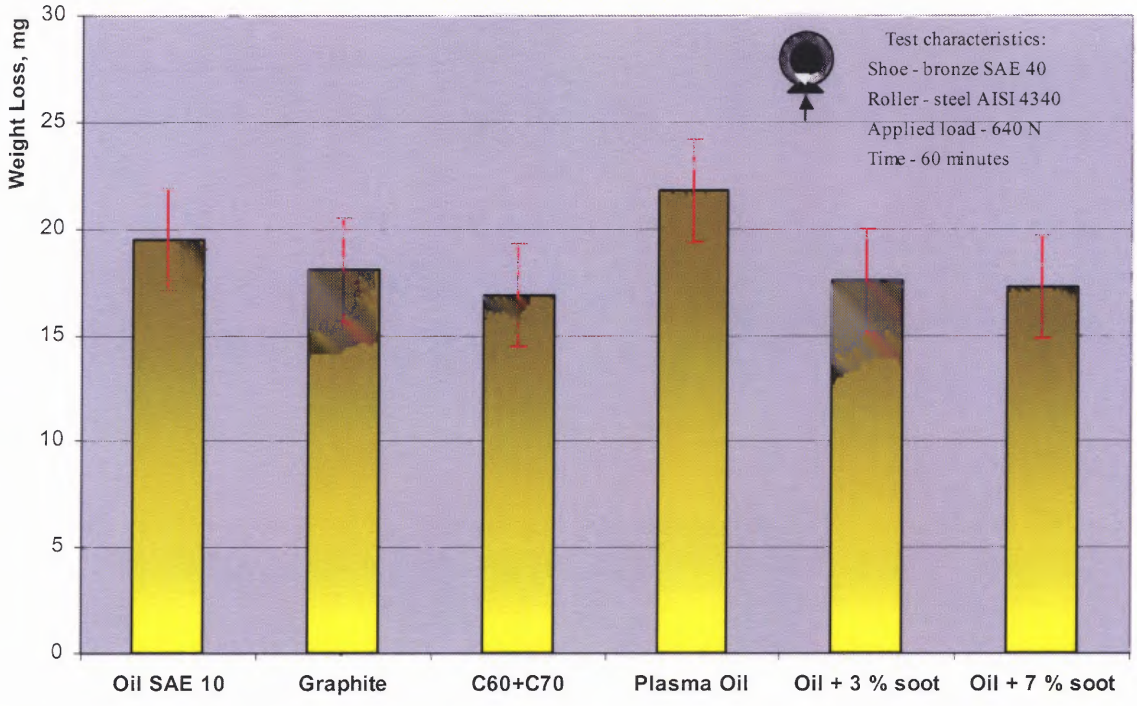

Figure 6.9 Weight loss of bronze shoe against steel roller for 640 *N* load for different lubricants in Series 2.

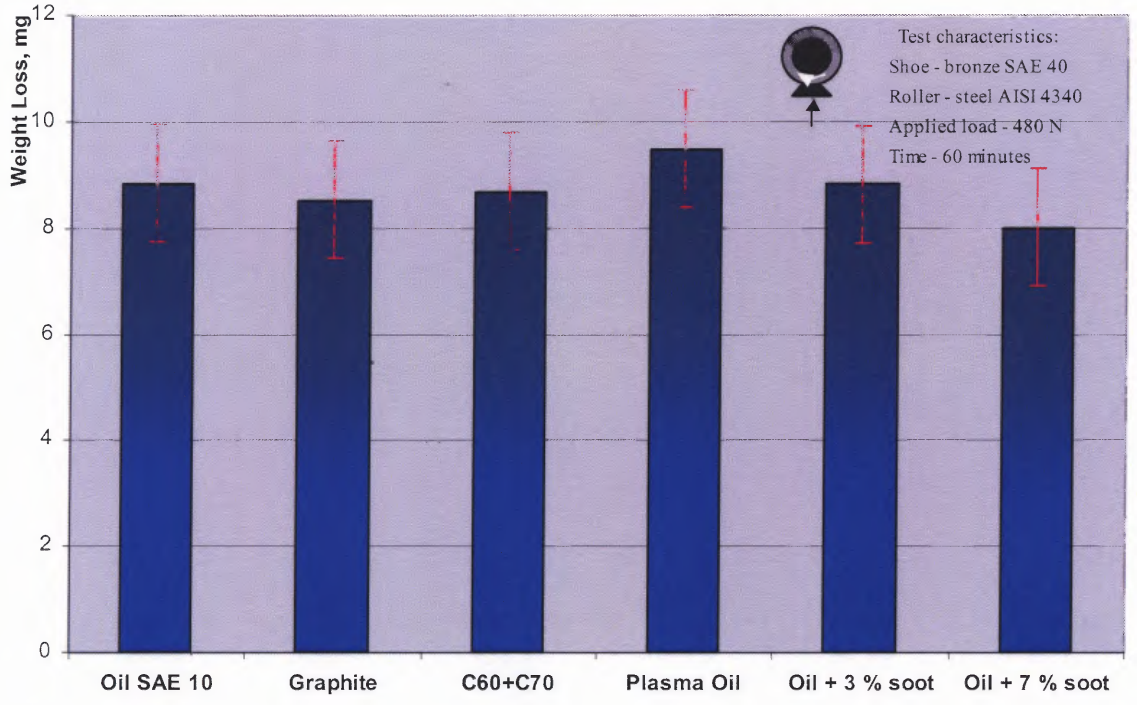

Figure 6.10 Weight loss of bronze shoe against steel roller for 480 *N* load for different lubricants in Series 2.

Inconsistency of results for applied normal load of 320 *N* as well as for some results for 480 *N* load has the same character as in Series 1. This discrepancy is associated with limitations of the presented wear friction testing machine.

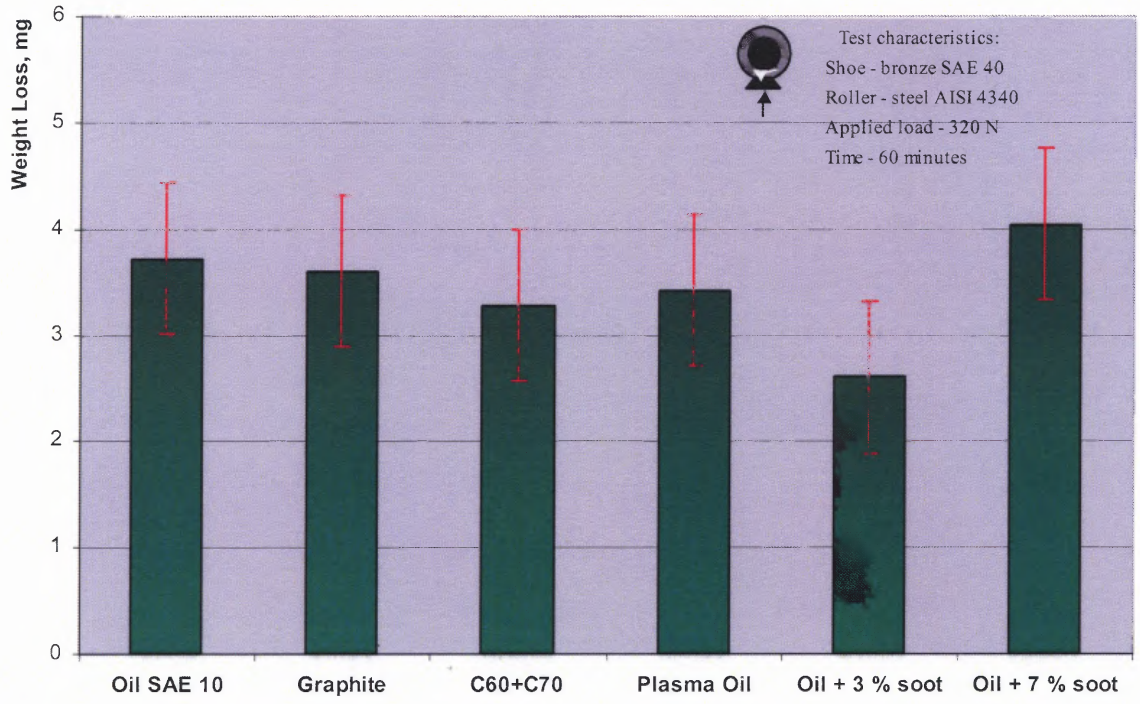

Figure 6.11 Weight loss of bronze shoe against steel roller for 320 *N* load for different lubricants in Series 2.

6.6 Measurements of Friction Parameters

Friction parameters, which include friction moment, friction force and friction coefficient, are essential part for understanding the processes which take part in rubbing of two materials. Experimental results of friction measurements are done for all selected lubricants for applied normal loads of 320, 480 and 640 *N* by getting five independent graphs for each lubricant.

The characters of friction behavior of steel-bronze couple in the presence of the selected lubricants for applied normal load of 480 *N* for Series 1 are shown in Figure 6.12. Data for 320 *N* and 480 *N* applied loads, have similar character. Presented results show that tested additives do not affect friction value of the base lubricant. Although there is certain difference in friction coefficient, it lies in the deviation range of the base lubricant.

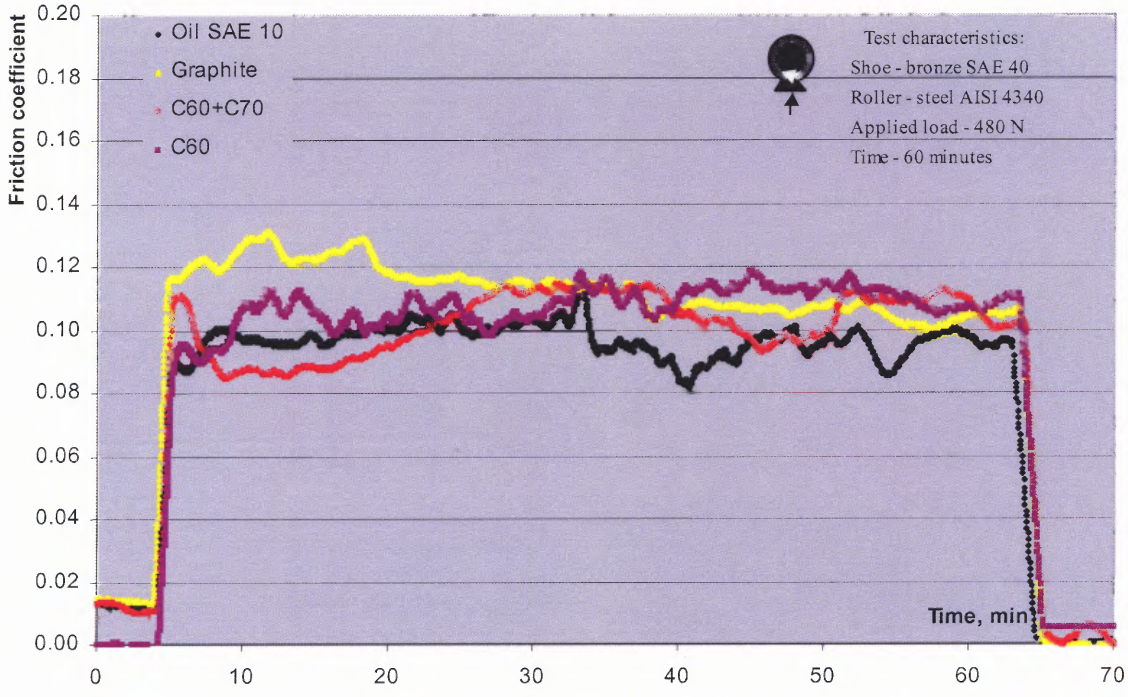

Figure 6.12 Friction coefficient for selected lubricants for 480 *N* load in Series 1.

Friction data for applied normal load of 640 N for lubricants in Series 2 are presented in Figure 6.13. Data for 320 *N* and 480 *N* applied loads, show analogous character. These results show slight improvement in the performance of tested lubricants over the base lubricant oil SAE 10.

Due to the scarce repeatability, demonstrated results do not prove that the tested lubricants essentially improve frictional characteristics of the base lubricant and, therefore, cannot be regarded as antifrictional additives.

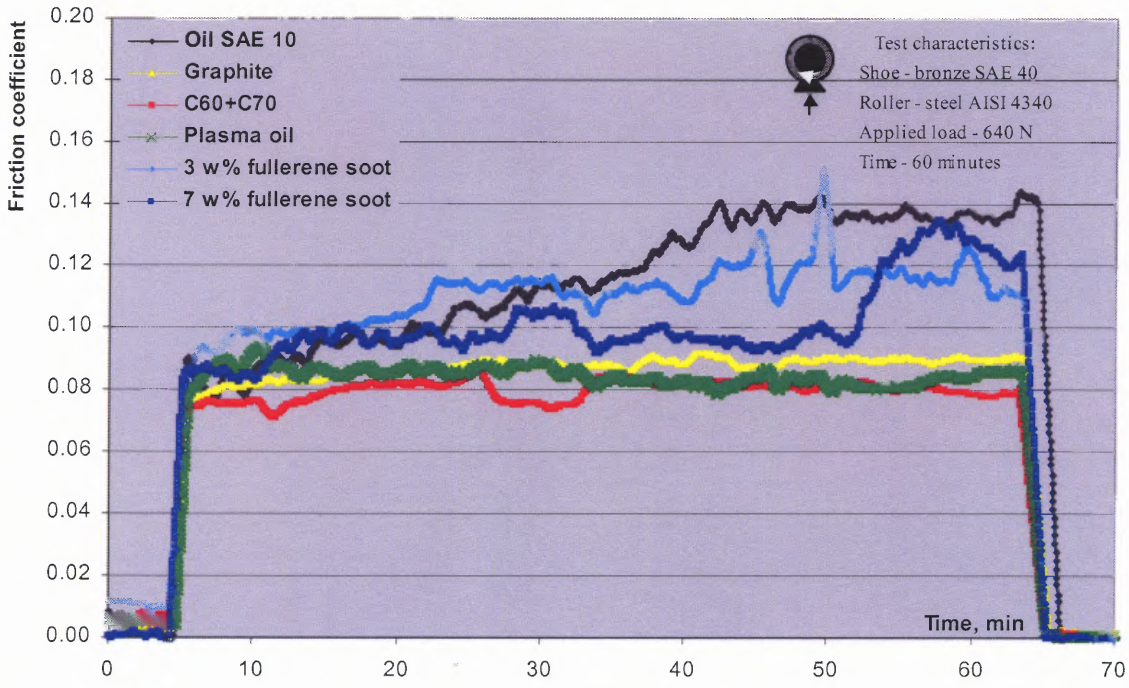

Figure 6.13 Friction coefficient for selected lubricants for 640 *N* load in Series 2.

Friction analysis shows that although presented additives improve wear of materials in contact, they only insignificantly affect friction characteristics of bodies in contact.

CHAPTER 7

ASSESSMENT OF FULLERENE ROLE IN LUBRICANT MODIFICATION

Fullerene role as additives to liquid lubricants used in boundary lubrication is based on review of lubrication characteristics, testing of the properties of the modified lubricants, measurement of changes in surface texture of the contact materials, evaluation of available methodology and equipment for friction and wear testing and verification of objectivity and consistency of the collected and recorded results.

In boundary lubrication, contact surfaces are not fully separated by lubricant that means the lubricant film is thinner than the height of some of the asperities. This leads to direct asperity contact that, under sliding conditions, results in temperature spikes in the contact areas, surface deterioration by seizure and following wear. Due to high build-up pressure in real contact areas, the liquid lubricant, as a rule, is squeezed out from these zones and may stay only in surface valleys. Thus, its lubricating influence in real contact areas is neglected, metallic surfaces come into contact and wear starts.

Another common problem of liquid lubricants associated with boundary lubrication is acceleration of lubricant oxidation. Although continuing air exposure applications make oil oxidation inevitable, high temperature spikes produced in contact areas significantly speed up this process. Hydrocarbons, which are the base of any lubricant, under sufficient thermal exposure, react with oxygen and form oil soluble hydroperoxides such as aldehydes, ketones and acids [19]. These byproducts reduce the lubricant viscosity and, therefore, significantly decrease lubricant's load carrying capacity. Future oxidation turns hydroperoxides into oil insoluble gums and sludges,

which increase friction between the contact surfaces and cause essential damage to the working surfaces in contact. The lubricant becomes darker and less viscous and, consequently, its overall performance goes down.

The most effective way to prevent direct asperity contact and, therefore, decrease wear and damage of the contact surfaces is to introduce in the interface of the contact certain material or intermediator that will not be easily squeezed out from the contact. This intermediator will serve as a separator between the contact bodies and effect friction and wear. One of such solutions is the use of hard coatings applied to one or both surfaces in contact. Although the use of such coatings has many advantages over conventional lubricants in some application areas, their drawbacks do not allow to make the wide use of these techniques. The principal barriers on the way of wide applications of hard coating are their high cost and time-consuming production. The other efficient solution is the use of antiwear additives to liquid lubricants that is inexpensive and effective method to improve wear and antioxidation resistance of the contact surfaces.

In the present study, fullerenes were used as additives to heavy-duty motor oil SAE 10. Developed lubricants were tested under simulated boundary lubrication conditions by computer controlled wear friction testing machine described in Chapter 5. Estimations of real contact area show that under the presented conditions, real contact area is about 0.23 % of the nominal contact area, see Chapter 4. Surface roughness profiles of contact roller and shoe give excellent understanding of the size of real contact area. These profiles in two different scales with evaluated length of 4.00 *mm* and 0.40 *mm* are illustrated in Figure 7.1. Presented calculations lead to the conclusion that the width of an asperity contact is estimated to be 50-100 *nm*. Scanning electron microscope images

of high magnification (x 300,000) lead to similar assessment, see Figure 7.2. The performed estimations of maximum build up pressure A_r in real contact is about 1.6 *GPa* that is much higher than the computed nominal contact pressure A_a. In spite of the presence of liquid lubricant, this pressure causes significant wear of contact surfaces.

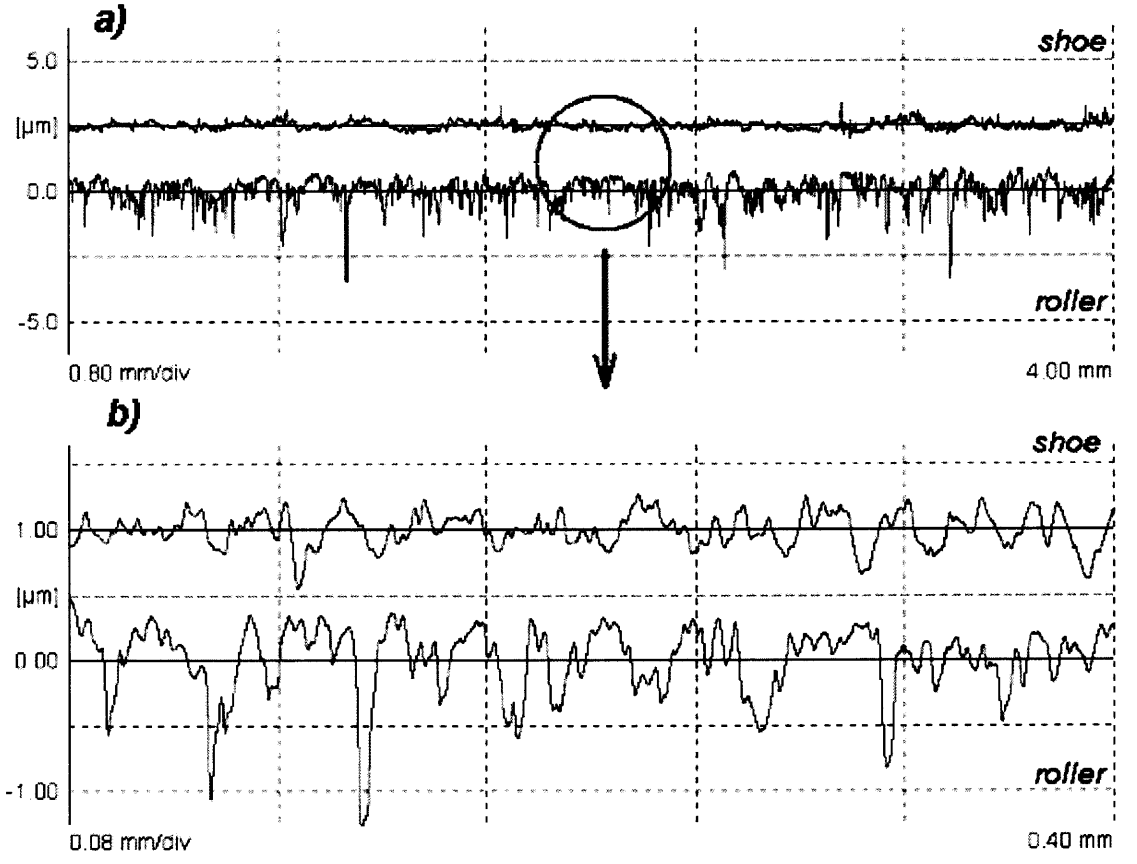

Figure 7.1 Roughness profiles of roller and shoe at different evaluation length: a) evaluation length – 4 *mm* and b) evaluation length – 0.4 *mm*.

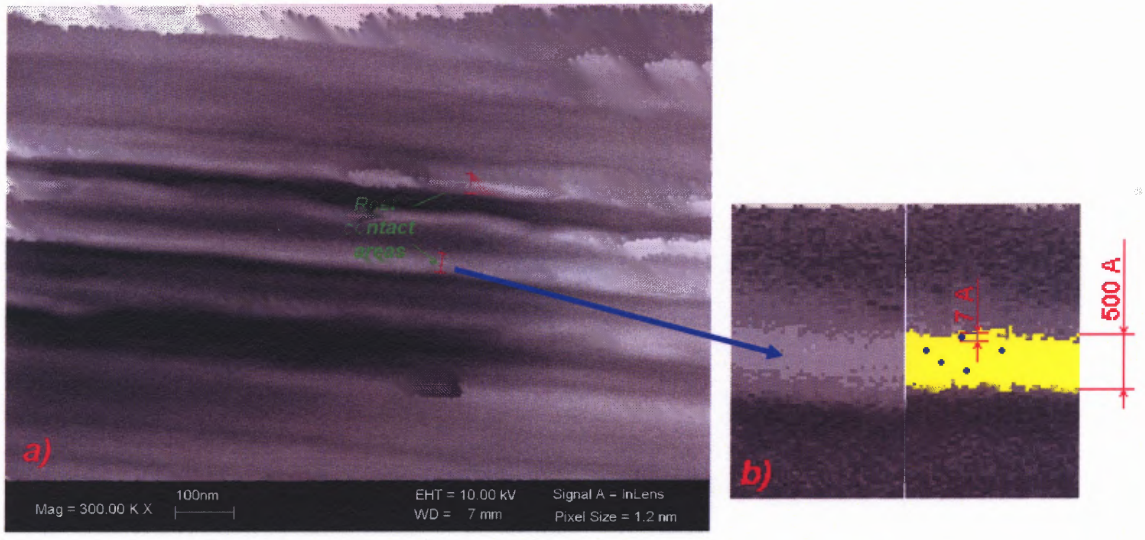

Figure 7.2 Scanning electron microscope image of bronze shoe (x 300,000): a) general image with designation of real contact area and b) comparison of an asperity contact with fullerene size.

The presented experimental results, shown in Chapter 6, demonstrate that fullerenes C_{60} and C_{70} additives improve wear performance of the base lubricant. Introduction of 1 *w%* of fullerene C_{60} and fullerene mixture of C_{60} and C_{70} in heavy-duty motor oil SAE 10 improves its wear performance under boundary lubrication conditions at applied normal loads of 480 and 640 *N*. It can be assumed that because fullerene additives do not change viscosity of the base lubricant and wear resistance of the contact bodies in their presence increases, fullerenes might fully or partially separate surfaces in contact and, therefore, act as intermediator between the two engaged surfaces.

Today evaluation techniques do not allow to prove the presence of fullerenes in real contact area by direct methods. The size of fullerenes, which is about 7 *Å*, can not be detected on the surface of the contact couple by scanning electron microscope or by other available techniques. For these reasons, the possible explanation of fullerene role in

lubricant modification can be based on assumptions and the logical conclusion from the performed investigation and the available information.

Fullerene additives to liquid motor oils are considered to serve as intermediator between two loaded surfaces. Fullerenes C_{60} and C_{70} have the qualities that make possible to use them as liquid lubricant additives: high elasticity of molecules, weak intermolecular interactions, quazispherical shape of molecules, high chemical stability and solubility in oil. Due to strong atomic bonds, fullerenes cannot be easily broken down, and, therefore, stay in contact as hard particles. According to the estimations [78], the stress level required to break fullerenes down at regular room conditions is approximately 20 *GPa*.

Analysis of pressure build up in real contacts and its comparison with the compression stability of fullerenes clearly demonstrate that the pressure required to break fullerenes down is much higher than the stress level that can be achieved in the real contact. Although build up contact pressure may cause plastic deformation in the bronze shoe, its value is insufficient to break fullerenes down. Therefore, fullerenes may be considered as hard particles that, after being delivered to the contact, cannot be easily squeezed out of the contact area. Thus, fullerenes can stay in the area of deformed asperity contact and, depending on the developed build up pressure, be partially or fully pressed in the bulk of contacting materials. Because hardness of steel AISI 4340 is much higher than that of bronze SAE 40 (Brinell 217 versus 60), fullerenes may be forced down mostly into the bulk of bronze shoe. Schematic representation of fullerene behavior in the deformed asperity contact and their role in decreasing wear of surfaces in contact are shown in Figure 7.3.

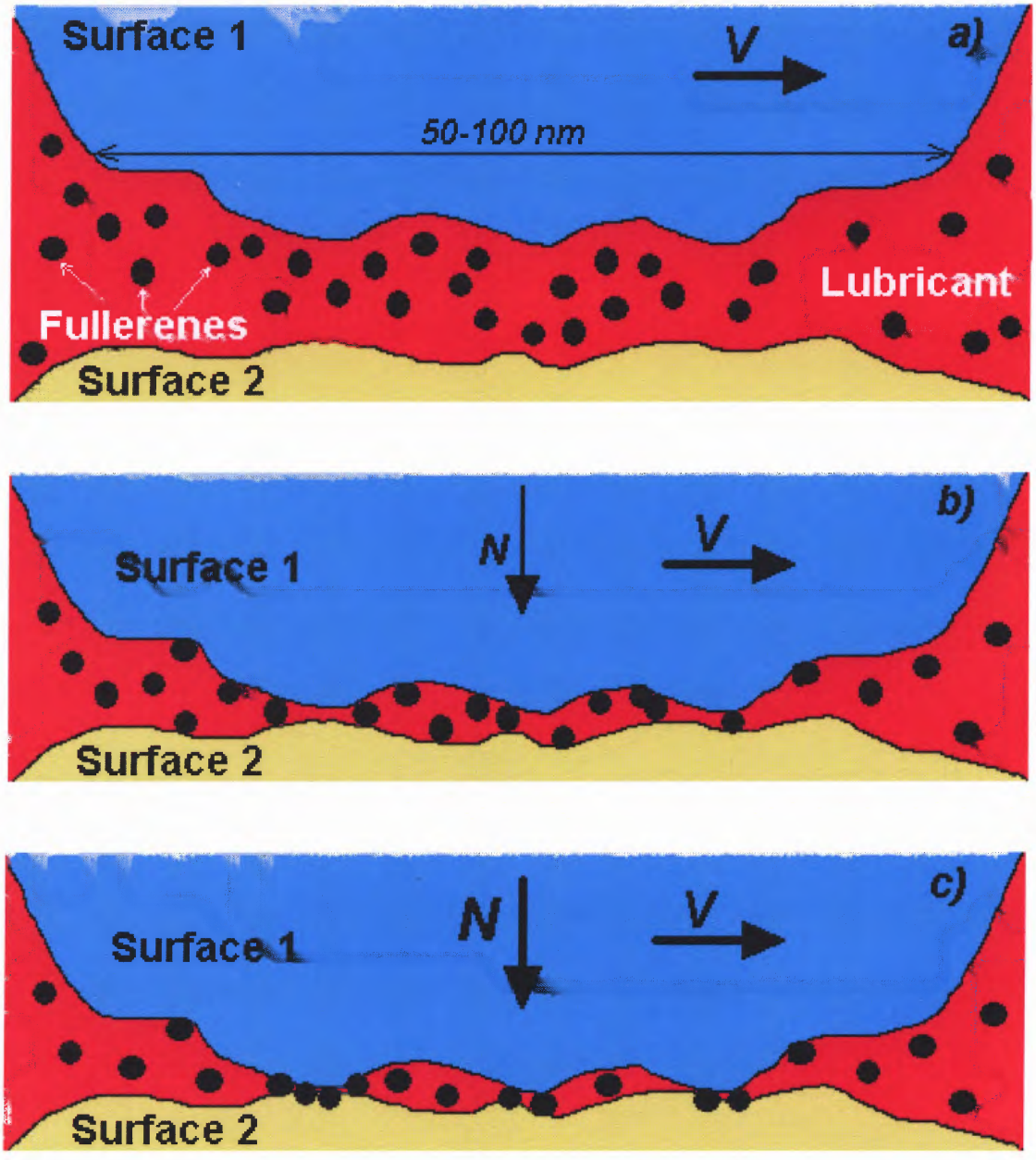

Figure 7.3 Schematic representation of fullerene behavior in asperity contact: a) initial pre-load state of asperity contact in the presence of fullerene content lubricants, b) asperity contact with some light load and c) asperity contact under full load.

According to the evaluation of the deformed contact geometry, the width of an average asperity contact can be covered by up to 10-15 fullerenes C_{60} or C_{70}. Although fullerene concentration, which is one weight percent, does not high enough to provide

dense fullerene layer of the entire contact area, a certain number of fullerenes will positively stay in contact. This leads to the point that the maximum pressure acting on fullerenes in the contact area is relatively higher than the estimated pressure in the real contact that is 1.6 *GPa*. Consequently, fullerenes are partially pressed into the surface of bronze shoe creating a protective layer. The detailed understanding and the stages of fullerene behavior in sliding loaded contact are schematically shown in Figures 7.3 and 7.4.

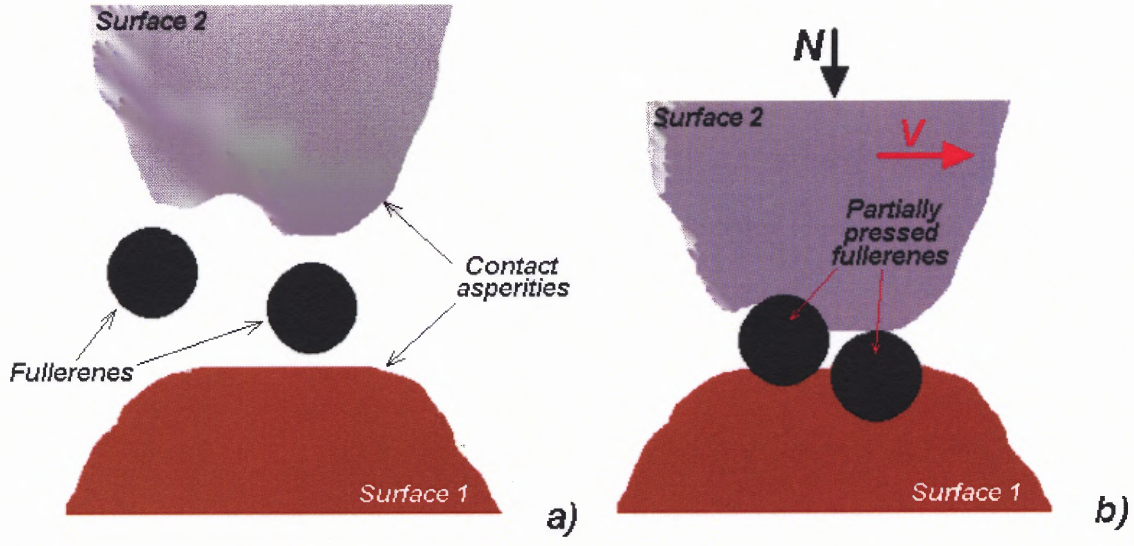

Figure 7.4 Fullerenes in asperity contact: a) no normal load and sliding applied and b) normal load and sliding are applied.

Figures 7.3-a and 7.4-a show the state of an asperity contact without any applied normal load. In these figures, surface 2 is bronze SAE 40 shoe, which is softer than steel AISI 4340 roller, surface 1. Initially, when liquid lubricant is delivered to the contact area, fullerenes are dissolved in the lubricant and are in suspended state. After normal load and tangential force are applied and two surfaces came into direct asperity contact, see Figures 7.3-b,c and 7.4-b, the lubricant is squeezed out from the contact areas, but

fullerenes as hard particles stay and plastically impinged into one of the contact surfaces. Comparison of the build up pressure and the elastic limit, see Table 6.3, allow to conclude that this scenario is most probable. Thus, fullerenes create a protective layer of hard particles on the functional surfaces engaged in contact and prevent direct asperity contact that leads to the increase of wear resistance of the functional surfaces.

The summary of the presented hypothesis can be expressed in the following statements:

- Fullerenes are soluble in mineral oils, possess high chemical stability and do not react with the base lubricant or the contact metal surfaces.
- Fullerenes have high compression stability and the pressure developed in real contact area is insufficient to break them down.
- Fullerenes as hard particles cannot be easily squeezed out from the asperity contact and can be partially or fully pressed into the surfaces in contact.
- Fullerenes act as minute hard balls, partially reduce direct asperity contact and, therefore, decrease wear of contacting functional surfaces.
- Fullerenes can function as oxidation inhibitors by scavenging free radicals and later rebuild them into new harmless structures.

CHAPTER 8

CONCLUSIONS

Modification of existing lubricants by new additives is an important issue in improving and lengthening the lifetime of machine components. The present study discusses the efficiency of fullerenes as additives to liquid lubricants. This study illustrates that the use of fullerenes is beneficial for improvement of wear resistance of steel– bronze friction couple. The achievements of the present research may be summarized as following:

- Computer-controlled wear friction testing methodology was developed and implemented. This methodology consists of computer controlled wear friction testing machine and various research techniques of both quantitative and qualitative analysis of friction-wear experiment output. These methods include evaluation of friction moment, friction force and friction coefficient, calculation of wear rate and weight loss of a tested sample, examination of contact surfaces before and after experiment and collecting, processing and representation of obtained data.

- Heavy-duty standard motor oil was modified by various fullerene containing additives such as fullerene C_{60}, fullerene mixture C_{60} and C_{70}, 3 *w%* fullerene soot and 7 *w%* fullerene soot. Assessment of the prepared lubricants was carried out to ensure that introduction of the selected additives did not make any significant changes in physical properties of the base lubricant.

- Surface texture analysis was applied to the friction couple at different stages of the experimental study. This analysis included evaluation of surface characteristics by profilometer and optical and scanning electron microscopic examination of the surfaces in contact.

- Fullerene containing lubricants were tested for their wear and friction efficiency at various applied normal loads. Despite insignificant changes in friction parameters, fullerene containing lubricants made considerable improvements in wear resistance of selected materials.

- Evaluation of real contact parameters was based on the model of asperity contact of spherical segments. This evaluation showed that real contact area is about 0.023 % of nominal contact area and maximum contact pressure is about 1.6 *GPa*.

- Assessment of the role of fullerene additives to liquid lubricant was developed and presented. This assessment was based on the obtained experimental data and logical conclusions from the performed investigation. Comprehensive picture of friction phenomenon in the presence of fullerene containing lubricants was produced.

This work shows wide perspectives of fullerene use as antiwear additives. Although fullerenes did not significantly change antifrictional properties of the base lubricant, they improve wear resistance of surfaces and have a strong advantage over already known antiwear additives such as graphite powder or dithiophosphoric acid zinc salts – fullerene are soluble in oil. This advantage is a result of fullerene ability to be dissolved in mineral oils.

The present study brings out many issues, which would be interesting to cover in the future studies. These issues include:

- Study of the performance of fullerene containing lubricants under boundary lubrication conditions with normal loads below elastic limit of the materials in contact. It will help to evaluate the behavior of fullerenes when they are not partially or fully pressed in the contact bodies.

- Investigation of the changes in the chemical and physical properties of fullerene containing lubricants when the lubricants are exposed to high temperature spark due to a long operation time under boundary lubrication conditions. This study will allow to get a comprehensive picture of oxidation abilities of fullerene containing lubricants.

- Study of the use of fullerenes as additives for solid lubricants or greases and the base for surface coatings. This study is interested from the point of view of the universality of fullerenes in various tribological applications.

APPENDIX A

SURFACE TEXTURE PARAMETERS

Although surface texture analysis presented in this work includes evaluation of only major parameters such as average roughness R_a, mean roughness depth R_z and skewness R_{sk}, detailed description of all parameters, from which these parameters were taken, gives a comprehensive picture of the surfaces in hand. This chapter provides the description of all parameters, which can be evaluated by Perthometer PGK.

A.1 Description of Surface Texture Parameters

Settings:

LC – Cutoff

LT – Traversing Length

LM – Evaluating Length

Z – Number of sampling lengths

VB – Measuring range

LY – Width (Y) of topography

NY – Number of topography profiles

NX – Number of profile points

dX – Point spacing in profile

VT – Measuring speed

Roughness Parameters:

[CREF (R)] [5.00 %] – Specify percentage reference line

[C (R)] [-1.00 mum] – Specify absolute intersection line

[C-MR (R) [10.00 %] – Specify intersection line for zone width

[C1 (R)] [0.50 %] – Specify upper intersection line

[C1 (R)] –0.50 %] – Specify lower intersection line

LC-R – Cutoff (roughness)

Ra – Roughness average

R max – Maximum roughness depth

Rz – Mean roughness depth

Rz max – Maximum single roughness depth

Rz-L – List of roughness depths

Rq – Root mean square roughness

Rp – Mean profile peak height

Rp max – Maximum profile peak height

Rp-L – List of profile heights

Rt – Roughness depth

R3z – Base roughness depth

R3z max – Maximum roughness depth

R3z-L – List of roughness depths

R Sm – Mean width of profile elements

R S – Mean spacing of local profile peaks

R Pc [<C1>; <C2>] – Peak count of the R-profile

R HSC [<C1>] – Peak count of the R-profile

R Mr [<C>; <CREF>] – Material ratio of the R-profile

R Mr-L [-1.00 mum; <CREF>] – Material ration list of the R-profile

R M% [<C-MR>; <CREF>] – Zone width of two material ratios

R M%-L [10.00 %; <CREF>] – Zone width list

R Sk – Skewness of the R-profile

R Ku – Kurtosis of the R-profile

Further Roughness Parameters:

Rv – Mean profile valley depth

Rv-L – List of profile valleys depths

Rdq – RMS slope of the profile depth

Core Roughness Parameters:

Rk – Core roughness depth

Rpk – Reduced peak height

Rvk – Reduced valley depth

MR1 – Material ration of peaks

MR2 – Material ratio of valleys

A1 – Material filled profile peak area

A2 – Lubricant filled profile valley area

CNOMO Parameters:

[A] [0.50 mm] – Specify operator for roughness motifs

[B] [2.50 mm] – Specify operator for waviness motifs

R – Mean depth of roughness motifs

AR – Mean spacing of roughness motifs

W – Mean depth of waviness motifs

AW – Mean spacing of waviness motifs

Rx – Maximum depth of profile irregularity

Wx – Maximum depth of waviness

Wte – Total depth of waviness

CMP – NCRX/NR (combination factor)

Core Roughness (Re-profile):

[Rke-A] [0.50 mm] – Specify operator for roughness motifs

[Rke-B] [2.50 mm] – Specify operator for waviness motifs

Rke – Core roughness depth (Re-profile)

Rpke – Reduced peak height (Re-profile)

Rvke – Reduced valley depth (Re-profile)

Rpkxe – Full peak height (Re-profile)

Rvkxe – Full valley depth (Re-profile)

Waviness Parameters:

LC-W – Cutoff (waviness)

Wt – Waviness height

Wa – Arithmetic mean deviation of the W-profile

P-Profile Parameters:

Pt – Profile depth

Pa – Arithmetic mean deviation of the P-profile

D-Profile Parameters:

Incl – Inclination of the D-profile

A.2 Analysis of Surface Profiles of Tested Materials for Series 1

This chapter illustrates the detailed analysis of typical steel roller and bronze shoe surfaces for experimental Series 1.

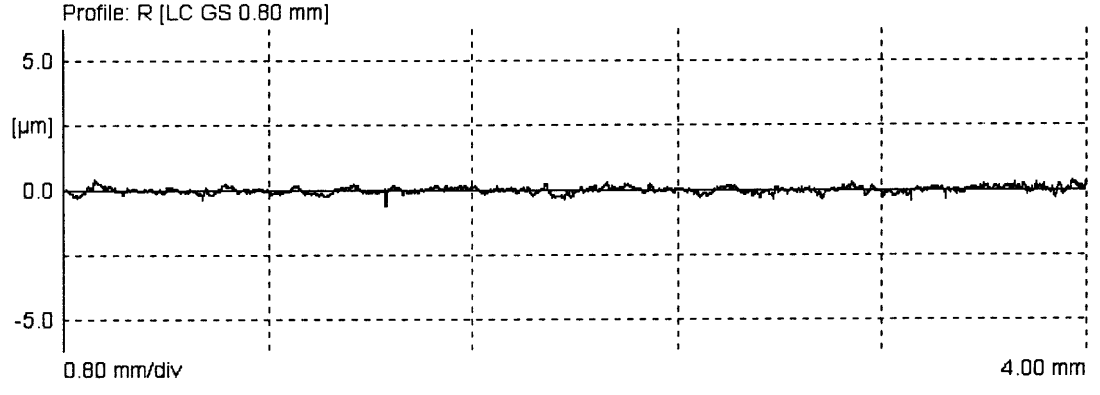

Figure A.1 Roughness profile for bronze SAE 40 shoe in Series 1.

General Parameters		
LC (GS)	0.25	mm
LT	5.60	mm
LM	4.00	mm
Z	5	
VB	±250	µm
LY	0.00	mm
NY	1	
NX	11200	
dX	0.50	µm
VT	0.50	mm/s
Rv	0.44	µm
Rv1	0.39	µm
Rv2	0.64	µm
Rv3	0.38	µm
Rv4	0.40	µm
Rv5	0.41	µm
Rv sigma	0.10	µm
Rdq	0.032	
Rk	0.32	µm
Rpk	0.09	µm
Rvk	0.15	µm
MR1	8.14	%
MR2	88.99	%
A1	0.00	µm²/mm
A2	0.01	µm²/mm
[A]	0.50	mm
[B]	2.50	mm
R	0.43	µm
AR	106.5	µm
W	0.95	µm
AW	1346.6	µm
Rx	2.56	µm
Wx	3.22	µm
Wte	4.33	µm
CMP	3.75	
[Rke-A]	0.50	mm
[Rke-B]	2.50	mm
Rke	0.32	µm
Rpke	0.06	µm
Rvke	0.38	µm
Rpkxe	0.15	µm
Rvkxe	2.09	µm
LC-W (GS)	0.80	mm
Pt	4.73	µm
Pa	0.99	µm
Incl	-0.06	µm/mm

Roughness Parameters		
[CREF (R)]	5.00	%
[C (R)]	-1.00	µm
[C-MR (R)]	10.00	%
[C1 (R)]	0.50	µm
[C2 (R)]	-0.50	µm
LC-R (GS)	0.14	mm
Ra	0.06	µm
Rmax	0.76	µm
Rz	0.59	µm
Rz max	0.76	µm
Rz1	0.52	µm
Rz2	0.76	µm
Rz3	0.47	µm
Rz4	0.53	µm
Rz5	0.66	µm
Rz sigma	0.11	µm
Rq	0.08	µm
Rp	0.23	µm
Rp max	0.29	µm
Rp1	0.24	µm
Rp2	0.16	µm
Rp3	0.29	µm
Rp4	0.21	µm
Rp5	0.28	µm
Rp sigma	0.05	µm
Rt	0.88	µm
R3z	0.38	µm
R3z max	0.50	µm
R3z1	0.33	µm
R3z2	0.30	µm
R3z3	0.37	µm
R3z4	0.40	µm
R3z5	0.50	µm
R3z sigma	0.07	µm
R Sm	---	µm
R S	26.81	µm
R Pc (0.50,-0.50)	0	/cm
R HSC (0.50)	0	/cm
R Mr (-1.00/5.00)	100.0	%
R Mr (0.17/5.00)	0.0	%
R Mr (0.00/5.00)	5.0	%
R Mr (-0.71/5.00)	100.0	%
R M% (10.00/5.00)	-0.03	µm
R M% (0.00/5.00)	0.17	µm
R M% (10.00/5.00)	-0.03	µm
R M% (20.00/5.00)	-0.06	µm
R M% (30.00/5.00)	-0.08	µm
R M% (40.00/5.00)	-0.10	µm
R M% (50.00/5.00)	-0.11	µm
R M% (60.00/5.00)	-0.13	µm
R M% (70.00/5.00)	-0.15	µm
R M% (80.00/5.00)	-0.18	µm
R M% (90.00/5.00)	-0.21	µm
R M% (100.00/5.00)	-0.71	µm
R Sk	-0.36	
R Ku	6.21	

Figure A.2 Surface parameter field for bronze SAE 40 shoe in Series 1.

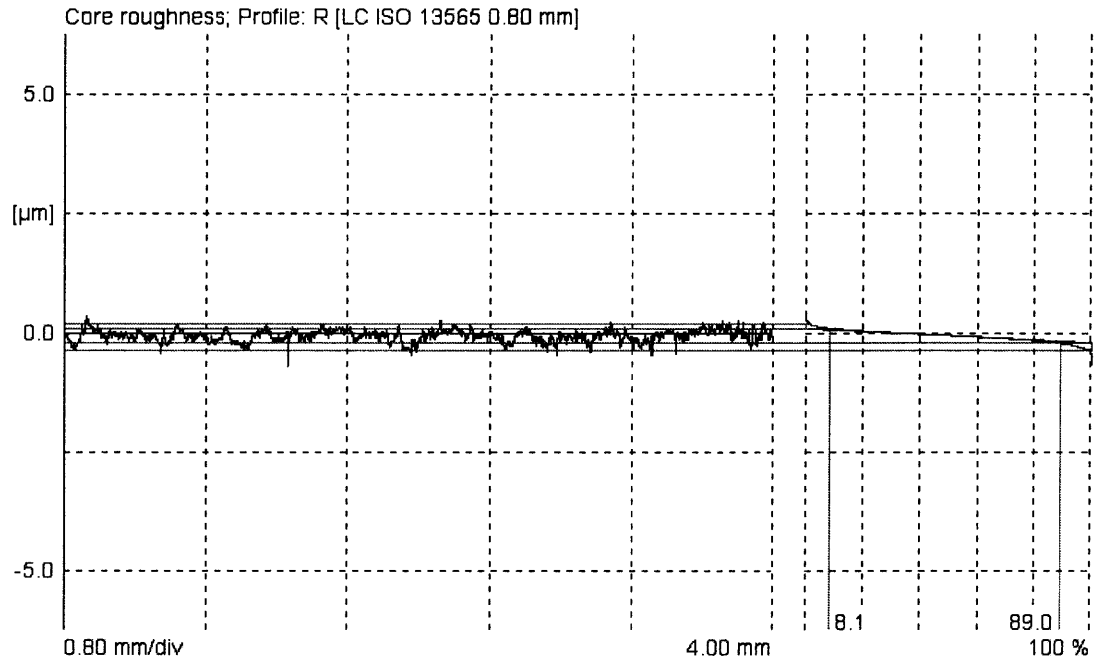

Figure A.3 Material ratio profile for bronze SAE 40 shoe in Series 1.

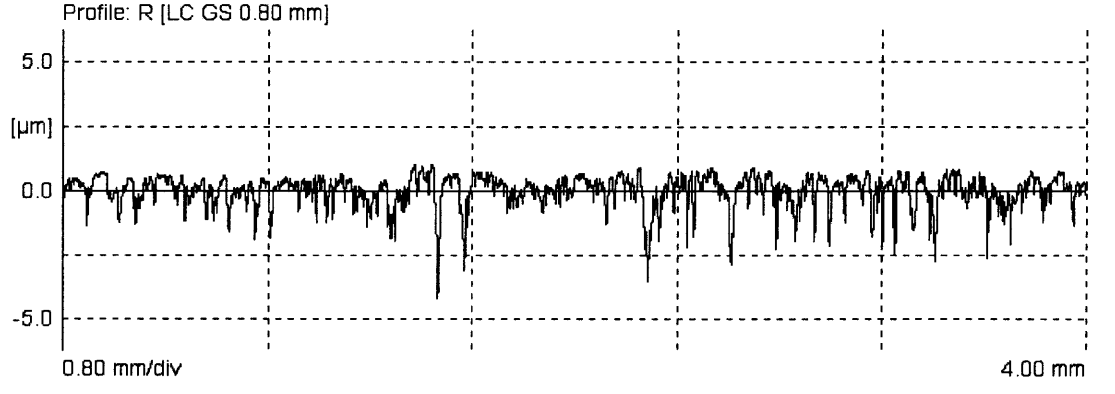

Figure A.4 Roughness profile for steel AISI 4340 roller in Series 1.

General Parameters		
LC (GS)	0.25	mm
LT	5.60	mm
LM	4.00	mm
Z	5	
VB	±250	µm
LY	0.00	mm
NY	1	
NX	11200	
dX	0.50	µm
VT	0.50	mm/s
Rv	3.05	µm
Rv1	1.91	µm
Rv2	4.19	µm
Rv3	3.53	µm
Rv4	2.85	µm
Rv5	2.77	µm
Rv sigma	0.77	µm
Rdq	0.175	
Rk	1.10	µm
Rpk	0.12	µm
Rvk	1.33	µm
MR1	3.30	%
MR2	81.06	%
A1	0.00	µm²/mm
A2	0.13	µm²/mm
[A]	0.50	mm
[B]	2.50	mm
R	1.86	µm
AR	85.5	µm
W	0.86	µm
AW	889.4	µm
Rx	5.16	µm
Wx	2.48	µm
Wte	4.96	µm
CMP	3.95	
[Rke-A]	0.50	mm
[Rke-B]	2.50	mm
Rke	0.84	µm
Rpke	0.15	µm
Rvke	1.23	µm
Rpkxe	0.20	µm
Rvkxe	4.33	µm
LC-W (GS)	0.80	mm
Pt	6.88	µm
Pa	1.06	µm
Incl	0.26	µm/mm

Roughness Parameters		
[CREF (R)]	5.00	%
[C (R)]	-1.00	µm
[C-MR (R)]	10.00	%
[C1 (R)]	0.50	µm
[C2 (R)]	-0.50	µm
LC-R (GS)	0.14	mm
Ra	0.37	µm
Rmax	4.95	µm
Rz	3.52	µm
Rz max	4.95	µm
Rz1	2.40	µm
Rz2	4.95	µm
Rz3	3.74	µm
Rz4	3.07	µm
Rz5	3.43	µm
Rz sigma	0.84	µm
Rq	0.52	µm
Rp	0.96	µm
Rp max	1.27	µm
Rp1	0.72	µm
Rp2	1.15	µm
Rp3	1.27	µm
Rp4	0.79	µm
Rp5	0.88	µm
Rp sigma	0.21	µm
Rt	5.07	µm
R3z	2.49	µm
R3z max	3.04	µm
R3z1	2.00	µm
R3z2	2.48	µm
R3z3	1.93	µm
R3z4	3.00	µm
R3z5	3.04	µm
R3z sigma	0.47	µm
R Sm	---	µm
R S	30.56	µm
R Pc (0.50,-0.50)	85	/cm
R HSC (0.50)	115	/cm
R Mr (-1.00/5.00)	85.0	%
R Mr (0.60/5.00)	0.0	%
R Mr (0.00/5.00)	5.0	%
R Mr (-1.00/5.00)	85.0	%
R Mr (-2.00/5.00)	97.7	%
R Mr (-3.00/5.00)	99.7	%
R Mr (-4.00/5.00)	99.9	%
R Mr (-4.38/5.00)	100.0	%
R M% (10.00/5.00)	-0.10	µm
R M% (0.00/5.00)	0.68	µm
R M% (10.00/5.00)	-0.10	µm
R M% (20.00/5.00)	-0.22	µm
R M% (30.00/5.00)	-0.30	µm
R M% (40.00/5.00)	-0.38	µm
R M% (50.00/5.00)	-0.45	µm
R M% (60.00/5.00)	-0.56	µm
R M% (70.00/5.00)	-0.69	µm
R M% (80.00/5.00)	-0.87	µm
R M% (90.00/5.00)	-1.20	µm
R M% (100.00/5.00)	-4.38	µm
R Sk	-1.84	
R Ku	6.70	

Figure A.5 Surface parameter field for bronze SAE 40 shoe in Series 1.

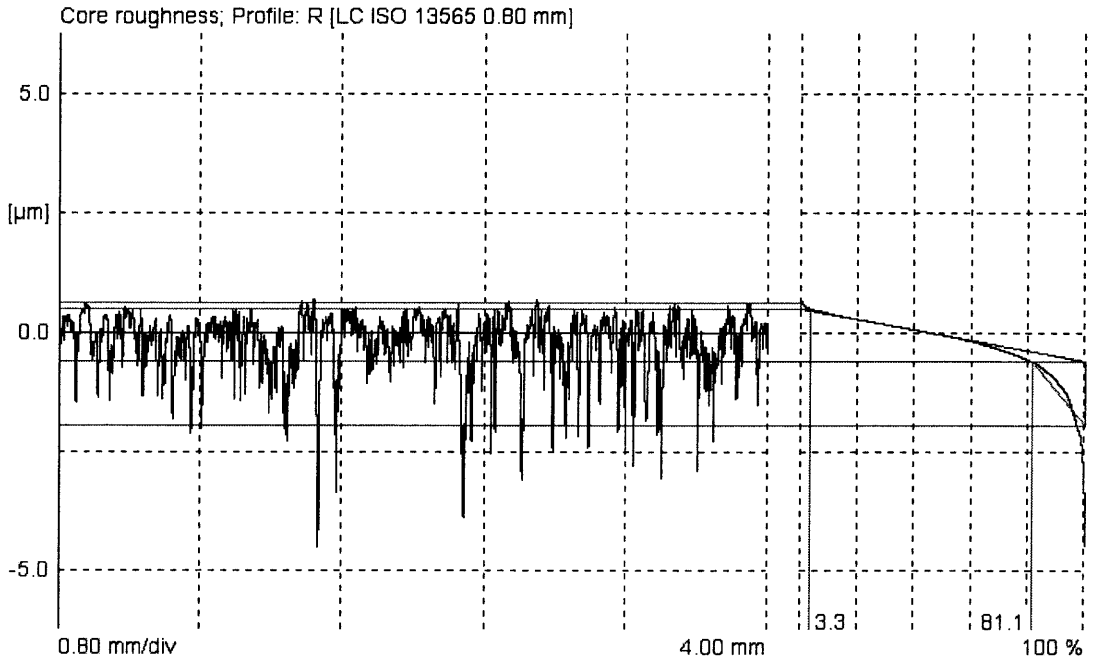

Figure A.6 Material ratio profile for bronze SAE 40 shoe in Series 1.

A.3 Analysis of Surface Profiles of Tested Materials for Series 2

This chapter shows the detailed analysis of a typical steel roller surface for experimental Series 1.

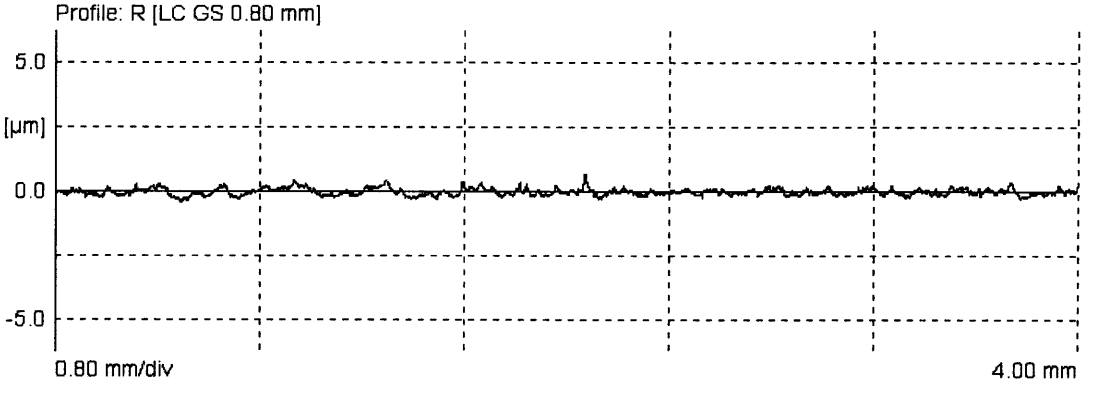

Figure A.7 Roughness profile for steel AISI 4340 roller in Series 2.

General Parameters		
LC (GS)	0.25	mm
LT	5.60	mm
LM	4.00	mm
Z	5	
VB	±250	µm
LY	0.00	mm
NY	1	
NX	11200	
dX	0.50	µm
VT	0.50	mm/s
Rv	2.57	µm
Rv1	3.74	µm
Rv2	1.64	µm
Rv3	2.15	µm
Rv4	3.12	µm
Rv5	2.19	µm
Rv sigma	0.76	µm
Rdq	0.137	
Rk	0.81	µm
Rpk	0.15	µm
Rvk	1.03	µm
MR1	3.62	%
MR2	79.24	%
A1	0.00	µm²/mm
A2	0.11	µm²/mm
[A]	0.50	mm
[B]	2.50	mm
R	1.53	µm
AR	75.0	µm
W	0.95	µm
AW	747.4	µm
Rx	5.26	µm
Wx	5.91	µm
Wte	5.91	µm
CMP	2.92	
[Rke-A]	0.50	mm
[Rke-B]	2.50	mm
Rke	0.71	µm
Rpke	0.25	µm
Rvke	0.97	µm
Rpkxe	0.44	µm
Rvkxe	3.67	µm
LC-W (GS)	0.80	mm
Pt	8.39	µm
Pa	1.41	µm
Incl	0.15	µm/mm

Roughness Parameters		
[CREF (R)]	5.00	%
[C (R)]	-1.00	µm
[C-MR (R)]	10.00	%
[C1 (R)]	0.50	µm
[C2 (R)]	-0.50	µm
LC-R (GS)	0.14	mm
Ra	0.28	µm
Rmax	4.00	µm
Rz	2.91	µm
Rz max	4.00	µm
Rz1	4.00	µm
Rz2	1.81	µm
Rz3	2.52	µm
Rz4	3.67	µm
Rz5	2.55	µm
Rz sigma	0.81	µm
Rq	0.40	µm
Rp	0.67	µm
Rp max	0.91	µm
Rp1	0.91	µm
Rp2	0.49	µm
Rp3	0.51	µm
Rp4	0.71	µm
Rp5	0.72	µm
Rp sigma	0.15	µm
Rt	4.00	µm
R3z	1.96	µm
R3z max	2.26	µm
R3z1	2.19	µm
R3z2	1.56	µm
R3z3	1.99	µm
R3z4	2.26	µm
R3z5	1.80	µm
R3z sigma	0.26	µm
R Sm	---	µm
R S	34.64	µm
R Pc (0.50,-0.50)	45	/cm
R HSC (0.50)	47	/cm
R Mr (-1.00/5.00)	91.8	%
R Mr (0.46/5.00)	0.0	%
R Mr (0.00/5.00)	5.0	%
R Mr (-1.00/5.00)	91.8	%
R Mr (-2.00/5.00)	99.2	%
R Mr (-3.00/5.00)	99.8	%
R Mr (-3.53/5.00)	100.0	%
R M% (10.00/5.00)	-0.09	µm
R M% (0.00/5.00)	0.46	µm
R M% (10.00/5.00)	-0.09	µm
R M% (20.00/5.00)	-0.17	µm
R M% (30.00/5.00)	-0.23	µm
R M% (40.00/5.00)	-0.29	µm
R M% (50.00/5.00)	-0.34	µm
R M% (60.00/5.00)	-0.42	µm
R M% (70.00/5.00)	-0.52	µm
R M% (80.00/5.00)	-0.67	µm
R M% (90.00/5.00)	-0.93	µm
R M% (100.00/5.00)	-3.53	µm
R Sk	-2.04	
R Ku	10.66	

Figure A.8 Surface parameter field for steel AISI 4340 roller in Series 2.

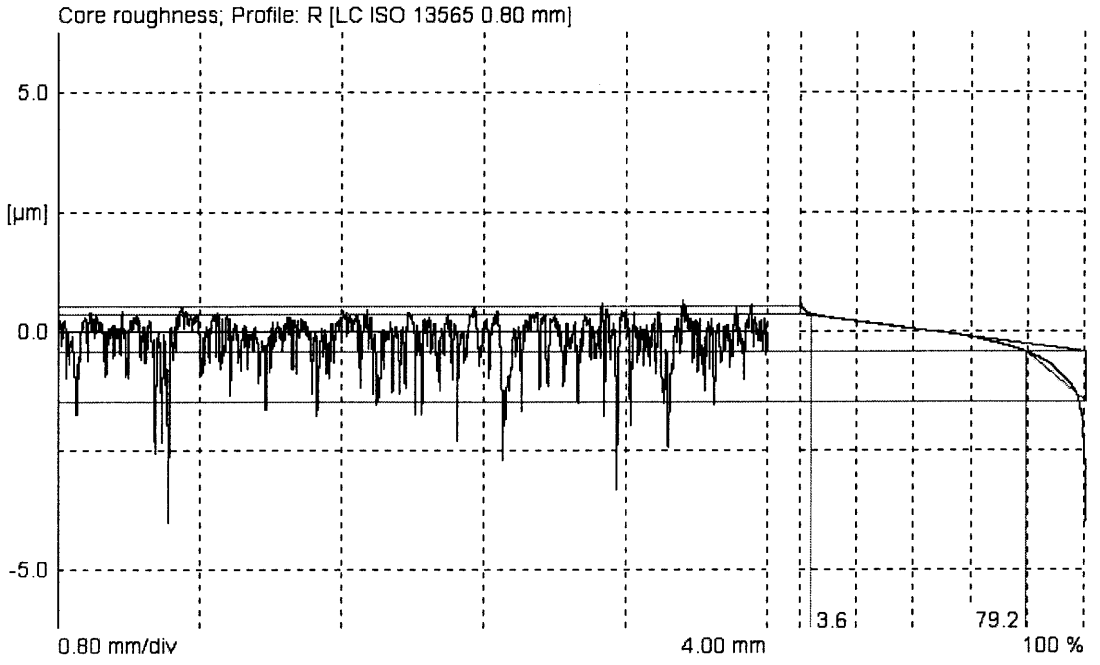

Figure A.9 Material ratio profile for bronze SAE 40 shoe in Series 2.

APPENDIX B

VISUAL C++ APPLICATION

Visual C++ program was developed and installed to control digital linear gage. The tasks of this program are sending 1-bit signal with specified frequency, receiving back signal from digital linear gage, synchronizing obtained signal with timer and saving all obtained information to file. Description of this program is divided by Source and Header files which are listed in Sections B.1 and B.2, respectively.

B.1 Source Files

ChildFrm.cpp

```
// ChildFrm.cpp : implementation of the CChildFrame class
//
#include "stdafx.h"
#include "ComTest.h"
#include "ChildFrm.h"
#ifdef _DEBUG
#define new DEBUG_NEW
#undef THIS_FILE
static char THIS_FILE[] = __FILE__;
#endif
/////////////////////////////////////////////////////////////////////////////
// CChildFrame
IMPLEMENT_DYNCREATE(CChildFrame, CMDIChildWnd)
BEGIN_MESSAGE_MAP(CChildFrame, CMDIChildWnd)
        //{{AFX_MSG_MAP(CChildFrame)
                // NOTE - the ClassWizard will add and remove mapping macros here.
                //    DO NOT EDIT what you see in these blocks of generated code !
        //}}AFX_MSG_MAP
END_MESSAGE_MAP()
/////////////////////////////////////////////////////////////////////////////
// CChildFrame construction/destruction
CChildFrame::CChildFrame()
{
        // TODO: add member initialization code here

}
CChildFrame::~CChildFrame()
{
}
```

```
BOOL CChildFrame::PreCreateWindow(CREATESTRUCT& cs)
{
	// TODO: Modify the Window class or styles here by modifying
	//  the CREATESTRUCT cs
	if( !CMDIChildWnd::PreCreateWindow(cs) )
		return FALSE;
	return TRUE;
}
/////////////////////////////////////////////////////////////////////////////
// CChildFrame diagnostics
#ifdef _DEBUG
void CChildFrame::AssertValid() const
{
	CMDIChildWnd::AssertValid();
}
void CChildFrame::Dump(CDumpContext& dc) const
{
	CMDIChildWnd::Dump(dc);
}
#endif //_DEBUG
/////////////////////////////////////////////////////////////////////////////
// CChildFrame message handlers
```

ComTest.cpp

```
// ComTest.cpp : Defines the class behaviors for the application.
//
#include "stdafx.h"
#include "ComTest.h"
#include "MainFrm.h"
#include "ChildFrm.h"
#include "ComTestDoc.h"
#include "ComTestView.h"
#ifdef _DEBUG
#define new DEBUG_NEW
#undef THIS_FILE
static char THIS_FILE[] = __FILE__;
#endif
/////////////////////////////////////////////////////////////////////////////
// CComTestApp
BEGIN_MESSAGE_MAP(CComTestApp, CWinApp)
	//{{AFX_MSG_MAP(CComTestApp)
	ON_COMMAND(ID_APP_ABOUT, OnAppAbout)
		// NOTE - the ClassWizard will add and remove mapping macros here.
		//    DO NOT EDIT what you see in these blocks of generated code!
	//}}AFX_MSG_MAP
	// Standard file based document commands
	ON_COMMAND(ID_FILE_NEW, CWinApp::OnFileNew)
	ON_COMMAND(ID_FILE_OPEN, CWinApp::OnFileOpen)
	// Standard print setup command
	ON_COMMAND(ID_FILE_PRINT_SETUP, CWinApp::OnFilePrintSetup)
END_MESSAGE_MAP()
/////////////////////////////////////////////////////////////////////////////
// CComTestApp construction
```

```
CComTestApp::CComTestApp()
{
	// TODO: add construction code here,
	// Place all significant initialization in InitInstance
}
/////////////////////////////////////////////////////////////////////////////
// The one and only CComTestApp object
CComTestApp theApp;
/////////////////////////////////////////////////////////////////////////////
// CComTestApp initialization
BOOL CComTestApp::InitInstance()
{
	AfxEnableControlContainer();
	// Standard initialization
	// If you are not using these features and wish to reduce the size
	//  of your final executable, you should remove from the following
	//  the specific initialization routines you do not need.
#ifdef _AFXDLL
	Enable3dControls();			// Call this when using MFC in a shared DLL
#else
	Enable3dControlsStatic(); // Call this when linking to MFC statically
#endif
	// Change the registry key under which our settings are stored.
	// TODO: You should modify this string to be something appropriate
	// such as the name of your company or organization.
	SetRegistryKey(_T("Local AppWizard-Generated Applications"));
	LoadStdProfileSettings();  // Load standard INI file options (including MRU)
	// Register the application's document templates.  Document templates
	//  serve as the connection between documents, frame windows and views.
	CMultiDocTemplate* pDocTemplate;
	pDocTemplate = new CMultiDocTemplate(
		IDR_COMTESTYPE,
		RUNTIME_CLASS(CComTestDoc),
		RUNTIME_CLASS(CChildFrame), // custom MDI child frame
		RUNTIME_CLASS(CComTestView));
	AddDocTemplate(pDocTemplate);
	// create main MDI Frame window
	CMainFrame* pMainFrame = new CMainFrame;
	if (!pMainFrame->LoadFrame(IDR_MAINFRAME))
		return FALSE;
	m_pMainWnd = pMainFrame;
	// Parse command line for standard shell commands, DDE, file open
	CCommandLineInfo cmdInfo;
	ParseCommandLine(cmdInfo);
	// Dispatch commands specified on the command line
	if (!ProcessShellCommand(cmdInfo))
		return FALSE;
	// The main window has been initialized, so show and update it.
	pMainFrame->ShowWindow(m_nCmdShow);
	pMainFrame->UpdateWindow();
	return TRUE;
}
/////////////////////////////////////////////////////////////////////////////
// CAboutDlg dialog used for App About
class CAboutDlg : public CDialog
{
```

```
public:
        CAboutDlg();
// Dialog Data
        //{{AFX_DATA(CAboutDlg)
        enum { IDD = IDD_ABOUTBOX };
        //}}AFX_DATA
        // ClassWizard generated virtual function overrides
        //{{AFX_VIRTUAL(CAboutDlg)
        protected:
        virtual void DoDataExchange(CDataExchange* pDX);    // DDX/DDV support
        //}}AFX_VIRTUAL
// Implementation
protected:
        //{{AFX_MSG(CAboutDlg)
                // No message handlers
        //}}AFX_MSG
        DECLARE_MESSAGE_MAP()
};
CAboutDlg::CAboutDlg() : CDialog(CAboutDlg::IDD)
{
        //{{AFX_DATA_INIT(CAboutDlg)
        //}}AFX_DATA_INIT
}
void CAboutDlg::DoDataExchange(CDataExchange* pDX)
{
        CDialog::DoDataExchange(pDX);
        //{{AFX_DATA_MAP(CAboutDlg)
        //}}AFX_DATA_MAP
}
BEGIN_MESSAGE_MAP(CAboutDlg, CDialog)
        //{{AFX_MSG_MAP(CAboutDlg)
                // No message handlers
        //}}AFX_MSG_MAP
END_MESSAGE_MAP()
// App command to run the dialog
void CComTestApp::OnAppAbout()
{
        CAboutDlg aboutDlg;
        aboutDlg.DoModal();
}
/////////////////////////////////////////////////////////////////////////////
// CComTestApp message handlers
```

ComTestDoc.cpp

```
// ComTestDoc.cpp : implementation of the CComTestDoc class
//
#include "stdafx.h"
#include "ComTest.h"
#include <string.h>
#include "ComTestDoc.h"
#include "MyFileDlg.h"
#ifdef _DEBUG
#define new DEBUG_NEW
```

```
#undef THIS_FILE
static char THIS_FILE[] = __FILE__;
#endif
#define OUT_DATA_SIZE 13
//////////////////////////////////////////////////////////////////////////
// CComTestDoc
IMPLEMENT_DYNCREATE(CComTestDoc, CDocument)
BEGIN_MESSAGE_MAP(CComTestDoc, CDocument)
	//{{AFX_MSG_MAP(CComTestDoc)
		// NOTE - the ClassWizard will add and remove mapping macros here.
		//    DO NOT EDIT what you see in these blocks of generated code!
	//}}AFX_MSG_MAP
END_MESSAGE_MAP()
//////////////////////////////////////////////////////////////////////////
// CComTestDoc construction/destruction
CComTestDoc::CComTestDoc()
{
	// TODO: add one-time construction code here
	strcpy(m_pComData, "1");
	m_nByteCnt = 1;
	m_sec = 0;
}
CComTestDoc::~CComTestDoc()
{
}
BOOL CComTestDoc::OnNewDocument()
{
	if (!CDocument::OnNewDocument())
		return FALSE;
	// TODO: add reinitialization code here
	// (SDI documents will reuse this document)
	DCB dcb;
	BOOL fSuccess;
	hCom = CreateFile( "COM1",
		GENERIC_READ | GENERIC_WRITE,
		0,    // comm devices must be opened w/exclusive-access
		NULL, // no security attributes
		OPEN_EXISTING, // comm devices must use OPEN_EXISTING
		0,    // not overlapped I/O
		NULL  // hTemplate must be NULL for comm devices
		);
	if (hCom == INVALID_HANDLE_VALUE)
		return FALSE;
	fSuccess = GetCommState(hCom, &dcb);
	if (!fSuccess)
		return FALSE;
	// Fill in the DCB: baud=2400, 8 data bits, no parity, 1 stop bit.
	dcb.BaudRate = 2400;
	dcb.ByteSize = 8;
	dcb.Parity = NOPARITY;
	dcb.StopBits = ONESTOPBIT;
	fSuccess = SetCommState(hCom, &dcb);
	if (!fSuccess)
		return FALSE;
	CMyFileDlg dlg;
	dlg.m_filename = "data.xls";
```

```
        dlg.DoModal();
        m_out_file.open(dlg.m_filename);
        return TRUE;
}
////////////////////////////////////////////////////////////////////////////
// CComTestDoc serialization
void CComTestDoc::Serialize(CArchive& ar)
{
        if (ar.IsStoring())
        {
                // TODO: add storing code here
        }
        else
        {
                // TODO: add loading code here
        }
}
////////////////////////////////////////////////////////////////////////////
// CComTestDoc diagnostics
#ifdef _DEBUG
void CComTestDoc::AssertValid() const
{
        CDocument::AssertValid();
}
void CComTestDoc::Dump(CDumpContext& dc) const
{
        CDocument::Dump(dc);
}
#endif //_DEBUG
////////////////////////////////////////////////////////////////////////////
// CComTestDoc commands
void CComTestDoc::PutToCOM()
{
        if(!hCom)
                return;
        char buff[OUT_DATA_SIZE+1];
        DWORD nBytesWritten = 0;
        DWORD nBytesRead = 0;
        WriteFile(hCom, m_pComData, m_nByteCnt, &nBytesWritten, NULL);
        ReadFile(hCom, buff, OUT_DATA_SIZE, &nBytesRead, NULL);
        buff[nBytesRead]='\0';
        m_out_file << ++m_sec << '\t' << (char*)(buff+3);
}
void CComTestDoc::OnCloseDocument()
{
        // TODO: Add your specialized code here and/or call the base class
        CloseHandle(hCom);
        m_out_file.close();
        CDocument::OnCloseDocument();
}
```

ComTestView.cpp

```
// ComTestView.cpp : implementation of the CComTestView class
```

```
//
#include "stdafx.h"
#include "ComTest.h"
#include "ComTestDoc.h"
#include "ComTestView.h"
#ifdef _DEBUG
#define new DEBUG_NEW
#undef THIS_FILE
static char THIS_FILE[] = __FILE__;
#endif
/////////////////////////////////////////////////////////////////////////////
// CComTestView
IMPLEMENT_DYNCREATE(CComTestView, CView)
BEGIN_MESSAGE_MAP(CComTestView, CView)
        //{{AFX_MSG_MAP(CComTestView)
        ON_COMMAND(MY_COM_BEGIN, OnComBegin)
        ON_COMMAND(MY_COM_STOP, OnComStop)
        ON_WM_TIMER()
        //}}AFX_MSG_MAP
        // Standard printing commands
        ON_COMMAND(ID_FILE_PRINT, CView::OnFilePrint)
        ON_COMMAND(ID_FILE_PRINT_DIRECT, CView::OnFilePrint)
        ON_COMMAND(ID_FILE_PRINT_PREVIEW, CView::OnFilePrintPreview)
END_MESSAGE_MAP()
/////////////////////////////////////////////////////////////////////////////
// CComTestView construction/destruction
CComTestView::CComTestView()
{
        // TODO: add construction code here
}
CComTestView::~CComTestView()
{
}
BOOL CComTestView::PreCreateWindow(CREATESTRUCT& cs)
{
        // TODO: Modify the Window class or styles here by modifying
        //  the CREATESTRUCT cs
        return CView::PreCreateWindow(cs);
}
/////////////////////////////////////////////////////////////////////////////
// CComTestView drawing
void CComTestView::OnDraw(CDC* pDC)
{
        CComTestDoc* pDoc = GetDocument();
        ASSERT_VALID(pDoc);
        // TODO: add draw code for native data here
}
/////////////////////////////////////////////////////////////////////////////
// CComTestView printing
BOOL CComTestView::OnPreparePrinting(CPrintInfo* pInfo)
{
        // default preparation
        return DoPreparePrinting(pInfo);
}
void CComTestView::OnBeginPrinting(CDC* /*pDC*/, CPrintInfo* /*pInfo*/)
{
```

```
	// TODO: add extra initialization before printing
}
void CComTestView::OnEndPrinting(CDC* /*pDC*/, CPrintInfo* /*pInfo*/)
{
	// TODO: add cleanup after printing
}
/////////////////////////////////////////////////////////////////////////////
// CComTestView diagnostics
#ifdef _DEBUG
void CComTestView::AssertValid() const
{
	CView::AssertValid();
}
void CComTestView::Dump(CDumpContext& dc) const
{
	CView::Dump(dc);
}
CComTestDoc* CComTestView::GetDocument() // non-debug version is inline
{
	ASSERT(m_pDocument->IsKindOf(RUNTIME_CLASS(CComTestDoc)));
	return (CComTestDoc*)m_pDocument;
}
#endif //_DEBUG
/////////////////////////////////////////////////////////////////////////////
// CComTestView message handlers
void CComTestView::OnComBegin()
{
	// TODO: Add your command handler code here
	GetDocument()->ResetSec();
	m_timer = SetTimer(1, 1000, NULL);
}
void CComTestView::OnComStop()
{
	// TODO: Add your command handler code here
	KillTimer(m_timer);
}
void CComTestView::OnTimer(UINT nIDEvent)
{
	// TODO: Add your message handler code here and/or call default
	CView::OnTimer(nIDEvent);
	CComTestDoc* pDoc = GetDocument();
	pDoc->PutToCOM();
}
```

MainFrm.cpp

```
// MainFrm.cpp : implementation of the CMainFrame class
//
#include "stdafx.h"
#include "ComTest.h"
#include "MainFrm.h"
#ifdef _DEBUG
#define new DEBUG_NEW
#undef THIS_FILE
```

```
static char THIS_FILE[] = __FILE__;
#endif
/////////////////////////////////////////////////////////////////////////////
// CMainFrame
IMPLEMENT_DYNAMIC(CMainFrame, CMDIFrameWnd)
BEGIN_MESSAGE_MAP(CMainFrame, CMDIFrameWnd)
        //{{AFX_MSG_MAP(CMainFrame)
                // NOTE - the ClassWizard will add and remove mapping macros here.
                //    DO NOT EDIT what you see in these blocks of generated code !
        ON_WM_CREATE()
        //}}AFX_MSG_MAP
END_MESSAGE_MAP()
static UINT indicators[] =
{
        ID_SEPARATOR,           // status line indicator
        ID_INDICATOR_CAPS,
        ID_INDICATOR_NUM,
        ID_INDICATOR_SCRL,
};
/////////////////////////////////////////////////////////////////////////////
// CMainFrame construction/destruction
CMainFrame::CMainFrame()
{
        // TODO: add member initialization code here

}
CMainFrame::~CMainFrame()
{
}
int CMainFrame::OnCreate(LPCREATESTRUCT lpCreateStruct)
{
        if (CMDIFrameWnd::OnCreate(lpCreateStruct) == -1)
                return -1;

        if (!m_wndToolBar.CreateEx(this, TBSTYLE_FLAT, WS_CHILD | WS_VISIBLE | CBRS_TOP
                | CBRS_GRIPPER | CBRS_TOOLTIPS | CBRS_FLYBY | CBRS_SIZE_DYNAMIC) ||
                !m_wndToolBar.LoadToolBar(IDR_MAINFRAME))
        {
                TRACE0("Failed to create toolbar\n");
                return -1;      // fail to create
        }
        if (!m_wndStatusBar.Create(this) ||
                !m_wndStatusBar.SetIndicators(indicators,
                  sizeof(indicators)/sizeof(UINT)))
        {
                TRACE0("Failed to create status bar\n");
                return -1;      // fail to create
        }
        // TODO: Delete these three lines if you don't want the toolbar to
        //  be dockable
        m_wndToolBar.EnableDocking(CBRS_ALIGN_ANY);
        EnableDocking(CBRS_ALIGN_ANY);
        DockControlBar(&m_wndToolBar);
        return 0;
}
BOOL CMainFrame::PreCreateWindow(CREATESTRUCT& cs)
```

```
{
        if( !CMDIFrameWnd::PreCreateWindow(cs) )
                return FALSE;
        // TODO: Modify the Window class or styles here by modifying
        //  the CREATESTRUCT cs
        return TRUE;
}
/////////////////////////////////////////////////////////////////////////////
// CMainFrame diagnostics
#ifdef _DEBUG
void CMainFrame::AssertValid() const
{
        CMDIFrameWnd::AssertValid();
}
void CMainFrame::Dump(CDumpContext& dc) const
{
        CMDIFrameWnd::Dump(dc);
}
#endif //_DEBUG
/////////////////////////////////////////////////////////////////////////////
// CMainFrame message handlers
```

MyFileDlg.cpp

```
// MyFileDlg.cpp : implementation file
//
#include "stdafx.h"
#include "ComTest.h"
#include "MyFileDlg.h"
#ifdef _DEBUG
#define new DEBUG_NEW
#undef THIS_FILE
static char THIS_FILE[] = __FILE__;
#endif
/////////////////////////////////////////////////////////////////////////////
// CMyFileDlg dialog
CMyFileDlg::CMyFileDlg(CWnd* pParent /*=NULL*/)
        : CDialog(CMyFileDlg::IDD, pParent)
{
        //{{AFX_DATA_INIT(CMyFileDlg)
        m_filename = _T("");
        //}}AFX_DATA_INIT
}
void CMyFileDlg::DoDataExchange(CDataExchange* pDX)
{
        CDialog::DoDataExchange(pDX);
        //{{AFX_DATA_MAP(CMyFileDlg)
        DDX_Text(pDX, IDC_EDIT1, m_filename);
        //}}AFX_DATA_MAP
}
BEGIN_MESSAGE_MAP(CMyFileDlg, CDialog)
        //{{AFX_MSG_MAP(CMyFileDlg)
                // NOTE: the ClassWizard will add message map macros here
        //}}AFX_MSG_MAP
```

```
END_MESSAGE_MAP()
/////////////////////////////////////////////////////////////////////////////
// CMyFileDlg message handlers
```

StdAfx.cpp

```
// stdafx.cpp : source file that includes just the standard includes
//	ComTest.pch will be the pre-compiled header
//	stdafx.obj will contain the pre-compiled type information
#include "stdafx.h"
```

B.2 Header Files

ChildFrm.h

```
// ChildFrm.h : interface of the CChildFrame class
//
/////////////////////////////////////////////////////////////////////////////
#if !defined(AFX_CHILDFRM_H__8EFF1E01_9181_4CF6_AC92_4DF898EE08A7__INCLUDED_)
#define AFX_CHILDFRM_H__8EFF1E01_9181_4CF6_AC92_4DF898EE08A7__INCLUDED_
#if _MSC_VER > 1000
#pragma once
#endif // _MSC_VER > 1000
class CChildFrame : public CMDIChildWnd
{
	DECLARE_DYNCREATE(CChildFrame)
public:
	CChildFrame();
// Attributes
public:
// Operations
public:
// Overrides
	// ClassWizard generated virtual function overrides
	//{{AFX_VIRTUAL(CChildFrame)
	virtual BOOL PreCreateWindow(CREATESTRUCT& cs);
	//}}AFX_VIRTUAL
// Implementation
public:
	virtual ~CChildFrame();
#ifdef _DEBUG
	virtual void AssertValid() const;
	virtual void Dump(CDumpContext& dc) const;
#endif
// Generated message map functions
protected:
	//{{AFX_MSG(CChildFrame)
		// NOTE - the ClassWizard will add and remove member functions here.
		//    DO NOT EDIT what you see in these blocks of generated code!
	//}}AFX_MSG
	DECLARE_MESSAGE_MAP()
```

```
};
/////////////////////////////////////////////////////////////////////////////
//{{AFX_INSERT_LOCATION}}
// Microsoft Visual C++ will insert additional declarations immediately before the previous line.
#endif //
!defined(AFX_CHILDFRM_H__8EFF1E01_9181_4CF6_AC92_4DF898EE08A7__INCLUDED_)
```

ComTest.h

```
// ComTest.h : main header file for the COMTEST application
//
#if !defined(AFX_COMTEST_H__5F36C730_CCCA_469B_9D62_758A5394876D__INCLUDED_)
#define AFX_COMTEST_H__5F36C730_CCCA_469B_9D62_758A5394876D__INCLUDED_
#if _MSC_VER > 1000
#pragma once
#endif // _MSC_VER > 1000
#ifndef __AFXWIN_H__
        #error include 'stdafx.h' before including this file for PCH
#endif
#include "resource.h"       // main symbols
/////////////////////////////////////////////////////////////////////////////
// CComTestApp:
// See ComTest.cpp for the implementation of this class
//
class CComTestApp : public CWinApp
{
public:
        CComTestApp();
// Overrides
        // ClassWizard generated virtual function overrides
        //{{AFX_VIRTUAL(CComTestApp)
        public:
        virtual BOOL InitInstance();
        //}}AFX_VIRTUAL
// Implementation
        //{{AFX_MSG(CComTestApp)
        afx_msg void OnAppAbout();
                // NOTE - the ClassWizard will add and remove member functions here.
                //    DO NOT EDIT what you see in these blocks of generated code !
        //}}AFX_MSG
        DECLARE_MESSAGE_MAP()
};
/////////////////////////////////////////////////////////////////////////////
//{{AFX_INSERT_LOCATION}}
// Microsoft Visual C++ will insert additional declarations immediately before the previous line.
#endif //
!defined(AFX_COMTEST_H__5F36C730_CCCA_469B_9D62_758A5394876D__INCLUDED_)
```

ComTestDoc.h

```
// ComTestDoc.h : interface of the CComTestDoc class
//
```

```
////////////////////////////////////////////////////////////////////////
#if
!defined(AFX_COMTESTDOC_H__E27DF2A9_0A79_4327_BFEC_72377A6A3D54__INCLUDED_)
#define AFX_COMTESTDOC_H__E27DF2A9_0A79_4327_BFEC_72377A6A3D54__INCLUDED_
#if _MSC_VER > 1000
#pragma once
#endif // _MSC_VER > 1000
#include <list>
#include <fstream>
#define MAX_COM_DATA 32
class CComTestDoc : public CDocument
{
protected: // create from serialization only
        CComTestDoc();
        DECLARE_DYNCREATE(CComTestDoc)
// Attributes
public:
// Operations
public:
        void PutToCOM();
        void ResetSec(){m_sec=0;}
// Overrides
        // ClassWizard generated virtual function overrides
        //{{AFX_VIRTUAL(CComTestDoc)
        public:
        virtual BOOL OnNewDocument();
        virtual void Serialize(CArchive& ar);
        virtual void OnCloseDocument();
        //}}AFX_VIRTUAL
private:
        HANDLE hCom;
        char m_pComData[MAX_COM_DATA];
        DWORD m_nByteCnt;
        DWORD m_sec;
        std::ofstream m_out_file;
        std::list<char*> m_out_data;
// Implementation
public:
        virtual ~CComTestDoc();
#ifdef _DEBUG
        virtual void AssertValid() const;
        virtual void Dump(CDumpContext& dc) const;
#endif
protected:
// Generated message map functions
protected:
        //{{AFX_MSG(CComTestDoc)
                // NOTE - the ClassWizard will add and remove member functions here.
                //    DO NOT EDIT what you see in these blocks of generated code !
        //}}AFX_MSG
        DECLARE_MESSAGE_MAP()
};
////////////////////////////////////////////////////////////////////////
//{{AFX_INSERT_LOCATION}}
// Microsoft Visual C++ will insert additional declarations immediately before the previous line.
```

```
#endif //
!defined(AFX_COMTESTDOC_H__E27DF2A9_0A79_4327_BFEC_72377A6A3D54__INCLUDED_)
```

ComTestView.h

```
// ComTestView.h : interface of the CComTestView class
//
/////////////////////////////////////////////////////////////////////////////
#if
!defined(AFX_COMTESTVIEW_H__06152F9F_0C7B_4694_AC7F_4EB4D6D6AEC5__INCLUDED_)
#define AFX_COMTESTVIEW_H__06152F9F_0C7B_4694_AC7F_4EB4D6D6AEC5__INCLUDED_
#if _MSC_VER > 1000
#pragma once
#endif // _MSC_VER > 1000
class CComTestView : public CView
{
protected: // create from serialization only
        CComTestView();
        DECLARE_DYNCREATE(CComTestView)
// Attributes
public:
        CComTestDoc* GetDocument();
private:
        UINT m_timer;
// Operations
public:
// Overrides
        // ClassWizard generated virtual function overrides
        //{{AFX_VIRTUAL(CComTestView)
        public:
        virtual void OnDraw(CDC* pDC);  // overridden to draw this view
        virtual BOOL PreCreateWindow(CREATESTRUCT& cs);
        protected:
        virtual BOOL OnPreparePrinting(CPrintInfo* pInfo);
        virtual void OnBeginPrinting(CDC* pDC, CPrintInfo* pInfo);
        virtual void OnEndPrinting(CDC* pDC, CPrintInfo* pInfo);
        //}}AFX_VIRTUAL
// Implementation
public:
        virtual ~CComTestView();
#ifdef _DEBUG
        virtual void AssertValid() const;
        virtual void Dump(CDumpContext& dc) const;
#endif
protected:
// Generated message map functions
protected:
        //{{AFX_MSG(CComTestView)
        afx_msg void OnComBegin();
        afx_msg void OnComStop();
        afx_msg void OnTimer(UINT nIDEvent);
        //}}AFX_MSG
        DECLARE_MESSAGE_MAP()
};
```

```
#ifndef _DEBUG  // debug version in ComTestView.cpp
inline CComTestDoc* CComTestView::GetDocument()
   { return (CComTestDoc*)m_pDocument; }
#endif
/////////////////////////////////////////////////////////////////////////////
//{{AFX_INSERT_LOCATION}}
// Microsoft Visual C++ will insert additional declarations immediately before the previous line.
#endif //
!defined(AFX_COMTESTVIEW_H__06152F9F_0C7B_4694_AC7F_4EB4D6D6AEC5__INCLUDED_)
```

MainFrm.h

```
// MainFrm.h : interface of the CMainFrame class
//
/////////////////////////////////////////////////////////////////////////////
#if !defined(AFX_MAINFRM_H__0A90CE85_C788_4AE9_A608_107A43B34B20__INCLUDED_)
#define AFX_MAINFRM_H__0A90CE85_C788_4AE9_A608_107A43B34B20__INCLUDED_
#if _MSC_VER > 1000
#pragma once
#endif // _MSC_VER > 1000
class CMainFrame : public CMDIFrameWnd
{
        DECLARE_DYNAMIC(CMainFrame)
public:
        CMainFrame();
// Attributes
public:
// Operations
public:
// Overrides
        // ClassWizard generated virtual function overrides
        //{{AFX_VIRTUAL(CMainFrame)
        virtual BOOL PreCreateWindow(CREATESTRUCT& cs);
        //}}AFX_VIRTUAL
// Implementation
public:
        virtual ~CMainFrame();
#ifdef _DEBUG
        virtual void AssertValid() const;
        virtual void Dump(CDumpContext& dc) const;
#endif
protected:  // control bar embedded members
        CStatusBar  m_wndStatusBar;
        CToolBar    m_wndToolBar;
// Generated message map functions
protected:
        //{{AFX_MSG(CMainFrame)
        afx_msg int OnCreate(LPCREATESTRUCT lpCreateStruct);
                // NOTE - the ClassWizard will add and remove member functions here.
                //    DO NOT EDIT what you see in these blocks of generated code!
        //}}AFX_MSG
        DECLARE_MESSAGE_MAP()
};
/////////////////////////////////////////////////////////////////////////////
```

```
//{{AFX_INSERT_LOCATION}}
// Microsoft Visual C++ will insert additional declarations immediately before the previous line.
#endif //
!defined(AFX_MAINFRM_H__0A90CE85_C788_4AE9_A608_107A43B34B20__INCLUDED_)
```

MyFileDlg.h

```
#if !defined(AFX_MYFILEDLG_H__CD5C31AB_828B_48E0_A570_43302E9881BF__INCLUDED_)
#define AFX_MYFILEDLG_H__CD5C31AB_828B_48E0_A570_43302E9881BF__INCLUDED_
#if _MSC_VER > 1000
#pragma once
#endif // _MSC_VER > 1000
// MyFileDlg.h : header file
//
/////////////////////////////////////////////////////////////////////////////
// CMyFileDlg dialog
class CMyFileDlg : public CDialog
{
// Construction
public:
        CMyFileDlg(CWnd* pParent = NULL);   // standard constructor
// Dialog Data
        //{{AFX_DATA(CMyFileDlg)
        enum { IDD = IDD_FILENAME };
        CString  m_filename;
        //}}AFX_DATA
// Overrides
        // ClassWizard generated virtual function overrides
        //{{AFX_VIRTUAL(CMyFileDlg)
        protected:
        virtual void DoDataExchange(CDataExchange* pDX);    // DDX/DDV support
        //}}AFX_VIRTUAL
// Implementation
protected:
        // Generated message map functions
        //{{AFX_MSG(CMyFileDlg)
                // NOTE: the ClassWizard will add member functions here
        //}}AFX_MSG
        DECLARE_MESSAGE_MAP()
};
//{{AFX_INSERT_LOCATION}}
// Microsoft Visual C++ will insert additional declarations immediately before the previous line.
#endif //
!defined(AFX_MYFILEDLG_H__CD5C31AB_828B_48E0_A570_43302E9881BF__INCLUDED_)
```

Resource.h

```
//{{NO_DEPENDENCIES}}
// Microsoft Developer Studio generated include file.
// Used by ComTest.rc
//
#define IDD_ABOUTBOX                    100
```

```
#define IDR_MAINFRAME                128
#define IDR_COMTESTYPE               129
#define IDD_FILENAME                 130
#define IDC_EDIT1                    1000
#define MY_COM_INIT                  32771
#define MY_COM_STOP                  32772
#define MY_COM_BEGIN                 32773
// Next default values for new objects
//
#ifdef APSTUDIO_INVOKED
#ifndef APSTUDIO_READONLY_SYMBOLS
#define _APS_3D_CONTROLS             1
#define _APS_NEXT_RESOURCE_VALUE     131
#define _APS_NEXT_COMMAND_VALUE      32774
#define _APS_NEXT_CONTROL_VALUE      1001
#define _APS_NEXT_SYMED_VALUE        101
#endif
#endif
```

StdAfx.h

```
// stdafx.h : include file for standard system include files,
//  or project specific include files that are used frequently, but
//      are changed infrequently
//
#if !defined(AFX_STDAFX_H__5A9F2227_8435_46CF_ABE2_0C97FCBF0AF0__INCLUDED_)
#define AFX_STDAFX_H__5A9F2227_8435_46CF_ABE2_0C97FCBF0AF0__INCLUDED_
#if _MSC_VER > 1000
#pragma once
#endif // _MSC_VER > 1000
#define VC_EXTRALEAN                 // Exclude rarely-used stuff from Windows headers
#include <afxwin.h>         // MFC core and standard components
#include <afxext.h>         // MFC extensions
#include <afxdisp.h>        // MFC Automation classes
#include <afxdtctl.h>               // MFC support for Internet Explorer 4 Common Controls
#ifndef _AFX_NO_AFXCMN_SUPPORT
#include <afxcmn.h>                 // MFC support for Windows Common Controls
#endif // _AFX_NO_AFXCMN_SUPPORT
//{{AFX_INSERT_LOCATION}}
// Microsoft Visual C++ will insert additional declarations immediately before the previous line.
#endif // !defined(AFX_STDAFX_H__5A9F2227_8435_46CF_ABE2_0C97FCBF0AF0__INCLUDED_)
```

REFERENCES

1. Szeri, A.Z., 1980, *Tribology: Friction, Lubrication and Wear*, Hemisphere Publishing Corporation, New York.

2. Bhushan, B., 2002, *Introduction to Tribology*, John Wiley & Sons, New York.

3. Kragelsky, I.V., Dobychin, M.N., and Kombalov, V.S., 1982, *Friction and Wear*, Pergamon Press, New York.

4. Eyre, T.S., 1976, "Wear Characteristics of Metals," Tribology International, **9**, pp. 203-212.

5. Scott, D., 1979, *Wear Treatise on Materials Science and Technology*, **13**, Academic Press, San Diego.

6. Peterson, M.B., and Winer, W.O., 1980, *Wear Control Handbook*, ASME, New York.

7. Buckley, D.H., 1981, *Surface Effects in Adhesion, Friction, Wear and Lubrication*, Elsevier, Amsterdam.

8. Rigney, D.A., 1981, *Fundamentals of Friction and Wear*, American Society for Metals, Metals Park, Ohio.

9. Bhushan, B., Davis, R.E., and Gordon, M., 1985, "Metallurgical Re-examination of Wear Modes: Erosive, Electrical Arcing and Fretting," Thin Solid Films, **123**, pp. 93-112.

10. Loomis, W.R., 1985, *New Directions in Lubrication, Materials, Wear and Surface Interactions – Tribology in 80's*, Noyes Publications, Park Ridge, New Jersey.

11. Zum Gahr, K.H., 1987, *Microstructure and Wear of Materials*, Elsevier, Amsterdam.

12. Bayer, R.G., 1994, *Mechanical Wear Prediction and Prevention*, Marcel Dekker, New York.

13. Rabinowicz, E., 1995, *Friction and Wear of Materials*, Second edition, John Wiley & Sons, New York.

14. Bhushan, B., 2001, *Fundamentals of Triblogy and Bridging the Gap Between Macro- and Micro/Nanoscales*, Kluwer Academic, Dordrecht, Netherlands.

15. Semenov, A.P., 1958, *Seizure of Metals*, Mashgiz, USSR, in Russian.

16. Kostetsky, B.I., and Edigaryan, F.S., 1964, *Classification of Principal Types of Wear and Elements of Wear Theory in Rolling Friction*, KIGVF, USSR, in Russian.

17. *Friction, Lubrication and Wear Technology*, 1992, ASM Handbook, **18**, Materials Park, Ohio.

18. *Glossary of Terms and Definitions in the Field of Friction, Wear and Lubrication (Tribology)*, 1969, Organization for Economic Cooperation and Development, Paris.

19. Billett, M., 1979, *Industrial Lubrication,* Pergamon Press, New York.

20. Pirlo, D.M., and Wessol, A.A., 2001, *Lubrication Fundamentals*, Second edition, Marcel Dekker, New York.

21. Gruen, D.M., Zuiker, C.D., and Krauss, A.R., 1995, "Diamond Films Grown from Fullerene Precursors," Proceedings of SPIE - Fullerenes and Photonics II, **2530**, pp. 2-13.

22. Ginzburg, B.M., Krasnyi, V.A., Kozyrev, Yu.P., and Bulatov, V.P., 1997, "Decrease of Fretting Wear of Metals in the Presence of Fullerene C_{60}," Trenie i Iznos, **18**, pp. 523-526.

23. Bhushan, B., 1993, "Fullerene Films for Solid Lubrication," S T L E Tribology Transactions, **36**, pp. 573-580.

24. Szucs, A., Tolgyesi, M., Novak, M., Nagy, J.B., and Lamberts, L., 1996, "Photoelectrochemical Behavior of C_{60} Films in Various Oxidation States," Journal of Electroanalytical Chemistry, **419**, pp. 39-46.

25. Murray, R.W. and Iyanar, K., 1997, "Oxidation of Fullerene C_{60} by the Methyltrioxorhenium-hydrogen Peroxide System," Tetrahedron Letters, **38**, pp. 335-338.

26. Ingold, K.U., 1961, "Inhibition of Autoxidation of Organic Substances in Liquid Phase," Chemical Reviews, **61**, pp. 563-589.

27. Johnson, M.D., Korcek, S., and Zinbo, M., 1983, "Inhibition of Oxidation by ZDTP and Ashless Antioxidants in the Presence of Hydroperoxides at 160 ^{o}C," Lubricant and Additive Effects on Engine Wear, **558**, pp. 71-81.

28. Feng, I.M., Perilstein, W.L. and Adams, M.R., 1963, "Solid Film Deposition and Non-sacrificial Boundary Lubrication," ASLE Trans., **6**, pp. 60-63.

29. Jones, R.B., and Coy, R.C., 1981, "The Chemistry of Thermal Degradation of Zinc Dialkyl Dithiophosphate Additives," ASLE Transactions, **24**, pp. 91-97.

30. Brazier, A.D., and Elliot, J.S., 1967, "The Thermal Stability of Zinc Dithiophosphates," J. Inst. Petrol., **53**, pp. 63-67.

31. Curl, R.F., and Smalley, R.E., 1991, "Fullerenes," Scientific American, **265**, pp. 54-63.

32. Huffman, D. R., 1991, "Solid C_{60}," Physics Today, **44**, pp. 22-29.

33. David, W.I.F., Ibberson, R.M., Mattewman, J.C., Prussides, K., Dennis, T.J.S., Hare, J.P., Kroto, H.W., Taylor, R. and Walton, D.R.W., 1991, "Crystal Structure and Bonding of Ordered C_{60}," Nature, **353**, pp. 147 – 149.

34. Dubrovsky, R., 2002, "Development of Cost Effective Ferromagnetic Fullerenes," Report to Picatiny Arsenal, New Jersey.

35. Wilson, R.J., Meijer, G., Bethune, D.S., Johnson, R.D., Chambllis, D.D., deVries, M.S., and Hunziker, H.E., 1990, "Imaging C_{60} Clusters on a Surface Using a Scanning Tunneling Microscope," Nature, **348**, pp. 621-622.

36. Bhushan, B., Ruan, J., and Gupta, B.K., 1993, "A Scanning Tunneling Microscopy Study of Fullerene Films," Journal of Physics D: Applied Physics, **26**, pp. 1319-1322.

37. Duclos, S.J., Brister, K., Haddon, R.C., Kortan, A.R. and Thlel, F.A., 1991, "Effect of Pressure and Stress on C_{60} Fullerite to 20 *GPa*," Nature, **351**, pp. 380-382.

38. Hainey, P.A., Fischer, J.E., Mcghie, A.R., Romanow, W.J, Denestein, A.M., McCauley Jr., J.P., Smith II, A.B. and Cox, D.E., 1991, "Orientational Ordering Transition in Solid C_{60}," Physics Review Letters, **66**, pp. 2911-2914.

39. Frum, C.I., Engelman, R., Hedderich, H.G., Bernath, P.F., Lamb, L.D. and Huffman, D.R., 1991, "The Infrared Emission Spectrum of Gas-phase C_{60} (Buckminsterfullerene)," Chemical Physics Letters, **176**, pp. 504 – 508.

40. Reguiero, M.N., Monceau, P. and Hodeau, J.L., 1992, "Crushing C_{60} to Diamond at Room Temperature," Nature, **355**, pp. 237-239.

41. Ruan, J., and Bhushan, B., 1993, "Nonoindentation Studies of Sublimed Fullerene Films Using Atomic Force Microscopy," Journal of Materials Research, **8**, pp. 3019-3022.

42. Selig, H., Lifshitz, C., Peres, T., Fischer, J.E, McGhie, A. R., Romanow, W.J., McCauley, J.P. and Smith, A.B., 1991, "Fluorinated Fullerenes," Journal of American Chemical Society, **113**, pp. 5475-5476.

43. Howard, J.B., Lafleur, A.L., Makarovsky, Y., Mitra, S., Pope, C.J., and Yadav, T.K., 1992, "Fullerenes Synthesis in Combustion," Carbon, **30**, pp. 1183-1201.

44. Alekseyev, N.I., and Dyuzhev, G.A., 2003, "Fullerene Formation in an Arc Discharge," Carbon, **41**, pp. 1343-1348.

45. Ellacott, M.V., Pang, L.S.K., Prochazka, L., Wilson, M.A., Fitz Gerald, J.D., and Taylor, G.H., 1994, "Composition of Cathode Deposits during Fullerene Production by Carbon Arc Plasma," Carbon, **32**, pp. 542-544.

46. Petcu, S., Cauchetier, M., Armand, X., Voicu, I., and Alexandrescu, R., 2000, "Formation of Fullerenes in the Laser-pyrolysis of Benzene," Combustion and Flame, **122**, pp. 500-507.

47. McBranch, D.W., Smilowitz, L.B., Klimov, V., Koskelo, A., Robinson, J.M., Mattes, B.R., Hummelen, J.C., Wudl, F., Withers, J.C., and Borrelli, N.F., 1995, "Optical Limiting and Excited-state Absorption in Fullerene Solutions and Doped glasses," Proceedings of SPIE - The International Society for Optical Engineering, **25-30**, pp. 196-204.

48. Gudaev, O.A., Malinovskij, V.K., Sanditov, B.D., and Sokolov, A.A., 1996, "Exciton Nature of the Fundamental Absorption Edge in Fullerene Films," Avtometriya, **2**, pp. 94-100, in Russian.

49. Shehter, Yu.N., Shkolnikov, V.M., Bogdanova, T.I., and Milovanov, V., 1979, "Conservative Lubricant Materials," Chemistry, p. 96.

50. Bogdanova, T.I., and Shehter, Yu. N., 1984, "Inhygridation of Oil Compositions for Defense from Corrosion," Chemistry, p. 30.

51. Vidgorovich V.I., Safronova N.V., and Shel N.V., 1996, "Efficiency of Amides of Higher Carbon Acids as Oil Stiffener and Oil-soluble Anticorrosive Additive," Protection of Materials, **32**, pp. 56-60.

52. Vidgorovich V.I., Shel N.V., and Safronova N.V., 1996, "Multifunctional Oil-soluble Anticorrosive Additive Gidrazeks – 89," Protection of Materials, **32**, pp. 319-324.

53. Ginzburg G.N., and Tochilnikov D.G., 2002, "Investigation and Development of New Types of Antifriction and Antiwear Materials on the Base of Fullerenes," Problemy Mashinostraeniya i Nadezhnos'ti Mashin, **2**, pp. 60-68.

54. Pedersen, M.O., Murray, P.W., Legsgaard, E., Stensgaard, I., and Besenbacher, F., 1997, "Carbon-60 Induced Structures on the Clean and Oxygen Covered Cu (110) Surface: Competitive Adsorption," Surface science, **389**, pp. 300-309.

55. Ludema, K.C., 1996, *Friction, Wear and Lubrication*, CRC Press, Boca Raton, Florida.

56. Harnoy, A, 2003, *Bearing Design in Machinery*, Marcel Dekker, New York.

57. Kragelsky, I.V, 1962, *Friction and Wear in Machines*, Mashgiz Press, Moscow, USSR.

58. Bhushan, B., 1999, *Principles and Applications of Tribology*, Wiley-Interscience Publication, New York.

59. Budynas, R.G., 1999, *Advanced Strength and Applied Stress Analysis*, McGraw-Hill, New York.

60. Dubrovsky, R., Kin, Y., and Shih, I.T., 1989, "Development of the Wear Testing Methodology," Proceedings of the First International Applied Mechanical Systems Design Conference, **1**, pp. 571-574.

61. Shih, I.T., 1988, "Seizure and Wear Testing Methodology," M.S. thesis, New Jersey Institute of Technology, Newark, NJ.